Computer Simulation of Gravity-Driven Granular Flow

(Spine Title: Computer Simulation of Gravity-Driven Granular Flow)

(Thesis Format: Integrated Article)

by

John Jan <u>Drozd</u>

Graduate Program in Applied Mathematics

A thesis submitted in partial fulfillment
of the requirements for the degree of
Doctor of Philosophy

The School of Graduate and Postdoctoral Studies
The University of Western Ontario
London, Ontario, Canada

THE UNIVERSITY OF WESTERN ONTARIO
SCHOOL OF GRADUATE AND POSTDOCTORAL STUDIES

CERTIFICATE OF EXAMINATION

Supervisor

_____
Dr. Colin Denniston

Examiners

_____
Dr. David Jeffrey

_____
Dr. Adam Metzler

_____
Dr. John R. de Bruyn

_____
Dr. Narayanan Menon

The thesis by

John Jan Drozd

entitled:

COMPUTER SIMULATION OF GRAVITY-DRIVEN GRANULAR
FLOW

is accepted in partial fulfillment of the
requirements for the degree of
Doctor of Philosophy

_____
Date

_____
Chair of the Thesis Examination Board

ii

Abstract

We develop and use three-dimensional event-driven molecular dynamics simulations of dry gravity-driven granular flow. Our system is comprised of mono- and poly-disperse sets of spherical grains falling down a vertical chute under the influence of gravity. We observe three phases or states of granular matter: a free-fall dilute granular gas region at the top of the chute, a granular fluid in the middle and then a glassy region at the bottom.

We investigate collision time distributions as one approaches the static limit of steady-state flow of dry granular matter. The collision times fall in a power-law distribution with an exponent dictated by whether the grains are ordered or disordered. Remarkably, the exponents have almost no dependence on dimension. We are also able to resolve a disagreement between simulation and experiments on the exponent of the collision time power-law distribution. We also investigate velocity fluctuations in dry granular flow. We find three different classes of velocity distributions depending on factors such as the local density. The class of the velocity distribution depends on whether the grains are in a free-fall, fluid or glassy state. The analytic form of the distributions match those that have been found by other authors in fairly diverse systems. Here, we have all three present in a single system in steady-state. Power-law tails that match recent experiments are also found but in a transition area suggesting they may be an artifact of crossover from one class of velocity distribution to another. We find evidence that the transition from one class to another may correspond to a second order dynamical phase transition in the limit that the vertical flow speed goes to zero.

Finally, we investigate constitutive relations in dry granular flow. We examine local stresses, heat flow, and dissipation in all three phases of our system. We find

a complete closed set of constitutive relations capable of describing the system in the different regions and test several proposed constitutive relations in the fluid and glassy regions. Similar to static sand piles, we find that stresses in the glassy region are almost entirely determined by directions along which collisions occur. We show that the static sand pile is the static limit of our glassy state. We also examine the strain rate and viscosity dependence on the granular temperature. While finding regimes consistent with experiments, we find that these quantities do not exhibit a universal power-law relationship. However we do find a universal power-law relationship between the shear stress and the shear rate in the glassy region, and likewise between viscosity and shear rate in the glassy region. We show that there is a yield stress associated with our glassy system and we demonstrate the stress and energy balance in the different regions of our system. We show that Fourier's law for heat flow is obeyed in the glassy region, however care must be taken in separating energy and heat flow. In the glassy region the conductivity is equal to the volume fraction times the mean collision frequency. In the fluid region the thermal conductivity has an exponential dependence on the granular temperature. We finally close our relations by deriving an expression for the mean collision frequency in terms of the pressure and granular temperature.

Statement of Co-Authorship

Chapters 2 - 4 of this thesis consist of the following papers:

Chapter 2: J.J. Drozd and C. Denniston, Simulations of collision times in gravity-driven flow, Europhys. Lett. **76**, 360 (2006).

Chapter 3: J.J. Drozd and C. Denniston, Velocity fluctuations in dense granular flows, Phys. Rev. E **78**, 041304 (2008).

Chapter 4: J.J. Drozd and C. Denniston, Constitutive relations in dense granular flows, *submitted*.

Chapter 2 is a publication in an Institute of Physics (IOP) Journal and Chapter 3 is a publication in an American Physical Society (APS) journal. Both journals allow including this published material in this thesis, without requesting permission from the publisher. These copyright policies are outlined on the IOP and APS web sites.

The original draft for each of the above articles was prepared by the author. Subsequent revisions were performed by the author and Dr. Colin Denniston. The software development in transforming Dr. Colin Denniston's two-dimensional code to three dimensional code and adding further functionality to the C code and developing Povray visualizations, as well as performing analytical and numerical work using Mathematica software was performed by the author under the supervision of Dr. Colin Denniston.

An Epigraph Poem For My Beloved Mother
On Tequila Bay

On Tequila Bay

I sail and sing all day

I think about the birds

Wings flying above

And the tree leaves

With a moistened glow

Dripping water from

The sky's rain

It's a music of life

Of high notes and low

To struggle, strain and learn

An inner yearn

To always glimmer hope

And valiantly cope

To live another day

On Tequila Bay

John Jan Drozd

I wrote this poem to remind myself to live life to the fullest and to never give up a life because you don't know when your time comes up, as taught by Ecclesiastes in the Old Testament.

A Dedication To My Beloved Mother

To my mother Frantiska (Frances) Drozd (May 24, 1931 - March 29, 2008).
I pray that my mother rests in peace in heaven with her favourite red carnations,
and is enjoying her time being reunited with her parents in heaven.

My mom passed away on March 29, 2008.
I love and miss my mom very much, especially Mom's happy smile.

Acknowledgements

I welcome this opportunity to thank all those people who helped me in pursuing my thesis project with their valuable comments and ideas. First and foremost, I would like to thank my supervisor Dr. Colin Denniston for his patience, helpful guidance and careful, critical proofreading of my papers and thesis. I would like to thank Dr. Colin Denniston for allowing me to work in this fascinating and active field of research and for introducing me to the capabilities of Mathematica software to statistically analyze and plot my C program generated data. Also, I would like to thank Dr. Colin Denniston for his most valuable and critical comments during our long discussions that we had in producing our papers. Dr. Colin Denniston always provided me consistent direction and unique insight into my research. As well, I must thank Dr. Colin Denniston and my committee advisors, Dr. Martin Müser and Dr. Lindi Wahl who always gave me positive support, giving me a full month time off during my difficult time when I had to cope with my mother's passing away during my graduate studies. Most importantly, I would like to thank my late Mom, Dad and sisters for the patience, understanding and support they gave me throughout my entire life and for their continuing belief in me. Finally, I would like to acknowledge my Ontario Government for their award of a Postgraduate Ontario Graduate Scholarship that has supported this study.

Table of Contents

List of Figures

xiii

CHAPTER 1

Introduction

1.1 Background Literature Review

The physics of granular materials or granular matter comes from a longstanding history. Eminent scientists such as Coulomb during the reign of Louis XVI, Faraday, Reynolds, Hagen, Huygens, Rayleigh, and Bagnold in the twentieth century contributed significantly to the early study of granular materials [1, 2, 3, 4, 5, 6, 7]. Following these early days, the physical approach led to engineering fields studying granular flows, pattern formation and packing. However, in spite of these valiant efforts, granular materials to this day are not fully understood.

The reason for encountering such mystery when one attempts to understand granular matter is that it is a unique, complex material. It is neither a solid nor a liquid and falls into a realm with material properties of its own. Granular matter has been coined as a general term to describe a material that is made up of particles that are at least visible to the naked eye. Granular matter ranges from grains of a few hundred microns each, to ice floes drifting across the polar seas, to everyday rocks, sands, seeds, beads, pharmaceutical pills, sugars, to Saturn's rings (made of icy particles about 1 cm wide distributed in a band roughly 1 km thick). The science of granular matter covers several orders of magnitude. Consequently,

granular matter is a system of interest to people working in many fields including biologists, physicists, astronomers, engineers, geologists, and material scientists. It has been proposed that *"[t]he fact that aggregates seem to obey 'universal laws' applicable over such a wide range of dimensions and characteristics is a strong incentive to pursue fundamental studies in that area."* [8].

It is important to understand the nature of granular materials not only from a scientific standpoint. There are many important practical applications for studying granular materials. Statistics indicate that *"[t]he processing of granular media and aggregates consumes roughly 10% of all energy produced on this planet. As it turns out, this class of materials ranks second, immediately behind water, on the scale of priorities of human activity. As such, any advance in understanding the physics of granulars is bound to have a major economic impact."* [8, 9]. Jacques Duran, in his book entitled *Sands, Powders and Grains* describes the industrial processes involved with granular materials: *"The industrial technology used in the treatment of granular materials involves a number of processes. First comes the extraction of ores, sands, and gravel, which often relies on dredging. Next comes crushing and grinding, followed by separation, all of which are commonly used with low-value-added materials. ... [M]ethods of transport (fluidized beds, conveyor belts), storage (silos), and mixing (e.g. cement trucks) figure in all stages of the industrial processing. For instance, the phenomena of segregation and intermittent blockages are pervasive in numerous industrial processes involving granular materials."* [8] The development of these technologies date back to the nineteenth century. Recent advances, however, have addressed some of the problems associated with industrial processes. For instance, scientists have studied force chains in granular materials extensively to address these problems [10, 11]. Many silo failures are due to large stress fluctuations resulting from blockages by arching caused by the discharge process of granular materials. Scientists have also modeled avalanches and giant stress fluctuations in silos and

compared theoretical stress models to experiments [12, 13]. An interesting silo design, developed by the National University of Mexico, used a hexagonal geometry to relieve the lateral wall stresses. This design was based on the angle of repose of the granular material [14].

My M.Sc. research at the Applied Mathematics Department at The University of Western Ontario investigated a food processing application. This involved studying flow patterns and stresses in the manufacturing of candies [15, 16] and grinding of bulk chocolate [17] using computer simulations. These simulations were coupled with physical experiments that were designed and carried out at the Department of Mechanical and Materials Engineering. Examples of such collaboration show that with the advent of high performance computers, with its enormous advances in computing power, the science of granular materials can be studied in greater depth [18].

Savage and Jeffrey [20] used the concept of the coefficient of restitution to theoretically describe the momentum transport of inelastically colliding granular particles. This allowed physicists to model real-world inelastic granular systems. Today, scientists and engineers are working hard to obtain a complete description of granular phenomena but there are still serious obstacles that they face. Theorists who often use Boltzmann equilibrium statistical mechanics to connect the microscopic level to the macroscopic description of granular materials, use a Boltzmann scaled temperature $k_B T$ which is small compared to the macroscopic scales of granular matter. Due to the highly dissipative nature of granular collisions, without a constant energy input to maintain a steady state balance with energy dissipation, one can envision that the particles would inelastically collapse and the system would halt to an ambient temperature. One can perform a simple calculation using $E = k_B T = \frac{1}{2} m v^2$ (using a particle mass of say 1 gram and a room temperature of 300 Kelvin) and show that the velocity of the particles in such a situation would be on the order of tens of nanometers per second.

Typically in steady-state, a particle takes approximately 200 seconds to move a particle diameter in a jammed region. A nanoscale speed is far too low to bring a configuration of a large number of macroscopic grains into equilibrium. For comparison, here $k_B T \ll \rho g a$, where ρ is the density, g is the acceleration due to gravity and a is the particle radius.

A related complication with applying the Boltzmann distribution of a deterministic mechanics to granular matter in which granular collisions are inelastic and thus involve a dissipation of energy, is that this dissipation gives rise to instabilities and dense clustering. Steady state systems of heated granular gases consisting of inelastic particles are statistically different from an equilibrium state [21]. Unlike the Boltzmann distribution, the energy distribution for gases consisting of inelastic particles exhibits overpopulated high energy tails. These tails are also evident in velocity distributions obtained by experiments [22, 23, 24, 25] and our computer simulations [26]. Thus, the Boltzmann distribution and the Boltzmann equation can only be approximately used to theoretically describe granular gases for low density systems that have small inelasticity [27].

Esipov and Poschel [28] used a kinetic energy distribution function satisfying the Boltzmann equation to study a system of inelastic hard spheres. They studied the kinetic energy distribution function to present the limits of validity of a hydrodynamic description of granular matter. They reduced the Boltzmann equation to hydrodynamics without having to consider divergence of transport coefficients. They assumed their particles behaved isotropically and were in a homogeneous state, and that the distribution function only depended on the kinetic energy. They also used a two-dimensional molecular dynamics simulation of 5000 particles enclosed by a circular wall that was maintained at a constant temperature. This simulation was used to support their analytical formulations. Their results suggested that these inelastic systems can be subdivided into phases. They suggested the existence of a dilute granular gas-like phase near the wall, a condensed

phase of closely packed particles between the bulk center and the wall, and a collapsing condensed phase close to the center of the container. It is a common but mistaken belief that there is only a jamming transition in granular materials, when in fact there are transitions between three regions. There are transitions between a granular gas and a condensed phase and as well between a condensed phase and a collapsing condensed phase. We similarly are able to produce three distinct phases of granular matter in our simulation: a dilute free-falling granular gas, a granular fluid and a jammed glass, and even a partially crystallized state when we used identically-sized particles. We find that the transitions between these three phases have distinct physical properties and we will describe these throughout the thesis.

Esipov and Poschel's [28] results were built upon by Noije and Ernst [29] who solved the nonlinear Enskog-Boltzmann equation for a system of heated inelastic spheres. They described a buildup of spatial velocity correlations, and found that their incompressibility assumption was no longer valid beyond a distance that diverged in the elastic limit. Further work on the nonlinear Boltzmann equation was conducted by Ernst and Brito [30] who added stochastic noise to the microscopic equations of motion to study velocity distributions in the different phases of granular matter. It is clear that more work needs to be done in extending hydrodynamic descriptions of granular materials into the inelastic, denser regimes. It will be demonstrated throughout this thesis that granular matter behaves significantly differently in different regions or phases. This is a major contribution to paving the way to establishing an understanding of how microscopic laws of motion can combine together to form the macroscopic phenomena of granular matter.

1.2 Outline

With this approach in mind, for the purposes of this thesis, a three-dimensional computer simulation of gravity-driven dry granular flow comprising of approximately $40,000$ discrete hard spheres, was developed to produce various states or phases of granular matter. The matter was considered as discrete classical particles in which contact forces and dissipation were key ingredients. Continuous energy input was needed in order to mobilize and maintain the particles in motion, due to the highly dissipative nature of particle collisions. Gravity was an essential component to provide constant energy input into the system.

An efficient event-driven molecular dynamics simulation in which the particles were advanced sequentially by the next shortest collision time was used. Each collision altered the velocities of the involved particles according to a collision law which was characterized by coefficients of restitution. During the time intervals between collisions, the particles would move along known ballistic trajectories. Thus, the positions of the particles at the time of the next collision could be computed in one step. This algorithm is outlined in [17, 18, 19].

The states of granular matter that were produced by the simulation include a range from a dilute freely falling granular gas, to a granular fluidized state, and finally, a jammed glassy state using poly-disperse (various-sized) particles and even a crystallized state using mono-disperse (same-sized) particles. Measurements from this simulation allowed us to examine properties of granular matter in a wide range of different states.

Following is a brief description of the next three chapters that comprise the body of this thesis. All three chapters are based on results obtained from an event-driven molecular dynamics computer simulation of gravity-driven dry granular matter flow. Figure 1.1 shows a visualization of the simulation that was used to

generate the measurements for the thesis. The simulation is described in detail within the chapters. Relevant literature reviews are also provided within these chapters. Briefly, Chapter 2 studies the distributions of collision times in gravity-driven granular flow in two and three dimensions. Comparisons are made with an experiment and by relating impulses to collision times, a definitive universal collision time distribution is established in a granular glassy state. Collision time distributions are also studied in the fluid state of our simulation. Chapter 3 studies velocity distributions in the free-fall gas, fluid, and jammed glassy state. It is clearly shown that the particular form of the velocity distribution depends on which granular state the measurements are made in. Finally, in Chapter 4, with the aim of better understanding the equations of mass, momentum and energy conservation, constitutive relations in dense granular flow are studied and comparisons are made to experiment and theory. Our results establish that collision times, velocity distributions and constitutive relations all behave differently in the different granular states or phases. Following is some background information for each of these chapters.

1.3   Relaxation times

Problems in granular materials deal with nonequilibrium situations which require a detailed understanding of the nonequilibrium processes whereby energy is transported from one granular particle to another. In granular matter, this energy transfer process involves particles interacting with each other via collisions.

If we consider a box container filled with hard elastic particles, a reasonable assumption would be that the collisions in particle trajectories would be independent, that is a collision for a particle would not depend on its history of previous collisions. Here we define a collision time as the time between successive collisions
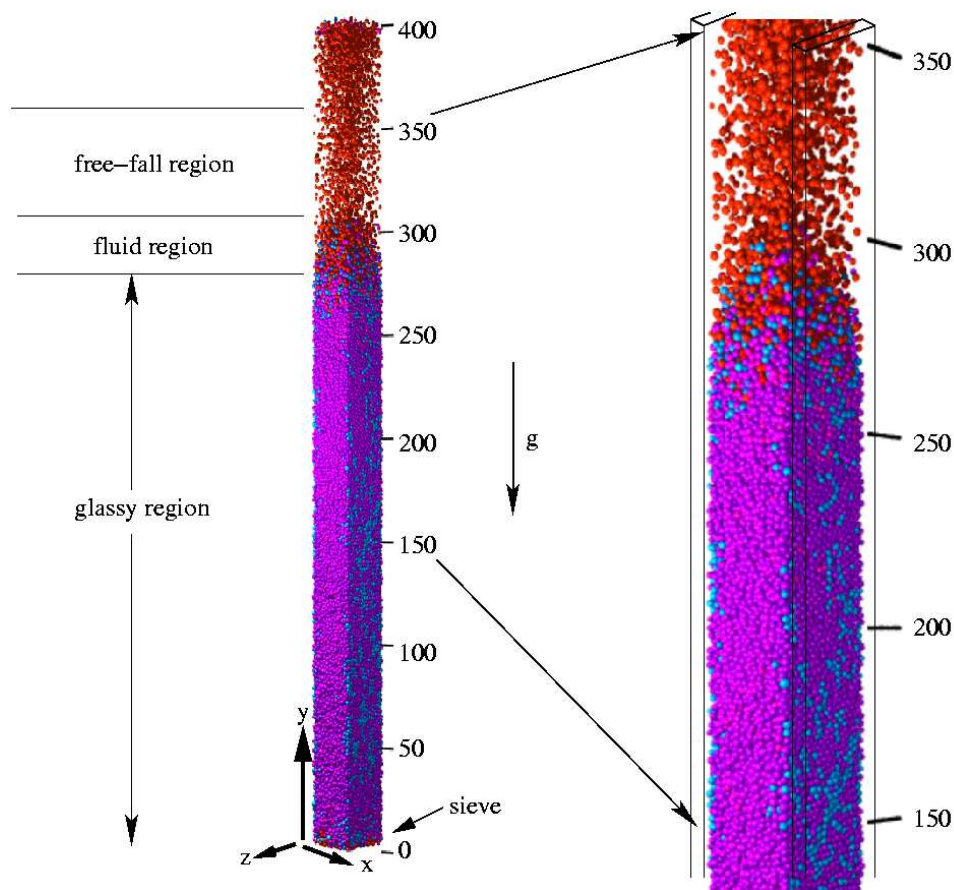
Figure 1.1: Section of a simulation involving 43 200 grains with 15 % polydispersity. The system size is $32a \times 32a \times 400a$. There are reflective walls at $x = 0$ and $x = L_x$, periodic boundary conditions in the z-direction, and a finite probability of reflection at the bottom of the chute (at $y = 0$). The particles are coloured according to the magnitude of their y-velocity with red balls traveling the fastest and blue balls slowest.

for a particle. We will show mathematically below that such an independence of collisions leads to an exponential distribution of collision times. On the other hand, if we do not observe an exponential collision time distribution, then the collisions must be history-dependent.

We now derive the exponential collision time distribution for a particle with independent collision events. We will follow the derivation given in [31]. Consider a particle with velocity v. Let $P(t)$ represent the probability that a molecule survives a time t without collision. $P(t = 0) = 1$ since a particle has no chance of suffering a collision at $t = 0$. As time progresses, the particle is exposed to the chance of suffering a collision. Let w be the probability per unit time that a particle will collide, called the collision rate. We will assume that w is independent of the particle's past history, that is, it is irrelevant when the particle last collided. Then $w\, dt$ is the probability that a particle suffers a collision between time t and $t + dt$.

We note that $P(t + dt)$, the probability that a particle does not collide within a time $t + dt$, must equal the probability $[P(t)]$ that a particle does not collide within a time t multiplied by the probability $[(1 - w\, dt)]$ that the particle does not collide in the later time interval between t and $t + dt$.

Hence,

$$P(t + dt) = P(t)(1 - w\, dt). \tag{1.1}$$

Thus,

$$P(t) + \frac{dP}{dt}dt = P(t) - P(t)wdt, \tag{1.2}$$

or

$$\frac{1}{P}\frac{dP}{dt} = -w. \tag{1.3}$$

Upon integrating equation (1.3), we get

$$
\begin{aligned}
\ln P &= -wt + \mathbf{constant} \\
P &= Ce^{-wt}
\end{aligned}
\tag{1.4}
$$

Since a particle has no chance of suffering a collision at $t = 0$, we have $P(0) = 1$, so the constant of integration $C = 1$. Thus, equation (1.4) becomes

$$
P = e^{-wt}.
\tag{1.5}
$$

Finally, putting this all together, we have the probability that a particle, after surviving without collisions for a time t, collides in the time interval between t and $t + dt$ is

$$
P_{\mathbf{collision}} \; dt = e^{-wt} w \; dt.
\tag{1.6}
$$

We let τ be the "collision time" or mean time between collisions, being

$$
\begin{aligned}
\tau &= \int_0^\infty t \, P_{\mathbf{collision}} \; dt \\
&= \int_0^\infty t \, e^{-wt} w \; dt \\
&= \frac{1}{w} \int_0^\infty e^{-y} y \; dy \\
&= \frac{1}{w}.
\end{aligned}
\tag{1.7}
$$

Equation (1.5) is depicted graphically in Figure 1.2(a). In the glassy region of our granular system, an exponential collision time distribution was not observed, leading us to conclude that collisions are history-dependent in a granular glass.
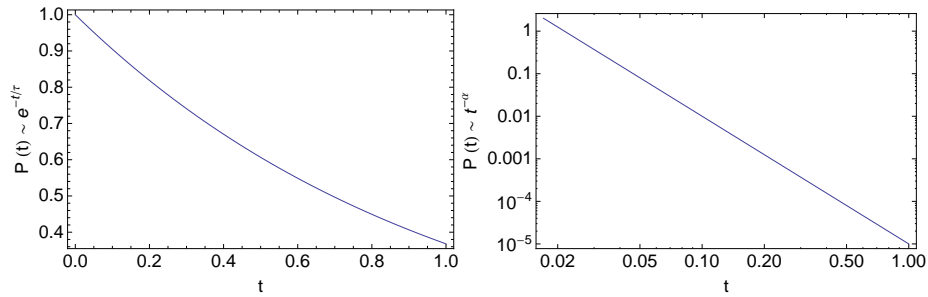
Figure 1.2: (a) Exponential collision time distribution as found in a granular fluid and (b) Power-Law collision time distribution as found in a granular glass.

In particular, we observed power-law behaviour in the glassy region:

$$P(t) \sim t^{-\alpha}, \tag{1.8}$$

where t is the collision time. Equation (1.8) is depicted graphically in Figure 1.2(b) on a log-log scale. In the fluid region, the collision times were distributed exponentially at the tails, but were power-law at short times. In Chapter 2, we use our simulation to investigate collision time distributions during steady-state, in a granular glass and in a fluidized state. Poly-disperse simulations (with different-sized particles) and mono-disperse simulations (with same-sized particles) are compared. The collision time distributions observed from our simulation differ from a collision time distribution that was obtained by a granular experiment and we resolve this discrepancy in our paper to arrive at the definitive collision time distribution.

1.4 Velocity Distributions

The Maxwell-Boltzmann distribution is the most likely velocity distribution for systems in equilibrium. The Maxwell-Boltzmann distribution, for example, pro-

vides a good approximation in a gas, and in a fluid region which is in equilibrium.

When Boltzmann derived the Maxwell-Boltzmann distribution he focused on a general Hamiltonian system, that is, a system of N point particles with an arbitrary interaction potential. The state of this system can be described as a phase point $x = (\vec{p_1}, ..., \vec{p_N}, \vec{q_1}, ..., \vec{q_N})$ in a phase space of momenta $\vec{p_i}$ and positions $\vec{q_i}$. By the Hamiltonian equations of motion, this phase point x evolves over time, and thus describes a trajectory x_t. This trajectory lies on a given energy hypersurface $H(x) = E$, where $H(x)$ is the Hamiltonian function.

The Maxwell-Boltzmann distribution characterizes the state of a gas of elastic hard spheres by means of a probability distribution f over the various values of the particle velocities. It can be expressed as [32]

$$f(\mathbf{p}) = Ce^{-\beta E_i}, \tag{1.9}$$

where $\beta = 1/k_B T$ with k_B being Boltzmann's constant, $\mathbf{p}$ is the momentum, T the absolute temperature and E_i an eigenvalue energy state of the Hamiltonian H.

The parameters C and β are determined by evaluating the integrals (using Gaussian integrals and their derivatives):

$$\begin{aligned} \int d^3 p f(\mathbf{p}) &= n, \\ \frac{1}{n} \int d^3 p \frac{\mathbf{p}^2}{2m} f(\mathbf{p}) &= \frac{E}{N}, \end{aligned} \tag{1.10}$$

where n is the density of the gas, and E/N is the energy per particle.

For our system of granular particles, our Hamiltonian is

$$H = \sum_i \frac{p_i^2}{2m} + \sum_{i \neq j} V(\mathbf{r_i}, \mathbf{r_j}), \tag{1.11}$$

where $\mathbf{p}$ is the momentum of a particle, m its mass, and V the hard sphere potential

$$V(\mathbf{r_1}, \mathbf{r_2}) = \begin{cases} 0, & |\mathbf{r_1} - \mathbf{r_2}| \geq 2a \\ \infty, & |\mathbf{r_1} - \mathbf{r_2}| < 2a \end{cases} \tag{1.12}$$

where a is the particle radius.

By inserting equation (1.11) into equation (1.9), we finally arrive at the Maxwell-Boltzmann distribution that characterizes our gas of hard spheres

$$f(\mathbf{p}) = C e^{-\beta \left(\sum_i \mathbf{p}_i^{\,2}/2m + \sum_{i \neq j} V \right)}, \tag{1.13}$$

where $\beta = 1/k_B T$ with k_B being Boltzmann's constant, T the absolute temperature, V the hard sphere potential, and C the normalization constant

$$C = \prod_i \int_{p_{\mathbf{min}}}^{p_{\mathbf{max}}} dp_i \; e^{-\beta \left(\sum_i \mathbf{p}_i^{\,2}/2m + \sum_{i \neq j} V \right)}. \tag{1.14}$$

One would expect that collisions would bring granular particles from a nonequilibrium situation to an equilibrium situation that satisfies a Maxwell-Boltzmann velocity distribution. If the potential V is independent of momenta, the velocity distribution should factorize giving

$$P(v_x, \; v_y, \; v_z) \sim e^{-\frac{m\left(v_x^2 + v_y^2 + v_z^2 \right)}{2k_B T}} \tag{1.15}$$

for any given grain.

Thus we expect a Gaussian distribution of velocities. This is not observed in our simulations. The reason for this failure can be found by examining equation (1.10). For an inelastic system, equation (1.10) integrates over a momentum distribution, but here we have a system where energy is not conserved so this normalization condition is not well-defined. Systems of inelastic granular particles are statistically different from an equilibrated Gaussian state. The velocity distribution for gases consisting of inelastic particles has overpopulated tails. This is observed in experiments [22, 23, 24, 25] and our computer simulations [26].

After investigating the collision time distributions, we used our event-driven simulation to find appropriate relations for the velocity distributions or fluctuations in the granular gas, fluid and glass states of our system. Basing our analysis on the statistical mechanics for our system in steady-state, in chapter 3, we measure the velocity distribution and compare to theoretical and experimental results.

Several experimental papers [22, 23, 24, 25, 33, 34, 35], as well as theoretical [28, 29, 30, 36] and simulation results [36], have reported different non-Maxwell Boltzmann velocity distributions in the fluid and glass states of granular matter. Using our simulation, we reconcile the different velocity distributions that were measured by associating them with various phases of granular matter. We relate and compare the observed velocity distributions in the free-fall gas, granular fluid and glassy regions with the relevant theory and reconcile conflicting results from experiments.

1.5 Constitutive Relations

In chapters 2 and 3, we will show that the derived history-independent exponential collision time distribution given by Equation (1.5), and the Maxwell-Boltzmann Gaussian velocity distribution given by Equation (1.15), cannot be universally

applied to all the states of granular matter. This leads us to chapter 4, where we concentrate on the basic continuum physics equations of momentum conservation, mass conservation and energy conservation. The continuum equations that we map our simulation results onto are

$$
\begin{aligned}
\frac{\partial \rho}{\partial t} + \nabla \cdot (\rho \mathbf{v}) &= 0, \\
\partial_t(\rho v_\alpha) + \partial_\beta(\rho v_\alpha v_\beta) &= \partial_\beta \sigma_{\alpha\beta} + \rho g_\alpha, \\
\partial_t (E) + \partial_\alpha (F_\alpha) &= I + \rho g \cdot \mathbf{v},
\end{aligned}
\tag{1.16}
$$

where ρ is the density, v the velocity, σ is the stress tensor, E is the kinetic energy, $\mathbf{F}$ is the energy flux, I is the dissipation and α and β refer to the x or y or z components. The Einstein summation convention is used for repeated indices α and β.

In order to solve these continuum relations we need constitutive relations. These constitutive relations allow the continuum equations to be solved by relating the stress σ, dissipation I and energy flux $\mathbf{F}$ to the physical variables of density ρ, velocity v and energy E. We also examine transport coefficients of viscosity and thermal conductivity which are parameters in the constitutive relations. We study these constitutive relations in the free-fall gas, fluid and glassy phases of granular matter because we find that the constitutive relations behave differently in these different regions. We compare our simulation results to experiments [22, 23] and theory [37, 38, 39, 40].

For a system of elastic hard spheres, that has a Maxwell-Boltzmann distribution of velocities and has independent collisions, that is, for "a hard sphere gas", one can show that appropriate constitutive relations for pressure can be obtained from a virial expansion at low densities, and a free-volume theory expression at

higher densities [37, 38]. Other relations relate shear stress to viscosity

$$\sigma_{\alpha\beta} = \eta \partial_\alpha v_\beta \quad \text{for } \alpha \neq \beta, \tag{1.17}$$

with the viscosity for a hard sphere gas being [41]

$$\eta = \frac{5}{64} \frac{1}{a^2} \sqrt{\frac{m k_B T}{\pi}}, \tag{1.18}$$

where a is the particle radius. Others relate the energy flux $\mathbf{F}$ to the heat flux $\mathbf{Q}$

$$F_\alpha = (Q_\alpha - \sigma_{\alpha\beta} v_\beta) + v_\alpha E, \tag{1.19}$$

with $\mathbf{Q}$ given by Fourier's Law

$$\mathbf{Q} = \kappa \nabla T. \tag{1.20}$$

Here, the thermal conductivity for a hard sphere gas is [41]

$$\kappa = \frac{25}{128} \frac{c_V}{a^2} \sqrt{\frac{k_B T}{\pi m}}. \tag{1.21}$$

One might expect that our fluid region acts as a hard sphere gas. Upon observing equations (1.18) and (1.21), one would expect that the viscosity and conductivity should increase with temperature. We will find that for the fluid region in our simulation, that the viscosity and heat conductivity are not proportional to $T^{1/2}$, and in fact are decreasing functions with temperature. This behaviour is often associated with a liquid whose viscosity and thermal conductivity increase as the liquid approaches the solid state.

Finally we look at the glassy state and analyze it using the fixed principal axes (FPA) model [42, 43] that is used for static sand piles. By comparing the eigen-

values of the stress tensor in the glassy region, we show agreement between the FPA model and our simulation data. Thus we effectively show that the static sand pile is the static limit of our glassy state.

The final chapter concludes by combining the results and provides recommendations for future work.

REFERENCES

[1] C. A. Coulomb, Acad. Roy. Sci. Mem. Phys. Divers Savant **7**, 343 (1773).

[2] M. Faraday, Philos. Trans. Roy. Soc. London **147**, 9 (1857).

[3] O. Reynolds, Phil. Mag. Ser. 5 **50**, 469 (1885).

[4] Lord Rayleigh, Phil. Mag. Ser. 6 **11**, 129 (1906).

[5] R. A. Bagnold, *The Physics of Blown Sand and Desert Dunes*, (Methuen, London, 1941).

[6] R. A. Bagnold, Proc. Roy. Soc. London Ser. A **225**, 49 (1954).

[7] R. A. Bagnold, Proc. Roy. Soc. London Ser. A **295**, 219 (1966).

[8] J. Duran, *Sands, Powders and Grains: An Introduction to the Physics of Granular Materials*, (Springer, New York, 1999).

[9] The statistic quoted here is from data published by Lafarge-Coppée, a worldwide leader in the manufacture of all types of construction materials. (no specific report title or number was mentioned)

[10] C.-h. Liu, S. R. Nagel, D. Shecter, and S. Coppersmith, Science, **269**, 513 (1995).

[11] D. M. Mueth, H. M. Jaeger, and S. R. Nagel, Phys. Rev. E **57**, 3164 (1998).

[12] P. Claudin and J.-P. Bouchaud, Phys. Rev. Lett. **78**, 231 (1997).

[13] L. Vanel, P. Claudin, J.-P. Bouchaud, M. E. Cates, E. Clément and J. P. Wittmer, Phys. Rev. Lett. **84**, 1439 (2000).

[14] G. H. Ristow, *Pattern Formation in Granular Materials, Springer Tracts in Modern Physics* pp. 79-80 (Springer, New York, 2000).

[15] P. Sistla, O. Baran, Q. Chen, S. Fohhano, P.H. Poole and R.J. Martinuzzi, Phys. Rev. E **71**, 011303 (2005).

[16] O. Baran, J.J. Drozd, R.J. Martinuzzi and P.H. Poole, Phys. Rev. E **76**, 021305 (2007).

[17] J.J. Drozd, *Computer Simulation of Granular Matter: A Study of An Industrial Grinding Mill*, M.Sc. Thesis, Graduate Program in Applied Mathematics, The University of Western Ontario, 2004.

[18] T. Pöschel and T. Schwager, *Computational Granular Dynamics: Models and Algorithms*, (Springer, New York, 2005).

[19] M. P. Allen and D. J. Tildesley, *Computer Simulation of Liquids*, (Oxford University Press, New York, 1999).

[20] S. B. Savage and D. J. Jeffrey, J. Fluid Mech. **110**, 255 (1981).

[21] Y. Srebro and D. Levine, Phys. Rev. Lett. **93**, 240601 (2004).

[22] W. Losert, D. G. W. Cooper, J. Delour, A. Kudrolli and J. P. Gollub, Chaos **9**, 682 (1999).

[23] W. Losert, L. Bocquet, T. C. Lubensky and J. P. Gollub, Phys. Rev. Lett. **85**, 1428 (2000).

[24] F. Rouyer and N. Menon, Phys. Rev. Lett. **85**, 3676 (2000).

[25] S. Moka and P. R. Nott, Phys. Rev. Lett. **95**, 068003 (2005).

[26] J.J. Drozd and C. Denniston, Phys. Rev. E **78**, 041304 (2008).

[27] *Granular Gases*, edited by T. Pöschel and S. Luding (Springer, Berlin, 2001); *Granular Gas Dynamics*, edited by T. Pöschel and N. Brilliantov (Springer, Berlin, 2003).

[28] S. Esipov and T. Poschel, J. Stat. Phys. **86**, 1385 (1997).

[29] T. P. C. van Noije, M. H. Ernst, R. Brito and J. A. G. Orza, Phys. Rev. Lett. **79**, 411 (1997).

[30] M. H. Ernst and R. Brito, Phys. Rev. E **65**, 040301 (2002).

[31] F. Reif, *Fundamentals of statistical and thermal physics*, (McGraw-Hill, Toronto, 1965), pp. 463-465.

[32] K. Huang, *Introduction to Statistical Mechanics*, (Taylor & Francis, New York, 2001), p. 74.

[33] V. V. R. Natarajan, M. L. Hunt and E. D. Taylor, J. Fluid Mech. **304**, 1 (1995).

[34] H. Takahashi and H. Yanai, Powder Technol. **7**, 205 (1973).

[35] S. B. Savage, J. Fluid Mech. **92**, 53 (1979).

[36] E. Ben-Naim and J. Machta, Phys. Rev. Lett. **94**, 138001 (2005).

[37] Z. W. Salsburg and W. W. Wood, J. Chem. Phys. **37**, 798 (1962).

[38] N. F. Carnahan and K. E. Starling, J. Chem. Phys. **51**, 635 (1969).

[39] J. Kolafa, unpublished results cited in T. Boublik and I. Nezbeda, Coll. Czech. Chem. Commun. **51**, 2301 (1986).

[40] A. Malijevsky and J. Veverka, Phys. Chem. Chem. Phys. **1**, 4267 (1999).

[41] R. G. Mortimer, *Physical Chemistry, Third Edition* (Elsevier, London, 2008), p. 464, 465, 470.

[42] M.E. Cates, J.P. Wittmer, J.-P. Bouchaud and P. Claudin, Chaos **9**, 511 (1999).

[43] M.E. Cates, J.P. Wittmer, J.-P. Bouchaud and P. Claudin, Physica A **263**, 354 (1999).

Chapter 2

Simulations of collision times in gravity driven granular flow

Dense granular matter does not easily fit into our standard classification of matter. Interest in the physics community was stimulated by the observation that forces between particles in the system are exponentially distributed suggesting that any load on the system is carried by a small number of force chains [1, 2]. More recent studies have suggested that spatial ordering is a key factor in the force response [3, 4], something that may not be clearly distinguishable from the exponential tail of the force distribution. Further work, both experimental and theoretical, has suggested that perhaps it is actually the low end of the force distribution that should be examined when deciding whether a system is jammed [5, 6, 7].

As the distribution of forces in a static granular system is history dependent [8], it makes sense to explore the static limit of dynamic models in order to shed light on the origin of jamming. In this letter, we perform simulations of gravity driven dense granular flow in two and three dimensions using an event-driven model involving only binary collisions. We reproduce the known power law relationship between the mean flow velocity and velocity fluctuations [9] and explain the discrepancy between the experimentally observed power law for the distribution of collision times [10] and that found in previous simulations [11]. Further, we

find that the distribution of collision times is capable of differentiating between ordered and disordered glassy systems. Moreover, the exponents appear to be superuniversal in the sense that they are independent of dimension. In addition, we find that the force distribution turns *up* at low impulses in the jammed state.

We simulate hard spheres as they fall down a rectangular chute under the influence of gravity, as shown in Fig. 2.1(a). At the bottom of the chute a sieve is modeled by having the particles reflecting from the bottom with a probability p (typically $p = 90\%$). Particles transmitted through the bottom reappear at the top of the chute once again to fall down through it. Particles reflect off the walls of the chute with a partial loss, typically 10%, in their vertical velocity. This is a simple, effective way to model rough walls. The grain polydispersity is varied from 0 to 15% in different simulations [12].

Velocities after collision $\dot{\mathbf{r}}'_1$ and $\dot{\mathbf{r}}'_2$ in terms of velocities before collision, $\dot{\mathbf{r}}_1$ and $\dot{\mathbf{r}}_2$, are

$$\begin{pmatrix} \dot{\mathbf{r}}'_1 \\ \dot{\mathbf{r}}'_2 \end{pmatrix} = \begin{pmatrix} \dot{\mathbf{r}}_1 \\ \dot{\mathbf{r}}_2 \end{pmatrix} + \frac{(1+\mu)}{(m_1 + m_2)} \begin{pmatrix} -m_2 & m_2 \\ m_1 & -m_1 \end{pmatrix} \begin{pmatrix} \dot{\mathbf{r}}_1 \cdot \mathbf{q} \\ \dot{\mathbf{r}}_2 \cdot \mathbf{q} \end{pmatrix} \mathbf{q}, \qquad (2.1)$$

where m_1 and m_2 are the particle masses and $\mathbf{q} = (\mathbf{r}_2 - \mathbf{r}_1)/|\mathbf{r}_2 - \mathbf{r}_1|$ [13, 14]. μ is a velocity-dependent restitution coefficient described by the phenomenological relation [15, 16],

$$\mu(v_n) = \begin{cases} 1 - (1 - \mu_0)(v_n/v_0)^{0.7} & , v_n < v_0 \\ \mu_0 & , v_n > v_0. \end{cases} \qquad (2.2)$$

Here v_n is the component of relative velocity along the line joining the grain centers, μ_0 is the asymptotic coefficient at large velocities (typically 0.9 here), and $v_0 = \sqrt{2ga}$, with g being the acceleration due to gravity and a the radius of the particle [17].
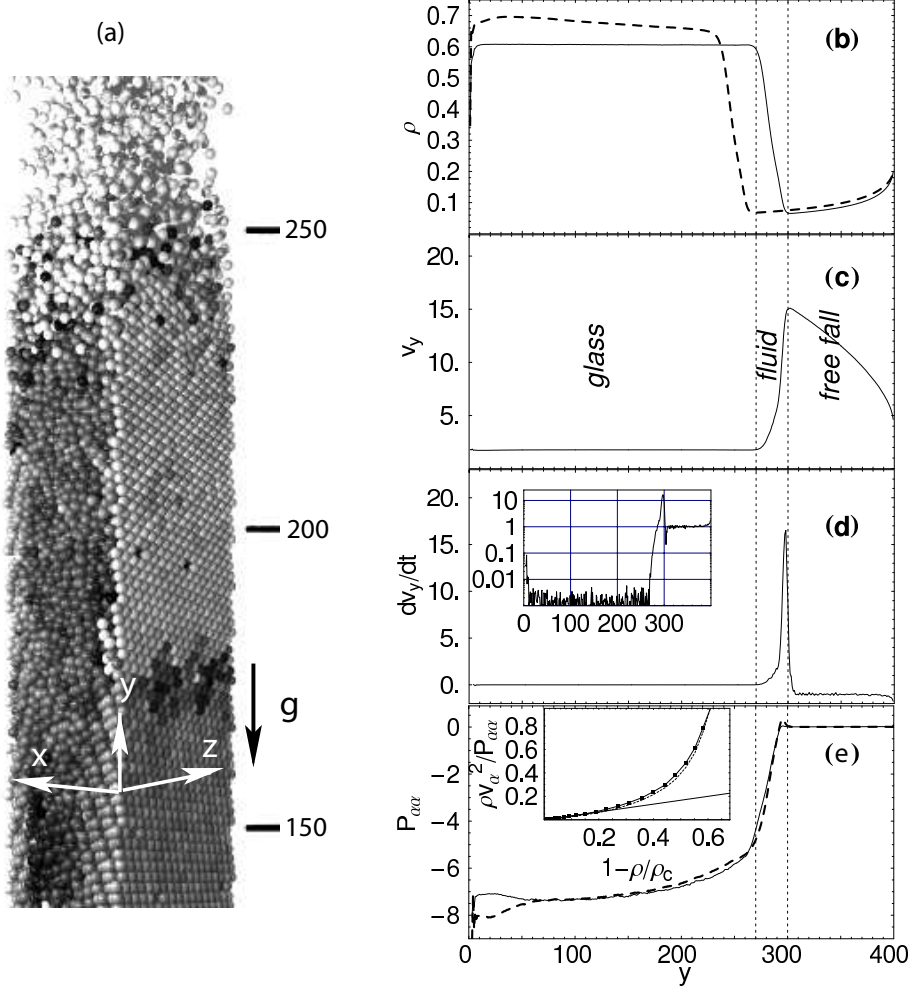
Figure 2.1: (a) Section of a 3D simulation involving 43 200 grains with 1% poly-dispersity in a $32a \times 32a \times 400a$ system. (b) Average density for 1% (dashed line) and 15% polydispersity (solid line) along the height of a 3D chute. For 15% polydispersity, (c) the $y-$velocity and (d) average acceleration, in units of g and as measured by the material derivative $dv_y/dt = \partial_t v_y + v_\alpha \partial_\alpha v_y$. The inset in (d) shows the absolute value of the same data on a log scale, showing the $1g$ accel-eration in the free fall region. (e) shows the pressure tensor components P_{xx} as the solid line and P_{yy} as the dashed line. The inset in (e) shows that the pressure approaches Eq. (2.3) as jamming is approached from the fluid phase [4].

We examine three simulation geometries: "disks", a purely two-dimensional simulation with disks as used in [11]; "spheres in 2D" which are spherical particles in a three-dimensional (3D) simulation kept in a 2D plane by having reflecting front and back walls $2.002a$ apart and with reflecting left and right walls; and "spheres in 3D" which are spherical particles in a chute with periodic front and back walls $16a$ and $32a$ apart and with reflecting left and right walls. In all three types of simulations a sieve is located at the bottom as described above. For simulations it is most convenient to use units where $g = 1$, $a = 1$, and the grain mass $M = 1$. A typical simulation run is $10^4 - 10^5$ time units, equivalent to $2 - 20$ minutes of real time in a system made up of balls 3 mm in diameter.

Steady-state density and velocity profiles for a system similar to that depicted in Fig. 2.1(a) are shown in Fig. 2.1(b) and (c). These profiles are averaged over the $xz-$cross-section of the $32a \times 32a$ chute. Three different regimes are evident. Grains initially placed at the top are little affected by collisions and accelerate uniformly with $\dot{v}_y = -g$, as shown in Fig. 2.1(d). This free-fall region ends abruptly just above the top of the dense column of grains seen in Fig. 3.1(a). There is then a short fluid region extending about $25a$ between the free-fall and glassy region. The grains behave like a simple fluid in this region, with a parabolic profile of the v_y velocity typical of Poiseuille flow ($\square$'s in Fig. 2(b)). For nearly monodisperse systems, the density increases rapidly in this region until it reaches the random close-packed volume fraction of ~ 0.64. Except for a small region at the bottom, the remainder of the system has a density greater than 0.64 indicating partial crystallization. For systems of particles with 15% polydispersity, the density remains constant at 0.6 and is in a glass-like state. As a result we will now concentrate on 15% polydisperse systems as they are more uniform.

Fig. 2.2(b) shows the v_y plug profile ($\blacksquare$'s) along with the corresponding shear stress profile in the glassy region of such a system. Clearly, the system supports a finite shear stress in the central region thus justifying calling this a glass. In
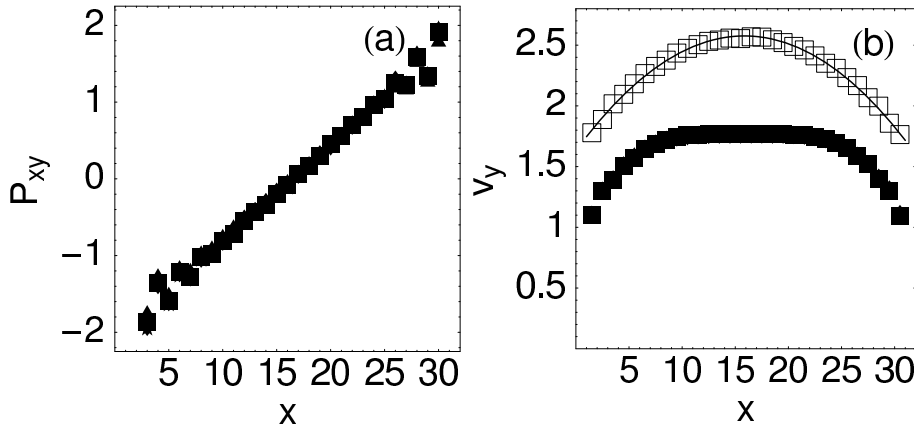
Figure 2.2: Shear stress and velocity profiles for the 15% polydisperse 3D simulation. Data in the glassy region for $h =$50, 100, 150, 200 are plotted separately but fall on top of each other (■'s). The □'s in (b) show the velocity profile in the fluid region at $y = 280$ which gives a parabolic profile (solid line).

steady state, the weight of the system, ρg can be supported by either a pressure gradient $\partial_y P_{yy}$ or by a gradient in the shear stress $\partial_x P_{xy}$ (pressures and stresses are measured as in [11]). A comparison of $\partial_y P_{yy}$ and $\partial_x P_{xy}$ (cf. Fig.s 3.1(e) and 2.2) shows that the shear stress, and hence the walls, carry most ($\sim 98\%$) of the weight.

As jamming is approached, Donev et al. [4] showed that the pressure in a classical (conservative) hard sphere glass approaches

$$P = D(\rho k_B T)(1 - \rho/\rho_c)^{-1}, \tag{2.3}$$

where D is the dimension, k_B is Boltzmann's constant, and ρ_c is the close-packed density. As can be seen in the inset in Fig. 2.1(e), the diagonal components of the pressure tensor do approach this value as ρ approaches ρ_c. However, there are small systematic deviations in the glassy phase, probably due to the dissipation and the fact that the velocities are not Maxwell distributed [18] as assumed in the derivation of Eq. 2.3.

It is reasonable to doubt the capability of a simple binary collision model to de-
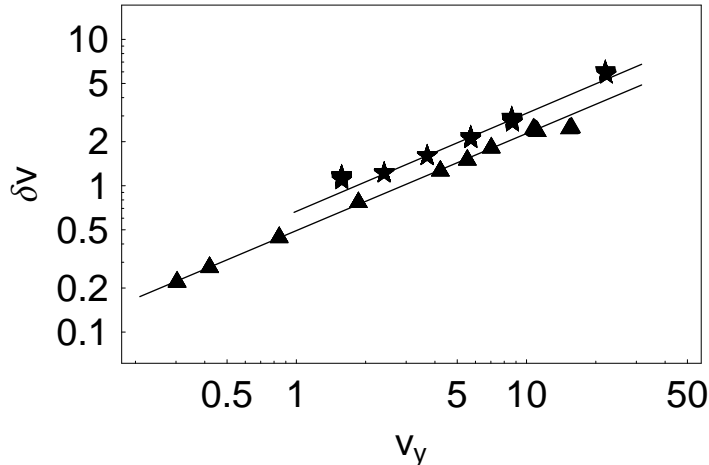
Figure 2.3: Relationship between fluctuating and flow velocity in the glassy region. Data were averaged in directions normal to $\vec{\mathbf{g}}$ for the 32x32 ($\star$, $\delta v = \left(\delta v_x^2 + \delta v_y^2 + \delta v_z^2\right)^{1/2}$) and 16x16 ($\blacktriangle$, $\delta v = \delta v_y$) 15% polydisperse systems. The fitted lines have slope of 2/3, in agreement with the experiments of [9]. v_y is varied by varying the probability of reflection p from 0.01 to 0.995.

scribe the dense glassy phase [19]. However, it is capable of reproducing a number of experimental results related to this dense phase. For example, experiments have shown [9] that the fluctuating velocity $\delta\mathbf{v}$ is related to the flow velocity $\mathbf{v}$ by a power-law relationship $\delta\mathbf{v} \propto \mathbf{v}^{2/3}$. We observe the same relationship (Fig. 2.3). Velocity fluctuations are not, however, isotropic. In a equilibrium fluid, fluctuations in the velocity are governed by equipartition and $\delta v_y^2 = \langle v_y^2 \rangle - \langle v_y \rangle^2$ is the same as δv_x^2 and δv_z^2. This is very nearly the case in what we label the fluid region, but is not at all the case in the unequilibrated free fall region or in the glassy region. Further measurements, such as that of the kurtosis of the velocity distribution, showed that the distribution of velocities is not Boltzmann-distributed.

Considerable attention has also been focused on relating the force/impulse and collision time distributions to jamming. A collision time is defined as the time between two consecutive collisions for a particle. In a simple fluid the collision times are distributed exponentially and the mean collision time (or "relaxation time") is proportional to the mean free path, the typical distance traveled between

collisions. This is indeed what we observe in what we call the "fluid" region of the simulations, as shown in Fig. 2.4(a). The distribution of collision times can be used to test the validity of many of the assumptions that go into standard kinetic theories used to describe granular gases and show us how they break down as we move into the dense glassy regions. As we will show, the distribution can also distinguish between a disordered glass and a crystalline packing of grains.

The distributions of the collision times $N(\tau)$ for binary collisions are shown in Fig. 2.4. For the glassy region of the 15% polydisperse systems (Fig. 2.4(b)), $N(\tau)$ follows a power law,

$$N(\tau) \sim \tau^{-\alpha} \qquad (2.4)$$

where α is 2.81 ± 0.06 for distributions of grain-grain collisions in all the geometries, *regardless of dimension.* The power-law behavior of $N(\tau)$ is independent of the specific choice made for the coefficient of restitution (as long as it is less than 1), and whether or not we use a constant or velocity-dependent coefficient of restitution as in Eq. 2.2. We also examined the distribution of the distance particles travel between consecutive collisions. It has the same power-law behavior as the collision time distribution and we will therefore concentrate on the collision time distribution here.

Experiments often refer to systems with less than 5% polydispersity as monodisperse. However, truly monodisperse systems eventually crystallize and give a power law with $\alpha = 4$ as shown in Fig. 2.4(c) (3D monodisperse systems did not crystallize over the entire system so the 3D data in Fig.2.4(c) are taken from a crystallized region). However, we find significant differences between even 1% polydisperse and truly monodisperse systems and systems with 7.5% polydispersity yielded the same power laws as the 15% system. It appears that the polydispersity is a critical factor in these calculations mainly due to its effect on breaking up crystalization.
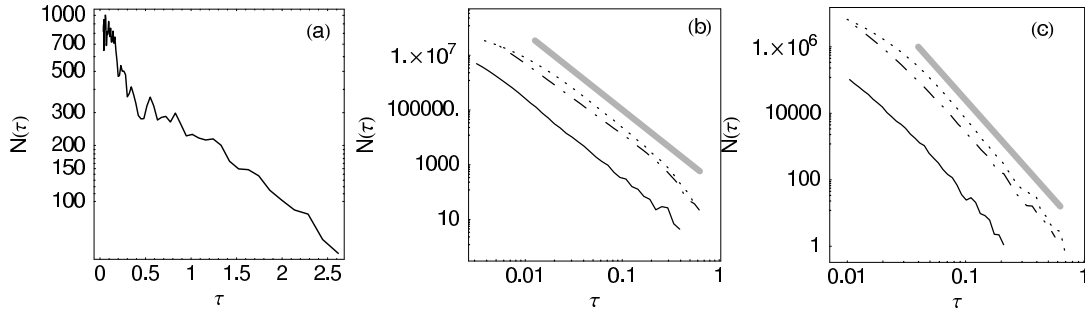
Figure 2.4: (a) Unnormalized collision time distribution in the fluid region of a 15% polydisperse "3D spheres" simulation showing an exponential distribution. (b) Unnormalized collision time distributions in the center of the glassy region for 15% *polydisperse* "disks" (dash-dotted line), "spheres in 2D" (dotted line), and "3D spheres" (solid line) showing a power-law with exponent 2.85 as indicated by the thick gray line. (c) Similar to (a) but for *monodisperse* particles that have crystallized. The power-law in this case has exponent 4 as indicated by the thick gray line. Note, plots in (b) and (c) are log-log plots whereas (a) is a *semi*-log plot. All distributions are averaged over time in a region slightly larger than a grain size in the x and y directions and over the entire z direction. The precise choice of the location, other than it being clearly in the appropriate region, does not change the result.

The significance of the power-law distribution of collision times lies in the fact that it implies that collisions are not statistically independent events. If they were independent, it is straightforward to show (as shown in Chapter 1) that the distribution of collision times would be exponential, or at least it would have an exponential tail [20]. This does not necessarily suggest a breakdown of the model based on binary collisions, suggested for other reasons in Ref. [19]. It does however suggest a breakdown in any kinetic theory arguments based on the Boltzmann equation which relies on the underlying assumption of molecular chaos and the statistical independence of collisions. Similarly, hydrodynamic descriptions which are based on a Chapman-Enskog expansion of the Boltzmann distribution break down. This is due to the breakdown in the statistical independence of collisions, not because ternary collisions are required to describe the system. Thus, the collision time distribution can differentiate a granular fluid (exponential), a granular crystal (power law $\alpha = 4$), and a granular *glass* (power-law $\alpha = 2.8$).
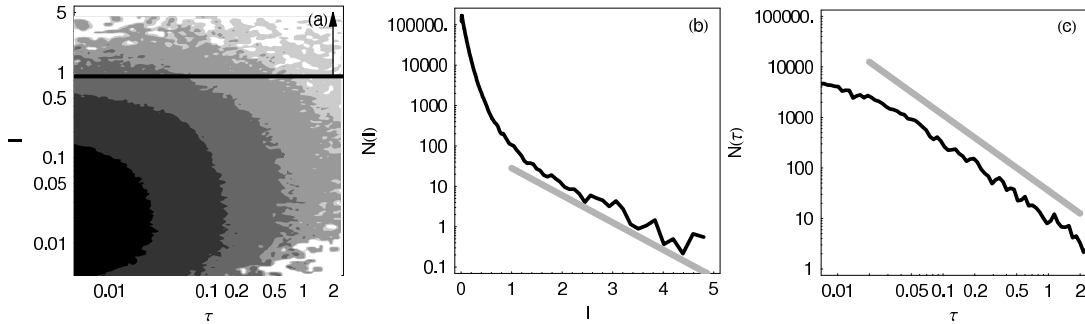
Figure 2.5: (a) Two-dimensional distribution of impulses and collision times (log scales) for a 15% "spheres in 2D" polydisperse simulation. The horizontal solid line in (a) indicates the cut-off in impulses, coinciding with the exponential tail of the 1D impulse distribution shown in the semi-log plot (b), that results in the 1.5 collision time power-law observed in (c). Integrating the two-dimensional distribution in (a) over all collision times gives the 1D histogram of impulses shown in (b). Including only those impulses in the exponential tail of the impulse distribution (b), we obtain the 1.5 collision time power law as shown by the thick gray line in (c).

Typically an exponential force distribution or impulse distribution is considered a signature of jamming. It has been suggested, however [5, 6, 7], that an upturn at the lower end of the impulse distribution may provide more information. Impulse distributions from our spheres in 2D simulation, as shown in Fig. 2.5(b), have a power law *upturn* at the low impulses and an exponential tail at the high impulses. The power law at the lower impulses appears to be more a signature of jamming as even the granular fluid phase exhibits an exponential tail.

Our "spheres in 2D" simulation is a direct analog of the experiment described in [10], the main difference being that the experiment discharged the grains from a hopper at the bottom of the chute whereas we use a sieving process at the bottom. The experiment used a pressure transducer attached to the chute wall to detect grain-wall collisions, and to measure impulses and times between collisions. However the experiment primarily sees an exponential distribution of impulses, although there is an upturn at small impulses for the slower flows. Further, for the distribution of grain-wall collision times they found a power-law with exponent

$\alpha = 1.5$. Based on the distribution of impulses, we explain the main discrepancy not as a surface versus bulk effect but as a result of experimental response time and sensitivity of the detector as follows. If we remove collisions with impulses in the power-law part of the distribution (i.e., the small impulse end that may be difficult to resolve experimentally) by putting in a cut-off at low impulses, we also get the 1.5 collision time power law found in the experiment [10], as shown in Fig. 2.5.

In conclusion, power laws with exponents independent of dimension were found for the distribution of collision times. Further, polydispersity and disorder are directly related to the power law exponent. The collision time distribution is an exponential for a granular fluid, a power-law with exponent $\alpha = 4$ for a granular crystal, and a power-law with exponent $\alpha = 2.8$ for a granular *glass*. It is interesting to note that the propagations of stress seems to show a similar ability to discern crystal and glass [3]. We successfully compared our collision time power law distribution with the experiment described in [10]. By subtracting out the collisions with very small impulses that would be difficult to measure experimentally, we found that the stronger collisions that make up the exponential tail of the *impulse* distribution have an associated collision time distribution with power law exponent 1.5. This highlights the importance of simulations that can give access to information not easily accessible in experiments. Measurement of the full collision-time distribution in experiments would require accessibility to the measurement of very low impulse collisions. In some systems this might be precluded by inelastic collapse and prolonged contacts. However, groups have observed peaks in the low end of the force distribution for static systems [5, 7] so it seems likely that a similar measurement of impulses in the analogous dynamic case could see the full spectrum of phenomenon we find in simulations.

thank N. al Tarhuni for performing some preliminary simulations.

REFERENCES

[1] H. Jaeger, S.R. Nagel, and R.P. Behringer, Rev. Mod. Phys. **68**, 1259 (1996).

[2] D.M. Mueth, H M. Jaeger, S.R. Nagel, Phys. Rev. E **57**, 3164 (1998).

[3] J. Geng, D. Howell, E. Longhi, R.P. Behringer, G. Reydellet, L. Vanel, E. Clément, S. Luding, Phys. Rev. Lett. **87**, 035506-1 (2001).

[4] A. Donev, S. Torquato, and F. H. Stillinger, Phys. Rev. E **71**, 011105 (2005).

[5] C. S. O'Hern, S. A. Langer, A. J. Liu and S. R. Nagel, Phys. Rev. Lett. **86**, 111 (2001).

[6] A. Ferguson and B. Chakraborty, Phys. Rev. E **73**, 011303 (2006).

[7] L.E. Silbert, D. Ertas, G.S. Grest, T.C. Halsey, D. Levine, Phys. Rev. E **65**, 051307 (2002).

[8] J.-C Tsai and J.P. Gollub, Phys. Rev. E **70**, 031303 (2004).

[9] N. Menon and D. Durian, Science **275**, 1920 (1997).

[10] E. Longhi, N. Easwar and N. Menon, Phys. Rev. Lett. **89**, 045501 (2002).

[11] C. Denniston and H. Li, Phys. Rev. E **59**, 3289 (1999).

[12] polydispersity $= 15\%$ $\Rightarrow$ standard deviation of particle radii is 0.15 if mean is 1.

[13] J. T. Jenkins and S. B. Savage, J. Fluid Mech. **130**, 187 (1983).

[14] S. B. Savage and D. J. Jeffrey, J. Fluid Mech. **110**, 255 (1981).

[15] C. Bizon, M. D. Shattuck, J. B. Swift, W. D. McCormick and H. L. Swinney, Phys. Rev. Lett. **80**, 57 (1997).

[16] S. Luding, E. Clement, J. Rajchenbach, and J. Duran, Europhys. Lett **36**, 247 (1996).

[17] Typical fluctuation velocities are $\delta v = 0.05$ implying $\mu \approx 0.99$.

[18] S. Moka and P.R. Nott, Phys. Rev. Lett. **95**, 068003 (2005).

[19] J.-C. Tsai, W. Losert, G. A. Voth and J. P. Gollub, Phys. Rev. E. **65**, 011306 (2001).

[20] F. Reif, *Statistical and Thermal Physics*, (McGraw-Hill, New York, 1965), p. 461.

CHAPTER 3

Velocity fluctuations in dense granular flows

3.1 Introduction

Dissipative granular fluids are difficult to characterize because they are typically not in any sort of equilibrium state. Unlike a closed system of elastic particles, an initially homogeneous steady-state dissipative granular fluid typically develops nonuniform, and even singular, spatial variations in density, momentum density, and temperature [1, 2]. Even static granular systems are typically the result of such a rapid quench in temperature that they are in glasslike states and hence not easily described by equilibrium thermodynamics [3]. It is, however, possible to produce a fairly homogeneous steady-state system if there is a steady energy input to compensate for the energy lost in collisions. This can be achieved by vibrating the system (or a wall), shearing the system, allowing grains to fall in a chute, or adding stochastic noise (in a simulation).

Theoretical and computational studies of steady state suggest that these inelastic systems can be subdivided into phases with different velocity distributions [4, 5, 6, 7, 8]. For instance, Esipov and Poschel [4] suggested the existence of a granular gas, a condensed phase and a collapsing condensed phase. They arrived at these phases by studying analytically the kinetic energy distribution function

satisfying the Boltzmann equation. They also studied this function numerically for a system composed of a circular wall maintained at a constant temperature, enclosing inelastic hard disks with binary collisions and found that their analytical formulation suited the simple cases of steady-state flows. Noije and Ernst [5] solved the nonlinear Enskog-Boltzmann equation for a freely evolving and a heated system of hard disks or spheres and found that their freely evolving system coincided with the result of Esipov and Poschel. Ernst and Brito [6, 7] analyzed the nonlinear Boltzmann equation by adding a stochastic noise or stochastic force to the microscopic equations of motion. They considered three types of thermostats, namely a Gaussian thermostat, a white noise thermostat and a gravity thermostat and found that the form of the high energy tails in the velocity distributions, whether it be Gaussian, stretched exponential, or power-law depends on the type of thermostat and on the type of interaction model. Ben-Naim and Machta [8] performed theoretical derivations and numerical simulations of inelastic gases to study stationary velocity distributions that obey the Boltzmann equation and found that their velocity distributions have a high-energy tail corresponding to a range from high to low velocities, and that steady states can be realized by injecting energy at high velocities. They randomly raised particles to high velocities such that energy was injected only at the tail of the distribution. This did not change the collision dynamics but rather set a scale for the most energetic particles. While these studies have given insight into granular dynamics, experiments rarely have an analog of stochastic noise or direct injection at one end of the spectrum or other easily controlled energy input.

There have been many experiments in which velocity distributions have been measured. Several experiments have studied granular flow in a vertical channel [9, 10, 11]. Savage [12] used fiber-optic probes to measure velocity profiles in a vertical channel at the sidewalls. Natarajan, Hunt and Taylor [9] found that their velocity measurements showed that the vertical flows had a central uniform flow

region and a shear flow region close to the vertical side walls. They also found that the magnitude of the velocity fluctuations in the transverse direction increased from the center towards the side walls. Menon and Durian [13] used diffusing-wave spectroscopy to measure fluctuation velocities of glass beads in a vertical chute and found a power-law relationship between mean fluctuation velocities and flow velocity. Losert, Cooper, Delour, Kudrolli and Gollub [14] used a vibrated granular experiment in which they measured velocity statistics for a layer of inelastic colliding beads driven by a vertically oscillating boundary. They found that when the external excitation was high enough to generate accelerations 3-8 times that of gravity, the probability distribution of the horizontal velocity $P(v) \sim \exp\left(-|v/v_c|^{1.5}\right)$. For cooler particles in the absence of excitation, they found an exponential velocity distribution. Rouyer and Menon [15] similarly used vertical vibration of a vertical plane to measure velocity fluctuations to arrive at $P(v) \sim C \exp\left[-\beta \left(|v|/\sigma\right)^{\alpha}\right]$ with $\alpha = 1.55 \pm 0.1$ at all the frequencies and amplitudes that they used. Recently Moka and Nott [16] used video imaging and particle tracking to measure particle velocity distributions in slowly flowing granular material down a vertical channel. They found an abrupt change in the mean velocity in shear layers near the sidewalls, but a constant velocity in the middle region. However, in contrast to [9, 17, 18], they found velocity fluctuations to be larger in the center of the channel than at the sidewalls. They found the velocity distribution to be non-Gaussian and anisotropic, following a power law at larger velocities, and that this distribution was identical in the outside shear layer and in the middle core. We will compare our simulation results with many of these experiments throughout this paper. As we shall show, the velocity distributions measured in these experiments are very different in different regions and a consistent interpretation of experiment therefore requires knowledge of what phase is being studied. One of the advantages of the system we are studying is that, as we will demonstrate below, we are able to visualize each of these phases in a steady-state configuration which is easily realized experimentally.

In this paper we will look at velocity distributions in the gravity-driven flow shown in Fig. 3.1. The simulation is set up to mimic experiments on chute-flow [9, 12, 13, 16]. Spherical grains are dropped in from the top of a rectangular chute and fall under the influence of gravity. There are flat walls at the left and right (x direction) of the chute and periodic boundary conditions at the front and back (z direction). At the bottom of the chute ($y = 0$), there is a sieve which controls the flow rate. When a particle leaves the bottom a new particle is placed at the top to maintain a constant number of particles in the system. We studied a similar system in a recent letter [19] (Chapter 2) and in two dimensions (2D) in an earlier work [21]. Based on the distributions of times between collisions, we found our simulation had three regions or phases, which we labeled and justified as a glassy region, a fluid region and a free-fall region. We found there was a different collision time distribution for each of these three distinct phases [19]. In the present study we also find these three phases can be characterized by the form of their respective velocity distributions.

In the first section we describe the simulations and the steady state configuration of the mean velocity and velocity fluctuations. We then examine the distribution of velocity fluctuations in detail. Different velocity distributions are found depending on whether the system displays characteristics of a fluid or a glass. The apparently conflicting results seen in experiments [9, 16] are found to be related to different phases in our simulations. We then examine the relation of the velocity fluctuations to the distribution of times between collisions. We find evidence that the transition from one class to another may correspond to a second order dynamical phase transition in the limit that the vertical flow speed goes to zero.
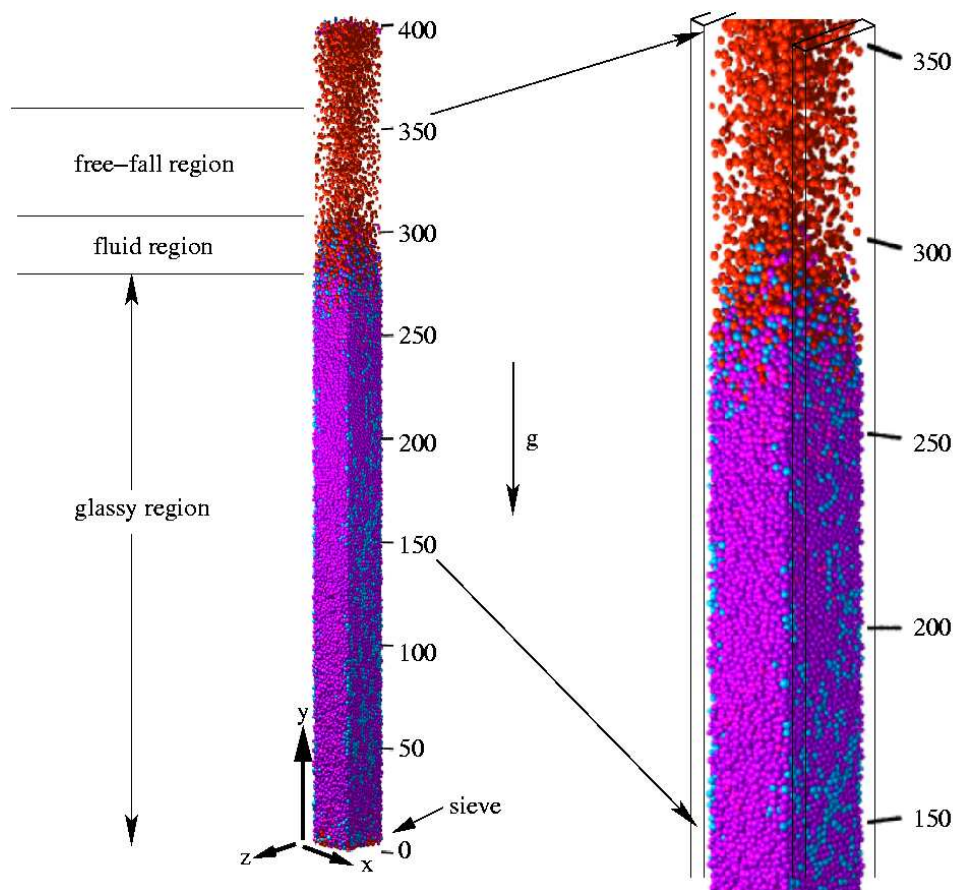
Figure 3.1: Section of a simulation involving 43 200 grains with 15 % polydispersity. The system size is $32a \times 32a \times 400a$. There are reflective walls at $x = 0$ and $x = L_x$, periodic boundary conditions in the z direction, and a finite probability of reflection at the bottom of the chute (at $y = 0$).

3.2   Model

A typical snapshot from one of our simulations is shown in Fig. 3.1. As indicated in Fig. 3.1, there are three regions, which we label as a glassy region, a fluid region and a free-fall region. These labels will be referenced throughout this paper and were justified in our previous study [19]. Spherical grains are dropped in from the top of a rectangular chute in the free-fall region and the grains accelerate at $1\,g$ where g is the acceleration due to gravity (units are given in footnote [20]). There are flat walls at the left and right (x direction) of the chute and periodic boundary conditions at the front and back (z direction). This geometry is similar to that studied experimentally in [16] where similarly rough sidewalls were used. Periodic boundary conditions in z reduce wall effects and allow us a translationally invariant direction to average data over. In experiments a similar situation is obtained by having a system much longer in z than x. At the bottom of the chute ($y = 0$), grains are reflected with a probability p (typically $p = 90\%$) which models a sieve at the bottom of the chute. This has the same effect as a mesh that was used in the chute experiment described by Menon and Durian [13]. By using a sieve to restrict our flow of particles, we are also able to model other experiments that use a restricting outlet as in the experiment by Moka and Nott [16]. As detailed later, we were able to reproduce the results of both of these experiments. We maintain a constant number of particles in our simulation by having new particles placed at the top of the chute when an old particle leaves the bottom. We ran simulations with different initial conditions for grains at the top of the chute, for instance we started particles at rest at the top of the chute and let them fall under the influence of gravity, gave them random velocities equal to the grains leaving the system at the bottom, and found no change in our results that are reported in this paper or in our previous paper [19] (Chapter 2).

The velocities of two grains after collision $\dot{\mathbf{r}}'_1$ and $\dot{\mathbf{r}}'_2$ in terms of the velocities

before collision, $\dot{\mathbf{r}}_1$ and $\dot{\mathbf{r}}_2$, are

$$
\begin{pmatrix} \dot{\mathbf{r}}_1' \\ \dot{\mathbf{r}}_2' \end{pmatrix} = \begin{pmatrix} \dot{\mathbf{r}}_1 \\ \dot{\mathbf{r}}_2 \end{pmatrix} \tag{3.1}
$$
$$
+ \frac{(1+\mu)}{(m_1+m_2)} \begin{pmatrix} -m_2 & m_2 \\ m_1 & -m_1 \end{pmatrix} \begin{pmatrix} \dot{\mathbf{r}}_1 \cdot \mathbf{q} \\ \dot{\mathbf{r}}_2 \cdot \mathbf{q} \end{pmatrix} \mathbf{q},
$$

where $\mathbf{q} = (\mathbf{r}_2 - \mathbf{r}_1)/|\mathbf{r}_2 - \mathbf{r}_1|$, and μ is the coefficient of restitution. Such collision models of granular flow have a long history [22, 23]. μ is a velocity-dependent restitution coefficient described by the phenomenological relation [24, 25, 26],

$$
\mu(v_n) = \begin{cases} 1 - (1-\mu_0)(v_n/v_0)^{0.7} & , v_n \leq v_0 \\ \mu_0 & , v_n \geq v_0. \end{cases} \tag{3.2}
$$

Here v_n is the component of relative velocity along the line joining the grain centers, μ_0 is the asymptotic coefficient at large velocities, and $v_0 = \sqrt{2ga}$ [27]. Equation (3.2) effectively makes the ball collisions become more elastic as the collisions become weaker as seen in experiments [24, 25, 26].

Experiments clearly show that the weight of a dense column of grains is supported by the walls [28, 29]. This is also desirable in a simulation as it will lead to a pressure independent of height in the dense glassy region. Specular reflection will *not* accomplish this. In experiments, spin and tangential friction would result in a loss of vertical momentum at rough-surfaced walls. While we do not have spin and friction in our simulation, we need a vertical loss to model the experiment. We achieved this by modeling the left and right walls as rough walls by having particles reflect off the left and right walls of the chute with a partial loss, typically 10% in their vertical (y) velocity. The precise value of the partial loss made little qualitative difference. Rough walls enabled our flowing grains to see a wall support and a shearing regime similar to that found in experiments [9, 16].
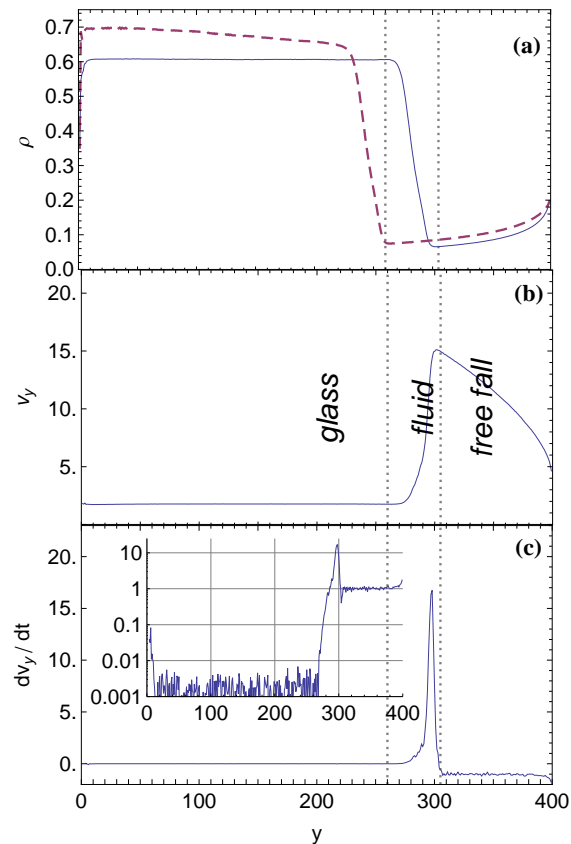
Figure 3.2: Average (a) density (volume fraction) for 1% (dashed line) and 15% polydispersity (solid line) along the height of a 3D chute. For 15% polydispersity, (b) the y velocity and (c) the average acceleration as measured by the material derivative. The inset in (c) shows the same data on a log scale, clearly indicating the acceleration of 1 g down in the free fall region. This justifies the "free fall" label. Note that this plot takes an absolute value so the acceleration is actually -1 g and changes sign at a height of 300. This is for a 3D $32a \times 32a \times 400a$ 15% polydisperse simulation with an asymptotic coefficient of restitution $\mu_0 = 0.9$.

A parameter that turns out to be surprisingly important is the polydispersity of the grain sizes. Here, we use a Gaussian distribution of grain radii and a polydispersity of 15% means that the standard deviation of the particle radii is 0.15 if the mean radius is 1. Typically even experiments that use "monodisperse" grains have some small polydispersity on order of a few percent. We have performed simulations at a range of polydispersity from 0 to 15% and find even a few percent can give significantly different results from pure monodisperse systems. This is because the geometry in the packing of particles of different sizes dictates whether particles crystallize (in the monodisperse case) or go into a glassy state (in the polydisperse case). This has a significant impact on collision time power laws [19] (Chapter 2).

3.3   Steady State Configuration

We started a configuration with particles racked in a three-dimensional (3D) rectangular array with a Gaussian distribution of randomized initial velocities with standard deviation 0.8. From this initial configuration, we ran our simulation and we plotted the number of collisions over time. When the total number of collisions per unit time remained level over time, our simulation had reached steady state. For our 3D system, steady state was achieved after approximately 100 time units, enough time for all grains to move through the system once.

The number of grains was chosen small enough that there would be a large free-fall region at the top (so the results would not depend on specifics of the injection at the top) but large enough so that there would also be a large glassy region (50% - 65% of the volume of the system). Flow velocity is controlled by the reflection probability p at the sieve. However, the qualitative behavior and division into 3 phases does not depend significantly on the flow velocity until the sieve restriction

is nearly removed (near $p \leq 0.10$).

Typical steady state configurations of the local density, measured as volume fraction, and vertical (y) velocity down the center of the chute are shown in Fig. 3.2 as a function of y (height). A clear difference in the density profile of a nearly monodisperse (1%) (dashed line in Fig. 3.2(a)) and the system with 15% polydisersity (solid line) is clearly visible. In the more polydisperse system the density in the region we have labeled as fluid steadily increases until it hits 0.60 volume fraction and is then constant in the main bulk of the column. However, the nearly monodisperse system shows a steady, nearly linear, increase in density from a volume fraction of 0.64 to nearly 0.70 near the bottom of the channel. This indicates that the nearly monodisperse system continues to order (i.e., crystallize) as it travels down the channel, even in the very dense region.

As previously indicated there are three regions, which we label as a glassy region, a fluid region and a free fall region. These labels were justified in our previous work [19] (Chapter 2). In the free-fall region the grains accelerate at $1\,g$ and collisions are rare enough that the acceleration is unimpeded as shown in Fig. 3.2(c). In the liquid region the density is sufficiently high that collisions mix the grains, but the distribution of collision times (the time between collisions for a given grain) is exponential, meaning that collisions are largely independent. In the glass region, the collision time distribution is a power-law and thus there are collisions at a wide range of time scales [19]. We should emphasize, as shown in [19] (Chapter 2), that mono-disperse systems continue to crystallize so they are not truly a glass.

The velocity profile in a cross section of the flow is also very different in the fluid and glass regions. As can be seen in Figs. 3.3(a) and 3.3(b), in the fluid region the fluid velocity fits a parabolic flow as expected for a fluid with a constant viscosity in a pressure gradient (Poiseuille flow) [30]. In the glassy region, jamming or
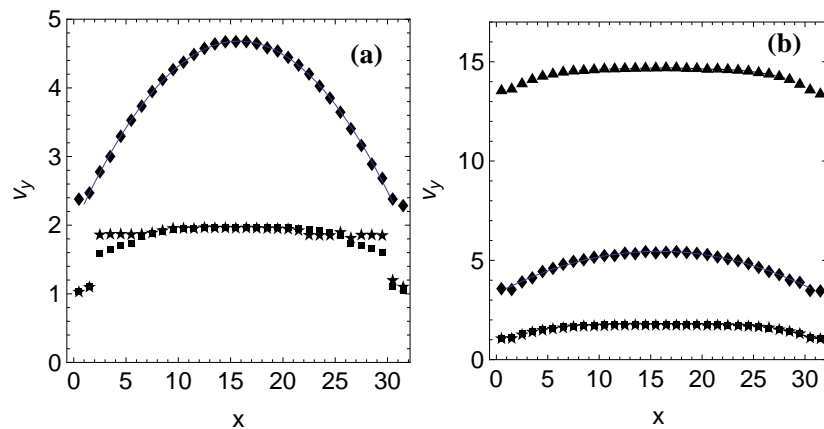
Figure 3.3: Vertical velocity profiles along a width of 3D chute in 32 by 32 systems at different heights. (a) is for 1% polydisperse systems with ◆ in the fluid phase at $y = 250$ (averaged over 500 time units), ■ in the disordered solid phase at $y = 200$, and ⋆ in the crystallized phase at $y = 150$ (averaged over 5 time units). (b) is for a 15% polydisperse system at different heights with the ▲ in the transition region of the free-fall to fluid phase at $y = 310$ (this plug profile was similar in the transition region of the free-fall to fluid phase for the 1% polydisperse system), ◆ in the fluid phase at $y = 290$ and the others in the glassy phase. The lines in the fluid phase are fits to a parabola. The discontinuities in (a) indicate fracture and while these discontinuities move around somewhat over time, the average profile does not become smooth.

plasticity occurs giving way to a plug type profile in the 15% polydisperse case. More pronounced kinks occurs in the 1% polydisperse (nearly monodisperse) case as shown by the $\star$'s in Figure 3.3(a). These kinks are associated with fracture along crystal domain walls. Similar profiles are seen in two-dimensional flow where it is easy to see the crystallization and domain walls (see Figure 3.4). This crystallization is not seen initially in the mono-disperse systems, but once it develops it persists for the entirety as our longest simulations. This suggests that once a seed crystal forms, it acts as a template for the material coming out of the liquid phase. This and our previous work, which demonstrated different exponents for poly- and monodisperse systems for the power-law distribution of collision times [19] (Chapter 2), suggests that the dynamics of the very dense monodisperse and polydisperse systems are significantly different. The dynamics of the dense polydisperse systems are more akin to regular structural glasses, whereas the dense monodisperse systems are more similar to fracture dynamics in crystalline systems.

The flow profile in the free-fall region depends somewhat on the profile that the grains start with at the top. If the grains start with a uniform distribution of velocities at the top, independent of their x position, then the profile will start out flat. As the grains fall down the channel they are slowed at the wall and the fluidlike phase gradually grows in from the walls. This produces an apparent a pluglike profile as the fluid phase is approached. However, the plug profile here is due to very different reasons than those causing the plug profile in the glassy region. In the glassy region the central portion of the flow is jammed into a true plug, whereas in the free-fall region the plug flow is from the retention of the input profile at the top of the column as shown by the top profile ($\blacktriangle$'s) in Fig. 3.3(b).

The characteristics of the velocity fluctuations $\left(\delta v_\alpha^2 \equiv \langle (v_\alpha - \langle v_\alpha \rangle)^2 \rangle \right)$ $(\alpha = x,\ y,\ z)$ also vary in the different regions. Figure 3.5 shows the profile of the velocity fluctuations in the different regions. In the fluid region (and the free-fall region which
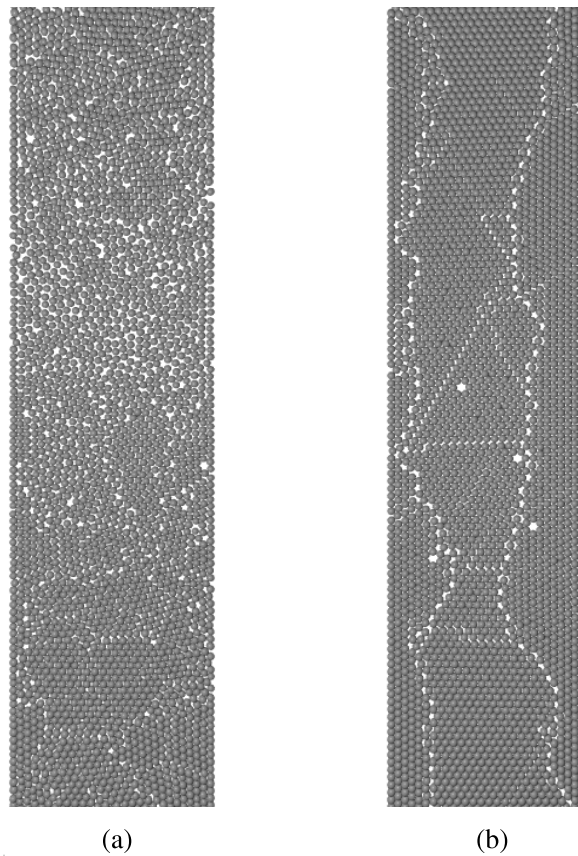
Figure 3.4: Visualization of 2D sphere simulation showing (a) random packing in monodisperse spherical grains at the early stages of the simulation (at time of 200 in simulation units), and (b) crystallization in monodisperse spherical grains at the later stages of the simulation (at time of 3200).
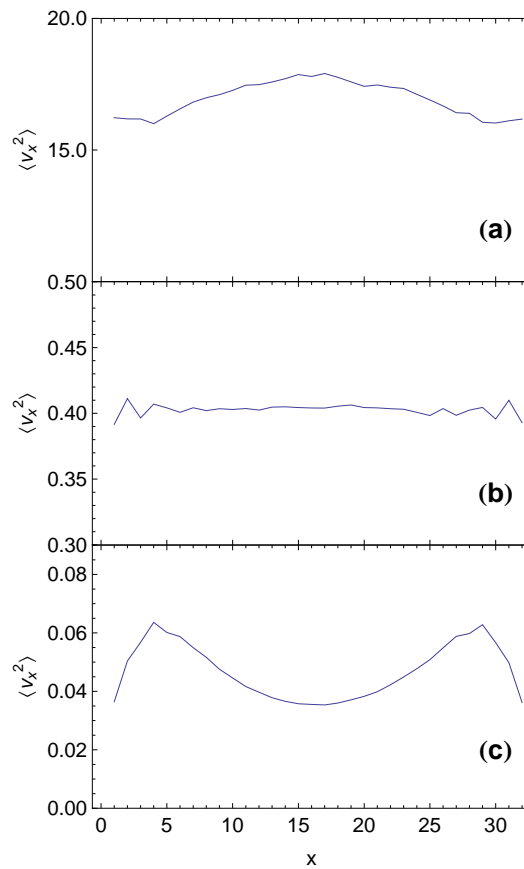
Figure 3.5: Plot of $\langle v_x^2 \rangle$ versus the width x in the (a) fluid, (b) glass-fluid transition and (c) glassy regions for 15% polydisperse 3D simulation. The curves represent data with an asymptotic coefficient of restitution of μ_0 of 0.97. Data are averaged over 10 ball diameters in height.
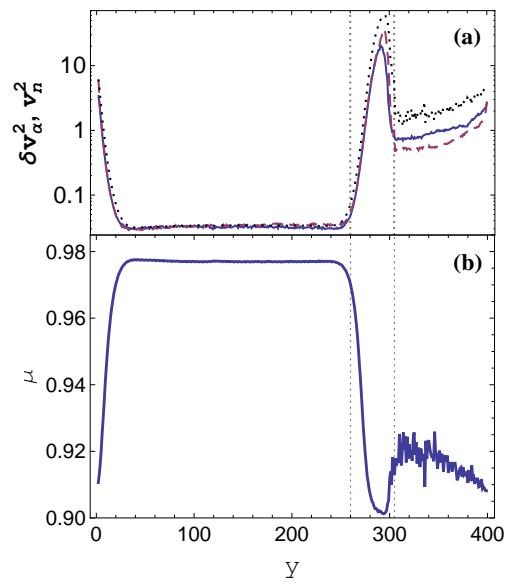
Figure 3.6: Plot of (a) δv_x^2 (solid line), δv_y^2 (dashed line) and the square of the mean relative velocity in normal direction during a collision v_n^2 (dotted line) versus the height for 15% polydisperse 3D simulation with an asymptotic coefficient of restitution $\mu_0 = 0.9$ and (b) the velocity-dependent coefficient of restitution $\mu(v_n)$. Note that plot (a) is a semi-logarithmic plot.

is similar) the grains gain enough kinetic energy between collisions (from acceleration due to gravity) to more than compensate for the loss in kinetic energy in collisions. As a result, the system is hotter ($\delta\mathbf{v}^2$ is bigger) in the middle and heat flows *out* from the center towards the walls (we define the granular temperature as $T \equiv [\langle v_x^2 \rangle + \langle (v_y - \langle v_y \rangle)^2 \rangle + \langle v_z^2 \rangle]/2$ and heat flow is proportional to ∇T). In the glass phase, the system is colder ($\delta\mathbf{v}^2$ is smaller) in the middle and heat flows *in* from the shear zones near the walls. Figure 3.6 shows that $\partial_y T > 0$ in the liquid and free-fall regions, so we expect heat should flow down the channel there, but that there should be no vertical heat flow in the glass (as $\partial_y T = 0$ in the glass). As Fig. 3.6(a) shows, the square of the typical normal velocity v_n^2 encountered in a collision essentially tracks the velocity fluctuations. In the fluid and free-fall region the typical v_n is sufficiently high that $\langle \mu \rangle$ is close to its asymptotic value μ_0. In the glassy region v_n is typically much smaller and $\langle \mu(v_n) \rangle$ is closer to 1.

Elastic hard spheres undergo a fluid-solid phase transition [31]. Inelastic granular systems have a similar transition [32, 33, 34, 35]. Theory suggests that in inelastic systems these phases can be further subdivided into dynamical phases with different characteristic velocity distributions [4, 5, 6, 7, 8]. The different phases we see in our simulations are closely aligned with the phases suggested by Esipov and Poschel [4], as we shall show in more detail below. Experiments, however, often have not clearly identified which phase is being observed. This has lead to what at first appears to be potentially conflicting results. Moka and Nott [16] observe a phase that exhibits plug-like flow and is hotter in the interior of the system. This corresponds to the free-fall to fluid transition region in our system. As in the experiment, our velocity in this transition region (▲'s) of Fig. 3.3(b), also shows a plug profile. This is because the particles at the top of the chute are given random velocities, and thus have, on average, a flat velocity profile at the top. As the particles travel through the free-fall to the fluid transition region this develops into a plug profile as the fluid region grows in at the walls. The corre-

sponding plot of granular temperature shown in Fig. 3.5(a) is hotter in the middle as collisions with the walls are slowing the grains in this region more than in the interior where there are few collisions. More typically, experiments [9, 17, 18] see the interior being colder corresponding to our glassy phase. Clearly, the system supports a finite shear stress in the central glassy region with continuous, plastic deformation along the boundary. This is shown in the plug flow profile in the glassy region of our simulation, ($\star$'s) of Fig. 3.3(b), and in the corresponding plot of granular temperature in Fig. 3.5(c), which shows the temperature to be colder in the middle. As we shall show below, the velocity distributions are very different in these three different regions and a consistent interpretation of experiment therefore requires knowing what phase is being studied. Few experiments tend to pin this down and the implicit assumption appears to be that the entire system is in one phase, something that is clearly not the case. We hope that future experiments will pay more attention to measuring properties such as density and flow rate as a function of height to clearly identify the phases present. One of the advantages of the system we are studying is that we can see all of these phases in a steady-state configuration that can be easily realized and thus studied experimentally.

3.4   Velocity distributions

A normal fluid in local equilibrium in the canonical ensemble has velocity fluctuations $\delta\mathbf{v}$ distributed about the local mean velocity $\mathbf{v}$ in a Gaussian,

$$P(\delta\mathbf{v}) \sim \exp\left(-\frac{\delta\mathbf{v}^2}{k_B T}\right). \tag{3.3}$$

Numerous experiments and simulations [5, 8, 14, 15, 16, 36] have shown that velocity fluctuations in granular materials do not generally follow such a distri-

bution. This is not that surprising as energy is constantly being lost (due to the inelastic collisions) and the assumption of local equilibrium is dubious in most of the system. However, there is also conversion of potential energy to kinetic energy due to the grains falling so the possibility of kinetic energy loss from collisions balancing kinetic energy gain exists, at least in some regions. In fact we find two regions in the system where the distribution of v_x *is* Gaussian.

The first location is in the free-fall region. Grains are placed at the top of the chute at a random x and z position and with a small random velocity ($\langle v_\alpha^2 \rangle$ similar to at the bottom of the chute but from a uniform distribution). Even though the initial velocity distribution is not Gaussian, the velocity distribution at the top becomes Gaussian within 5 ball radii of the top (we measured the distribution every $5a$ from top to bottom). This is not surprising if one recalls the central limit theorem (particles start at top with velocities independent of nearby particles). The v_x distribution remains Gaussian in the free fall region [see Fig. 3.7(a)], but narrows as the grains fall (i.e. the standard deviation $\langle v_x^2 \rangle^{1/2}$ becomes smaller as shown in Fig. 3.6). The distribution narrows as a result of collisions dissipating kinetic energy. This energy could, in principle, be recouped from gains from the conversion of potential energy to kinetic energy, and as we will see below this does affect the v_y distribution. However, the v_x fluctuations are largely decoupled from the v_y fluctuations in the free fall region. This can be seen in the anisotropy of the velocity fluctuations shown in Fig. 3.8 for $\mu_0 = 0.9$. There is a significant difference in the anisotropy in the polydisperse versus monodisperse (1% polydisperse) cases when we compare Fig. 3.8(a) versus Fig. 3.8(b). The reason we find this difference in anisotropy in the glassy phase is that in the monodisperse case, the particles become more ordered and tend to crystallize causing forces to translate along straight line chains of particles. Thus the monodisperse particles become more correlated. In the polydisperse case the particles are more disordered and thus less correlated. We reported this finding in our previous paper [19]
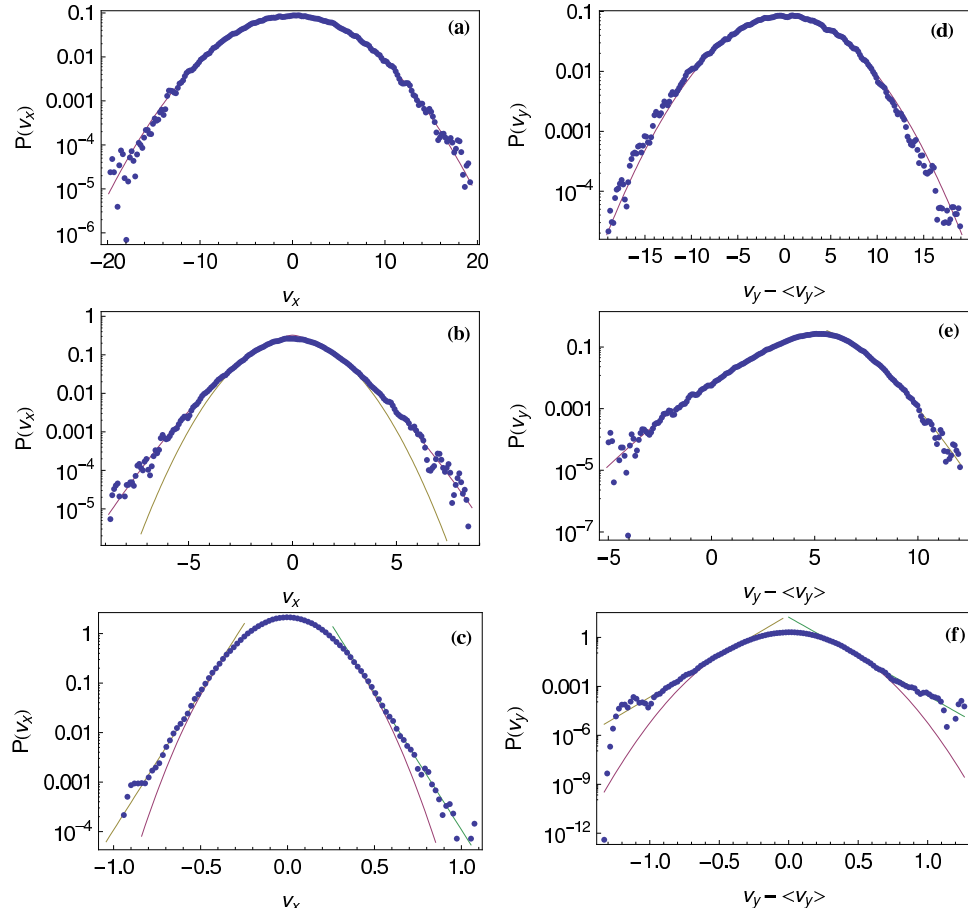
Figure 3.7: x-velocity distributions in (a) free-fall, (b) fluid and (c) glassy region and y-velocity distributions in (d) free-fall, (e) fluid and (f) glassy region for a 15% polydisperse simulation. Note that $\langle v_x \rangle = 0$, so we plotted the x-velocity distribution as $v_x = v_x - \langle v_x \rangle$, whereas $\langle v_y \rangle \neq 0$, so we plotted the y-velocity distribution as $v_y - \langle v_y \rangle$. These velocity distributions were taken at heights in the chute at $h = 300$ in the free-fall region, $h = 270$ in the fluid region, and $h = 190$ in the glassy region. Fits are shown with the solid line. ($\mu_0 = 0.97$). Red curves are fits to $A \exp\left(-\delta v_\alpha^2/v_0^2\right)$. Blue lines are fits to $A \exp\left[-\left(v_\alpha/v_0\right)^\beta\right]$ with $\beta = 1.5$ in (b) and (c).
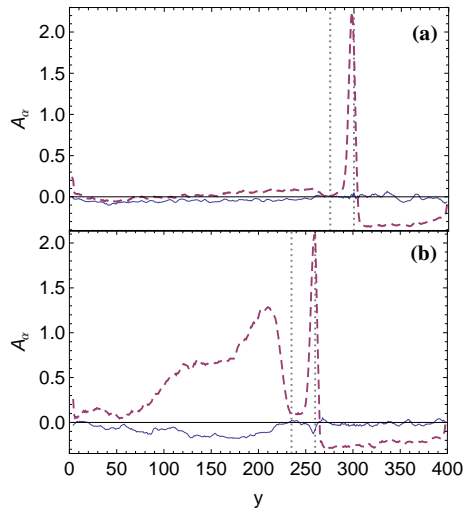
Figure 3.8: $A_\alpha = (\delta v_\alpha^2 - \delta v_x^2)/\delta v_x^2$, the anisotropy in the velocity fluctuations relative to the x direction. A_y (dashed line) and A_z (solid line) are shown for the 3D (a) 15% polydisperse system and (b) 1% polydisperse (essentially monodisperse) system with an asymptotic coefficient of restitution $\mu_0 = 0.9$. The vertical dashed lines indicate the fluid transition region.

(Chapter 2). In the remainder of the paper we will focus on the 15% polydisperse systems. Also, in the free fall region, δv_x^2 and δv_z^2 differ significantly from δv_y^2. In the transition from free-fall to fluid, this anisotropy abruptly changes sign and then drops close to zero in the liquid phase. We will discuss this transition region more below after we have discussed the distributions in the main phases.

In the fluid phase, the v_x distribution fits a Gaussian at low v_x but has stretched exponential tails as shown in Fig. 3.7(b). These tails gradually fill in the whole distribution to the point where the entire distribution can be well fit to a function $A \exp(-(|v_x/v_0|^\alpha)$, with $\alpha = 3/2$, as shown in Fig. 3.7(b). Similar velocity distributions (with the same $\alpha = 3/2$) have been measured in experiments on *driven* granular systems [14, 15]. Such a distribution has also been shown to be a solution to the Boltzmann equation for a system of heated (i.e., with stochastic noise) granular fluid by Noije and Ernst [5] and as a special case of more general multiplicative driving [37]. In our case, the driving is not stochastic (the grains are

converting gravitational potential energy into kinetic energy deterministically). However, in the fluid phase the dynamics are apparently sufficiently chaotic to mimic the stochastic noise used in [5, 37]. In the free-fall region the direction of particle motion is predominantly downward with gravity whereas in the fluid region there are more sideways particle collisions which couple the velocity fluctuations in all directions (the anisotropy seen in Fig. 3.6 disappears). Thus the net result (i.e. the form of the distribution) has the same velocity distribution (with the same $\alpha = 3/2$) in the fluid region as is seen in simulations with stochastic noise. It would appear that the stochastic nature is actually essential as the velocity distributions do *not* have this shape in the free-fall regions, where the grain trajectories are too independent to induce chaos, nor in the glassy region, where the motion of the grains is too coherent.

In the glassy phase, the v_x distribution again fits a Gaussian at low v_x but has exponential tails. In this case, the tails, that are best fit by a function $A \exp(-|v_x/v_0|)$, are closest to filling the distribution near the top of the glassy region and then settle to a fixed fraction of the distribution in bulk of the glassy region. Such distributions have also been seen in experiments of vibrated monolayers of spheres [38, 39]. Exponential tails have also been seen in several simulations of dense clusters in two dimensions [37, 40]. Such exponential tails have also been derived in the context of driven inelastic Maxwell models with diffusion [4, 6, 7, 41].

We found that our $v_y - \langle v_y \rangle$ distributions in the free-fall and glassy regions showed similar behavior to the v_x distributions described above and as shown in Figs. 3.7(a) and (c). In the fluid region, however, the v_y distribution was dramatically asymmetric about the mean. This distribution can be fit separately on the left and on the right of its peak to functions $A \exp(-(|v_x/v_0|^\alpha))$, with $\alpha = 3/2$, as shown in Fig. 3.7(b). Interestingly, this asymmetry in the v_y distribution has also been found in vibratory experiments [15]. A possible origin of this anisotropy may be

that particles going faster than the average downward velocity are more likely to collide than particles going slower than the average.

Clearly, the velocity distribution for each state has very distinct characteristics. As a result, there are transition areas where the velocity distribution changes from one type to another. These cross-over areas can give the impression of there being power-law tails in the velocity distributions. Such distributions have also been suggested theoretically as "borderline" cases [6, 7]. As an example we examine the transition area between the free-fall and the fluid regions. The velocity distribution for the fluid is wider than that in the free-fall region (cf. Fig. 3.6) and grows into the free-fall distribution from the tails. The v_x velocity distribution and v_y velocity distribution at roughly halfway through this transition area are shown for one case in Figs. 3.9(a) and 3.9(b), respectively. As can be seen, the tails of these distributions can be fit to $P \sim 1/v^\beta$ with $\beta = 3.8$ for both tails of the v_x distribution and with $\beta = 7.3$ and $\beta = 2.4$ for the left and right tails of the v_y distribution rather convincingly. Theory [6, 7, 8] suggests considerably higher exponents for the power laws. Interestingly, our exponents are very close to the experimentally determined power-law exponents of $\beta = 3.6$ for the tails of the v_x distribution and $\beta = 7.4$ and $\beta = 2.9$ for the tails of the v_y distribution found recently in an experiment by Moka and Nott [16]. Their experiment configuration is very similar to that of our simulation and the characteristics of the average velocity profile and the profile of velocity fluctuations are consistent with what we find in the free-fall to fluid transition area (compare Fig. 1 of [16] with the appropriate profiles in our Figs. 3.3 and 3.5). It is not clear that this is a true power law as it corresponds to a cross-over area and while we have just over three decades in height, we do not have a full decade in width. However, it is possible that the equivalent area in the experiment is wider than we see in our simulations due to some aspect that we are not including (such as particle spin). It would be interesting to see the experimental results at a range of heights along
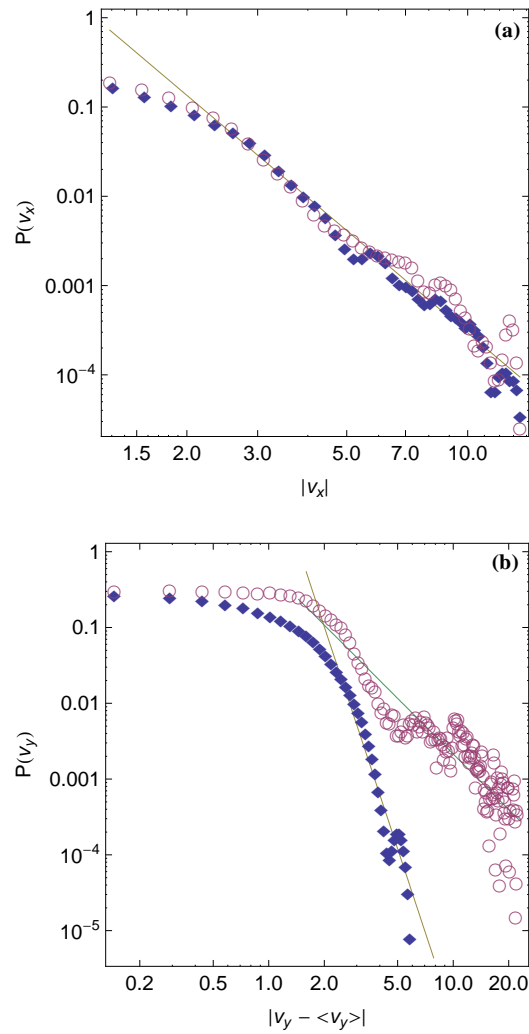
Figure 3.9: (a) Log-log plots of x-velocity distributions in a transition region between free fall and fluid. The line is a power law fit $P \sim 1/v^\beta$ with $\beta = 3.8$. (b) y-velocity distributions in a transition region between free fall and fluid. The line is a power law fit $P \sim 1/v^\beta$ with $\beta = 7.3$ on the left and $\beta = 2.4$ on the right.

the column to compare with what we have done here in the simulations.

3.5   Velocity Correlations

As the particles undergo collisions traveling down the chute, they lose some of their relative velocity v_n, and hence become more correlated. In order to compare how the particles become correlated within the chute, we measured their v_x velocity-velocity correlation function every $5a$ from the top to bottom of the chute. In particular, we compared the velocity correlations of the particles in the glassy and fluid regions and found a noticeable difference in the way the velocity correlations scale.

We ran simulations with different system widths L_x, in the x direction, while keeping the dimensions in the y direction and z direction the same. Note that as the walls are at $x = 0$ and $x = L_x$, $\langle v_x \rangle = 0$. Based on our data for system widths of $20a$, $28a$, $36a$ and $44a$, the $\langle v_x(x_o)v_x(x) \rangle$ velocity correlations,

$$C(x) = \frac{\langle v_x \left(x \right) v_x \left(x_0 \right) \rangle}{\left[\langle v_x^2 \left(x \right) v_x^2 \left(x_0 \right) \rangle \right]^{1/2}}, \tag{3.4}$$

for various system sizes are shown in Fig. 3.10. The form of the tails of the velocity correlations in the glassy region follow an exponential decay, $\exp\{-(x - x_0)/\xi\}$. This is demonstrated by the straight portions of the curves in the semi-log plot shown in Fig. 3.10(a). Remarkably ξ scales only with system size, $\xi = 0.125L_x$. [The lines in Fig. 3.10(a) are parallel and the $x-$axis is already scaled by L_x.] The slope of the gray line in Figure 3.10(a) corresponds to $\xi = 0.125L_x$.

We also tried looking at 2D correlation functions $\langle v_x(x_o, y_o)v_x(x, y) \rangle$. The correlation length was similar in the y-direction, although the data for the 2D correlation function was much noisier [as it was measured relative to a single point (x_0, y_0, z_0)
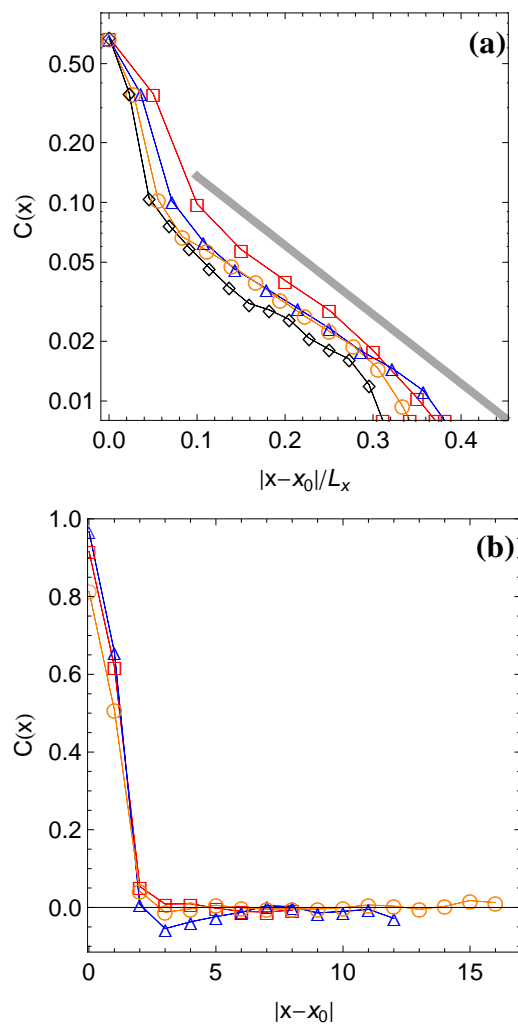
Figure 3.10: Correlation function $C(x)$ for the x component of the velocity measured from $x_0 = L_x/2$ (center of the chute). The sizes of all the systems are $L_x \times 32a \times 400a$, where L_x is the width of the system in the x direction ($L_x = 20a$ for the boxes, $28a$ for the triangles, $36a$ for the circles and $44a$ for the diamonds). (a) Semi-logarithmic plot of $C(x)$ for the x component of velocity in the glassy region as a function of the scaled variable $(x - x_0)/L_x$. Data shown in plot (a) is averaged in height in the uniform glassy region at $y_0 = 90a \pm 20a$. The gray line has a slope of -8 which translates to a length scale $\xi \approx 0.125 L_x$ in the relation $\exp\{-(x - x_0)/\xi\}$. (b) $C(x)$ in the fluid region as a function of $|x - x_0|$. The data shown in plot (b) is at a height in the fluid region of the three systems all at the same granular temperature.

and so could not benefit by the averaging over different y_0 that was done for the 1D correlation functions]. As the weight of the glassy column is supported by the walls, essentially through what is expected to be an arching effect [28], the similarity of correlation lengths in the x and y directions is expected.

Interestingly, in the fluid region, the $\langle v_x(x_o)v_x(x)\rangle$ velocity correlations drop to zero at a length of around $3-5a$, where a is the mean particle radius. This is shown in Fig. 3.10(b) which plots the velocity correlations in the fluid region for three different sized systems, but at the same granular temperature. Thus we can clearly see that how the correlations scale also distinguishes between a glassy and fluid phase in granular matter. It would be interesting if experiments could measure velocity correlations in different phases of granular matter to compare with our findings.

3.6   Properties related to velocity fluctuations

Previous work has suggested a possible relationship between the velocity fluctuations, $\delta v \equiv |\delta \mathbf{v}^2|^{1/2}$, and the flow velocity, $\mathbf{v}$. In [19] we used our simulations to confirm Menon and Durian's diffusing wave spectroscopy experimental result [13] that the fluctuating velocity is power-law related to the flow speed v_y of particles falling under the influence of gravity in a vertical chute, $\delta v \propto v^{2/3}$ (Fig. 3.11). An important detail is that we arrived at this 2/3 power law only after we had averaged our data across the x direction of the chute (in the glassy region). This is similar to the experiment, where diffusing wave spectroscopy was used. Such an experiment involves looking at the correlation of laser speckle patterns after the laser beam has traversed the width of the chute. Note, however, from Fig. 3.5(c) that the velocity fluctuations are *not* constant across the channel. Plotting δv locally (i.e., the profile across the chute rather than the average), we get the
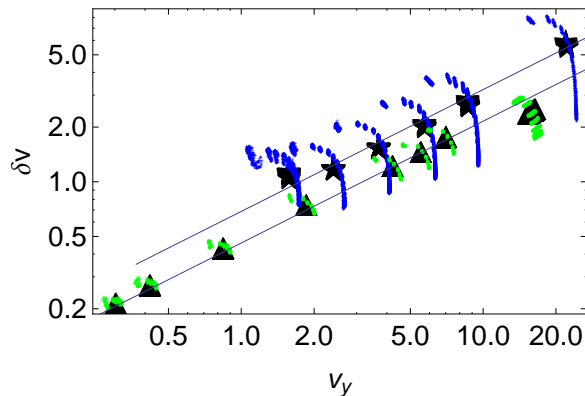
Figure 3.11: Relationship between fluctuating and flow velocity in the glassy region. Data was averaged in directions normal to $\vec{g}$ for the 32x32 ($\star$, $\delta v = \left(\delta v_x^2 + \delta v_y^2 + \delta v_z^2\right)^{1/2}$) and 16x16 ($\blacktriangle$, $\delta v = \delta v_y$) 15% polydisperse systems. The fitted lines have slope of 2/3, in agreement with the experiments of [13]. The points arcing across the line are non-averaged values of velocities and velocity fluctuations at specific local points in the system.

curved branches in Fig. 3.11. Note that the actual profiles cross the average perpendicular to our 2/3 power-law line. Thus this power law is a nonlocal, averaged effect.

In our previous paper [19] (Chapter 2) we studied collision time distributions in the glassy and fluid regions. Here we will examine how the collision time distribution changes from one region to the other and how the collision times are related to the velocity fluctuations. The average collision time (the time between successive collisions for a particle) is:

$$\tau_c \equiv \langle \tau \rangle = \frac{\int_{t_s}^{t_b} \tau N(\tau) d\tau}{\int_{t_s}^{t_b} N(\tau) d\tau}, \tag{3.5}$$

where $N(\tau)$ is the histogram of collision times observed in one of our simulations, and t_s and t_b are upper and lower cutoffs. Figure 3.12 shows the collision distributions for different regions of our simulations. For the analytic form of the
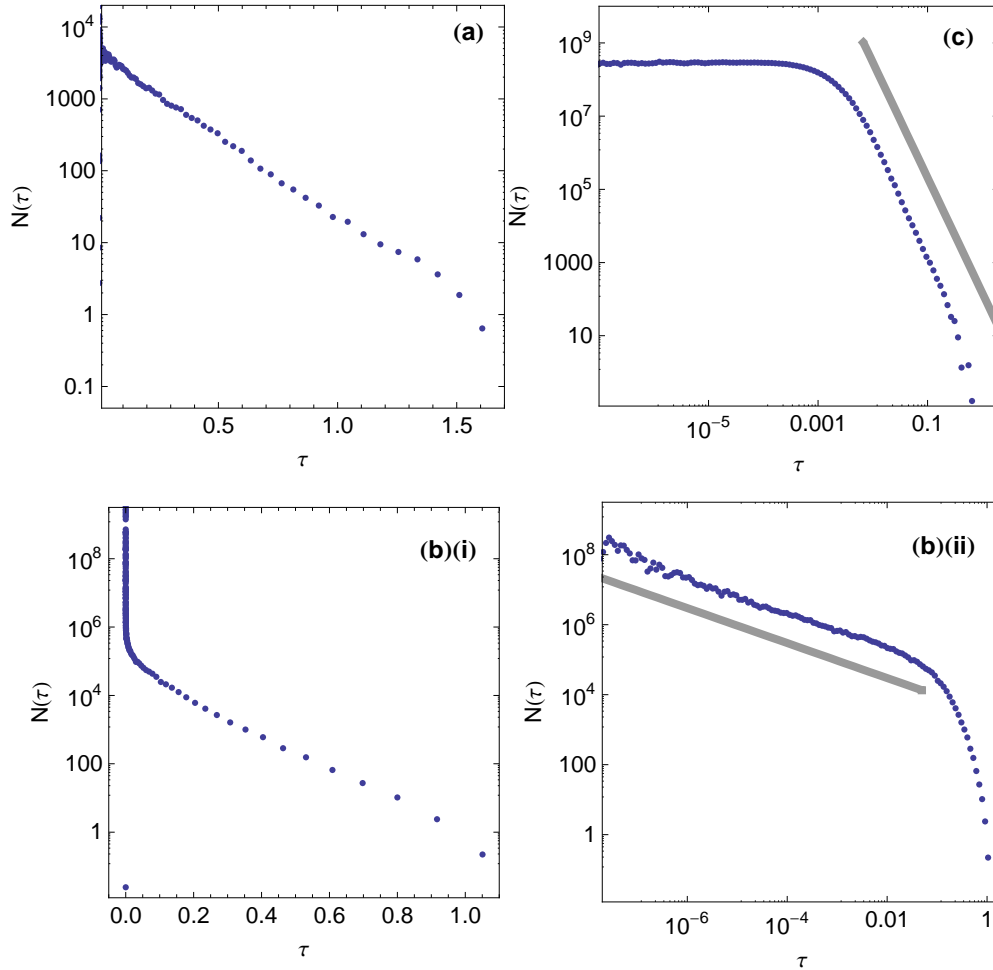
Figure 3.12: In a 15% polydisperse 3D 32x32x250 simulation with a probability of reflection p of 10% at the bottom of the chute, (a) semilogarithmic plot of collision time distribution at top of fluid region at $h = 190$, (b)(i) semilogarithmic plot on the left and (b)(ii) log-log plot on the right of the collision time distribution in fluid-glass transition region at $h = 165$ (the sloped straight line in the log-log plot on the right has a slope of -0.5), and (c) log-log plot of collision time distribution in glassy region at $h = 90$ (the sloped straight line has a slope of -3).
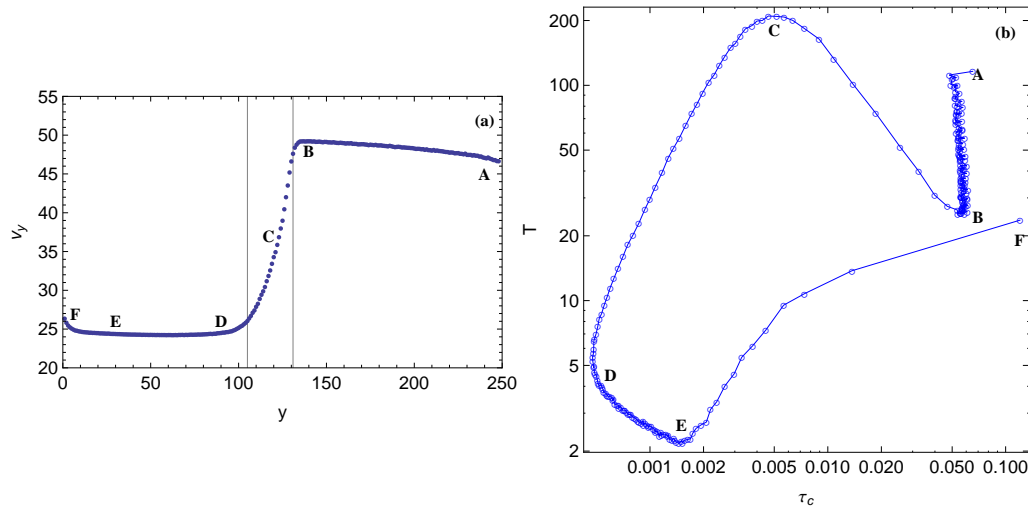
Figure 3.13: Mapping of points A, B, C, D, E and F between (a) v_y velocity profile along chute height y and (b) log-log plot of velocity fluctuations as measured by the granular temperature, T, versus mean collision time, τ_c in a 15% 3d 32x32x250 simulation with $p = 0.01$. The free-fall region runs between points A and B. The free-fall to fluid transition region runs between points B and C. The fluid region runs between points C and D. The glassy region runs between points D and E. Between points E and F the the material becomes fluid again near the bottom sieve. Here, p is the probability of reflection at the bottom of the chute and the asymptotic coefficient of restitution $\mu_0 = 0.9$.

collision time distributions that we will compare our simulation data to,

$$
\langle \tau \rangle \;=\;
\begin{cases}
t_m & \text{for} \quad N(\tau) \sim e^{-\tau/t_m}, \\
2t_s & \text{for} \quad N(\tau) \sim \tau^{-3}, \; t_b \to \infty, \\
\frac{1}{3}t_b & \text{for} \quad N(\tau) \sim \tau^{-1/2}, \; t_s \to 0.
\end{cases}
\tag{3.6}
$$

Thus, the mean collision time tends to zero, or the lower cutoff, for the τ^{-3} case whereas it tends to the upper cutoff for the $\tau^{-1/2}$ case.

As can be seen from Fig. 3.12, in the fluid region we have an exponential distribution of collision times and therefore a well-defined mean collision time, $\langle \tau \rangle$, t_m from Eq. (3.6). As shown in Fig. 3.12(c), in the glass, $N(\tau) \sim \tau^{-3}$ as reported in our recent paper [19]. This is shown in Fig. 3.12(c) for one of the faster

systems. In the glass, $\langle \tau \rangle$ is essentially equal to the lower cutoff of the power law (see Eq. 3.6). In the fluid-glass transition region $N(\tau) \sim \tau^{-1/2}$ as shown in Fig. 3.12(b). In this case $\langle \tau \rangle$ is at the upper cutoff, Eq. (3.6), corresponding to the crossover to the exponential tail. The $\tau^{-1/2}$ power-law exists only over a narrow band of heights and disappears by the exponential tail continuously turning into the τ^{-3} glass distribution. The crossover between the resulting two power laws (t_b for $\tau^{-1/2}$ and t_s for τ^{-3}) moves lower as one goes into the glass. The existence of the $\tau^{-1/2}$ power-law is somewhat curious as it does not correspond to either the fluid or glassy states. However the way it disappears as we go into the glass provides a clue. If one associates the glass with a "collapsing condensate" [1, 2, 4], the fluid to glass transition should involve "droplets" of collapsing condensate coming out of the fluid. In each droplet, the collision times should be distributed as in the glass, but the cutoff, t_s will depend on how close the droplet is to the close-packed glass density. Droplets of different sizes are then likely to have different cutoffs. A wide distribution of droplet sizes will then result in a wide distribution of cutoffs for the $N(\tau) \sim \tau^{-3}$ power law, perhaps generating the $\tau^{-1/2}$ low end tail seen in the transition regime.

We now examine the relationship between the velocity fluctuations, as measured by the granular temperature $T = \left(\langle v_x^2 \rangle + \langle v_y - \langle v_y \rangle^2 \rangle + \langle v_z^2 \rangle \right) / 2$ and the collision times. Figure 3.13(a) shows the velocity profile for a very fast flowing system (with probability of reflection at the bottom of the chute of $p = 0.01$). The transitions between different phases are marked by capital letters. We can map these labeled points that mark the boundaries between the different regions onto a plot of T vs. τ_c shown in Fig. 3.13(b). The different regions show *very* different relationships between T and τ_c. To see if these relationships are general, or system specific, we look at several systems with different probabilities of reflection at the bottom of the chute, and hence very different flow rates. By plotting the different systems on the same log-log plot, as shown in Fig. 3.14, we can observe whether
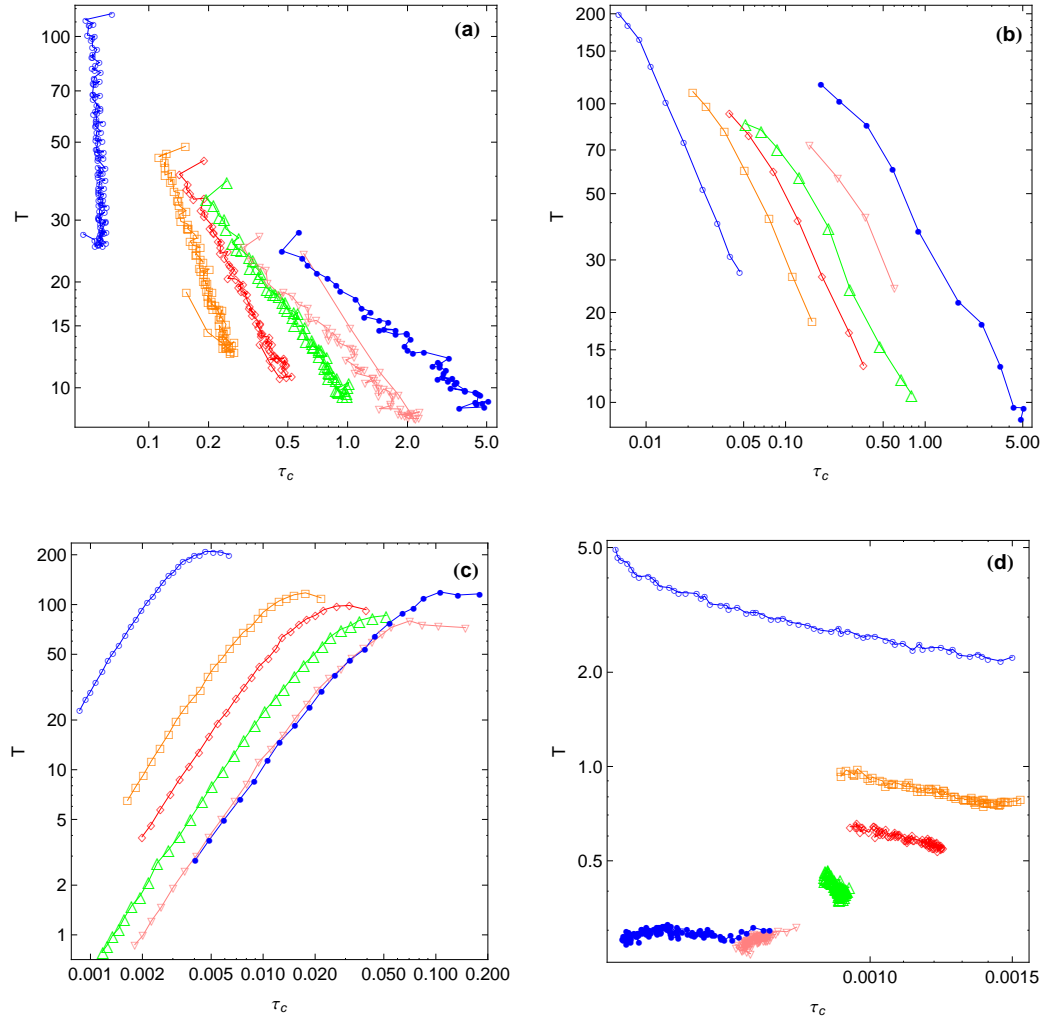
Figure 3.14: Log-log plot of velocity fluctuations as measured by the granular temperature, T, versus mean collision time, τ_c in (a) free-fall region, (b) free-fall to fluid transition, (c) fluid region and (d) glassy region in a 15% 3D 32x32x250 simulation with ($\circ$ with $p = 0.01$), ($\square$ with $p = 0.1$), ($\diamond$ with $p = 0.25$), ($\triangle$ with $p = 0.5$), ($\triangledown$ with $p = 0.75$) and ($\bullet$ with $p = 0.9$). Here, p is the probability of reflection at the bottom of the chute and the asymptotic coefficient of restitution $\mu_0 = 0.9$.
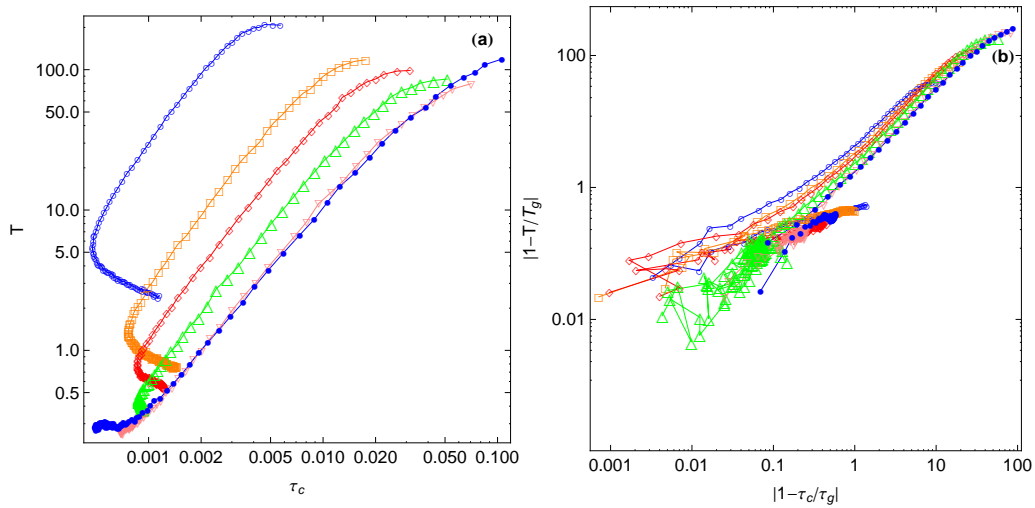
Figure 3.15: (a) Granular temperature, T, versus mean collision time, τ_c, and (b) temperature versus mean collision time scaled by the glass transition temperature, T_g and the corresponding collision time τ_g in a 15% 3D $32 \times 32 \times 250$ simulation with ($\circ$ with $p = 0.01$), ($\square$ with $p = 0.1$), ($\diamond$ with $p = 0.25$), ($\triangle$ with $p = 0.5$), ($\bigtriangledown$ with $p = 0.75$) and ($\bullet$ with $p = 0.9$). Here, p is the probability of reflection at the bottom of the chute and the asymptotic coefficient of restitution $\mu_0 = 0.9$.

there is a power-law relationship between T and τ_c in each of the different regions. As can be seen from the Figure there exists a power-law relationship $T = \tau_c^\gamma$ in the free-fall to fluid transition with γ around -1.1 (the lines are all parallel and have slope -1.1) and in the fluid region with γ around 1.4, but there is no obvious relationship in the free-fall and glassy regions.

In Fig. 3.15 we examine the fluid and glass regions corresponding to different values for the probability of reflection at the bottom of the chute, p [42]. As shown in Fig. 3.15, the faster systems with lower reflection probabilities of p such as 10% tend to *turn around* at the fluid to glass transition and reach a limiting line. The slower systems with higher reflection probabilities such as 75% both fall on the same limiting line. This behavior can be explained as follows. The simulation with $p = 10\%$ is a much faster flow so its y velocity, density and velocity fluctuations are not a constant value in the "glass". For example, the

density at the top of the glassy region for the fast flows is slightly lower and gradually increases as one goes further into the glass. Thus the system is unable to reach a stationary, or in other words translationally invariant, steady state.

It is also worthwhile to consider the fluid to glass transition regions in terms of the jamming phase diagram proposed by [43]. They propose a "jammed" phase diagram as a function of temperature, density, and shear stress where the region in the vicinity of the origin is jammed and the region far from the origin is not jammed. Their jamming transition is expected to be first order except for the J-point, a transition at close packing density and at $T = 0$ and where the shear stress is zero. The transitions for the different systems seen in Fig. 3.15 occur at different temperatures and different shear stresses (related to the flow speed controlled by the probability of reflection p). As we lower the flow speed, and the temperature at which the transition occurs decreases, our system should be approaching the J-point and the transition should become more continuous and the "glass" state should approach a more well-defined translationally invariant, disordered limit. This is consistent with what we observe in Fig. 3.15. If we attempt to scale Fig. 3.15(a) by the difference in temperature from the observed transition for each system, we arrive at Fig. 3.15(b). We find that the slower systems start to approach a single universal line but the faster systems deviate. While a full investigation of the transition is beyond the scope of the current paper, we plan to investigate this phenomenon in the future.

3.7   Conclusions

In this paper we have examined velocity fluctuations in computer simulations of a granular system. The gravity driven granular chute flow system we study has been realized in numerous experiments. Our observations are consistent with

the fluctuations observed in the experiments most closely matching our simulations [13, 16].

We find three main classes of velocity distributions corresponding to the free-fall, fluid, and glassy regions. In the free-fall region we see a Gaussian distribution of velocities, but the velocity fluctuations in the vertical and horizontal direction evolve separately. In the fluid region the velocity distribution has a stretched exponential tail of $\exp\left(-v^{3/2}\right)$, but the vertical velocity fluctuations become very asymmetric and require separate fits for velocities above and below the mean. In the glassy state the velocity distribution has exponential tails. Velocity fluctuations are correlated on the scale of the system size in the glassy region and have a finite correlation length independent of system size in the fluid region.

We then related the velocity fluctuations to the collision time, the time between collisions. The distribution of collision times in the glass is power-law distributed and in the fluid it is exponential, as we observed in previous work [19] (Chapter 2). We also find evidence that the transition from fluid to glass becomes more continuous for slower-moving, lower temperature flows. The slower flows also reach a more translationally invariant disordered glassy state. These observations are consistent with the approach to the J-point defined by O'Hern et al. [43].

3.8   Acknowledgments

REFERENCES

[1] I. Goldhirsch and G. Zanetti, Phys. Rev. Lett. **70**, 1619 (1993).

[2] S. McNamara and W. R. Young, Phys. Rev. E **50**, R28 (1994).

[3] I. S. Aranson and L. S. Tsimring, Rev. Mod. Phys. **78**, 641 (2006).

[4] S. Esipov and T. Poschel, J. Stat. Phys. **86**, 1385 (1997).

[5] T. P. C. van Noije, M. H. Ernst, R. Brito, and J. A. G. Orza, Phys. Rev. Lett. **79**, 411 (1997).

[6] M. H. Ernst and R. Brito, Phys. Rev. E. **65**, 040301 (2002).

[7] M. H. Ernst and R. Brito, J. Stat. Phys. **109**, 407 (2002).

[8] E. Ben-Naim and J. Machta, Phys. Rev. Lett. **94**, 138001 (2005).

[9] V. V. R. Natarajan, M. L. Hunt, and E. D. Taylor, J. Fluid Mech. **304**, 1 (1995).

[10] R. M. Nedderman and C. Laohakul, Powder Technol. **25**, 91 (1980).

[11] H. Takahashi and H. Yanai, Powder Technol. **7**, 205 (1973).

[12] S. B. Savage, J. Fluid Mech. **92**, 53 (1979).

[13] N. Menon and D. J. Durian, Science **275**, 1920 (1997).

[14] W. Losert, D. G. W. Cooper, J. Delour, A. Kudrolli, and J. P. Gollub, Chaos **9**, 682 (1999).

[15] F. Rouyer and N. Menon, Phys. Rev. Lett. **85**, 3676 (2000).

[16] S. Moka and P. R. Nott, Phys. Rev. Lett. **95**, 068003 (2005).

[17] W. Losert, L. Bocquet, T. C. Lubensky, and J. P. Gollub, Phys. Rev. Lett. **85**, 1428 (2000).

[18] L. Bocquet, W. Losert, D. Schalk, T. C. Lubensky, and J. P. Gollub, Phys. Rev. E **65**, 011307 (2001).

[19] J. J. Drozd and C. Denniston, Europhys. Lett. **76**, 360 (2006).

[20] We use units where the acceleration due to gravity $g = 1$, the mean grain radius $a = 1$, and the mean grain mass $m = 1$. To convert to units where, say, g = 9.8 m/s^2, a = 1.5mm = 1.5×10^{-3} m, and m = 0.11 grams = 1.1×10^{-3} kg (i.e., a steel ball with mass density of 7850 kg/m^3), multiply our distance by a in meters, time by $(a/g)^{1/2} = [(1.5 \times 10^{-3}$ m$)/(9.8$m/s$^2)]^{1/2} = 0.0124$ s and masses by m in kilograms. A typical simulation run is $10^4 - 10^5$ time units, or $2 - 20$ minutes of real time for a system made up of steel balls 3 mm in diameter. For a typical run with polydisperse grains, this corresponds to 6.5×10^9 collisions.

[21] C. Denniston and H. Li, Phys. Rev. E **59**, 3289 (1999).

[22] J. T. Jenkins and S. B. Savage, J. Fluid Mech. **130**, 187 (1983).

[23] S. B. Savage and D. J. Jeffrey, J. Fluid Mech. **110**, 255 (1981).

[24] C. Bizon, M. D. Shattuck, J. B. Swift, W. D. McCormick, and H. L. Swinney, Phys. Rev. Lett. **80**, 57 (1998).

[25] S. Luding, E. Clement, J. Rajchenbach, and J. Duran, Europhys. Lett. **36**, 247 (1996).

[26] W. Goldsmith, *Impact: The theory and physical behaviour of colliding solids* (E. Arnold, London, 1960), 263-267.

[27] Typical fluctuation velocities are $\delta v = 0.05$ implying $\mu \approx 0.99$.

[28] K. To, P. Y. Lai, and H. K. Pak, Phys. Rev. Lett. **86**, 71 (2001).

[29] J. Duran, *Sands, powders, and grains :an introduction to the physics of granular materials*, Partially ordered systems. (Springer, New York, 2000), ISBN 0387986561.

[30] L. D. Landau and E. M. Lifshitz, *Fluid Mechanics*, 2nd ed., (Pergamon Press, Oxford, England; Toronto, 1987), ISBN 0080339336.

[31] H. Reiss and A. D. Hammerich, J. Phys. Chem. **90**, 6252 (1986).

[32] E. Khain, Phys. Rev. E **75**, 051310 (2007).

[33] E. Khain, B. Meerson, and P. V. Sasorov, Phys. Rev. E **70**, 051310 (2004).

[34] R. Liu, Y. Li, M. Hou, and B. Meerson, Phys. Rev. E **75**, 061304 (2007).

[35] M. Schröter, S. Nägle, C. Radin, and H. L. Swinney, Europhys. Lett. **78**, 44004 (2007).

[36] J. S. van Zon and F. C. MacKintosh, Phys. Rev. Lett. **93**, 038001 (2004).

[37] R. Cafiero, S. Luding, and H.J. Herrmann, Phys. Rev. Lett. **84**, 6014 (2000).

[38] J. S. Olafsen and J. S. Urbach, Phys. Rev. Lett. **81**, 4369 (1998).

[39] J. S. Olafsen and J. S. Urbach, Phys. Rev. E **60**, R2468 (1999).

[40] H. J. Herrmann, S. Luding, and R. Cafiero, Physica A **295**, 93 (2001).

[41] A. V. Bobylev and C. Cercignani, J. Stat. Phys. **106**, 547 (2002).

[42] In our work on collision time distributions [19] described in Chapter 2, our reflection probability p value was 90%, or in other words, our collision times were measured for a very slow flow of particles.

[43] C. S. O'Hern, L. E. Silbert, A. J. Liu, and S. R. Nagel, Phys. Rev. E **68**, 011306 (2003).

CHAPTER 4

Constitutive relations in dense granular flows

4.1   Introduction

There have been numerous attempts to accurately describe stresses in granular matter ranging from approaches using partial differential equations [1, 2, 3, 4, 5] to using phenomenological ideas [6, 7]. Apart from adopting mathematical models, if we concentrate on the basic physics of momentum conservation, mass conservation and energy conservation, this does not provide us with enough equations to fully solve for local density, velocities, and temperature. In order to solve for these quantities, the stress tensor and heat flux need to be expressed in terms of these local variables in order to "close" the equations (i.e. have the same number of equations and unknowns). This prompts us to studying various constitutive relations to provide these necessary additional constraints. With this aim in mind, we have performed simulations of gravity driven dense granular flow in three dimensions to compare and test constitutive pressure, stress and energy relations of granular matter.

The binary, hard sphere collision model used for our simulations is similar to that used in [8, 9], but for illustrative purposes a typical snapshot from one of our simulations is shown in Fig. 4.1(a). We will reiterate a brief description of
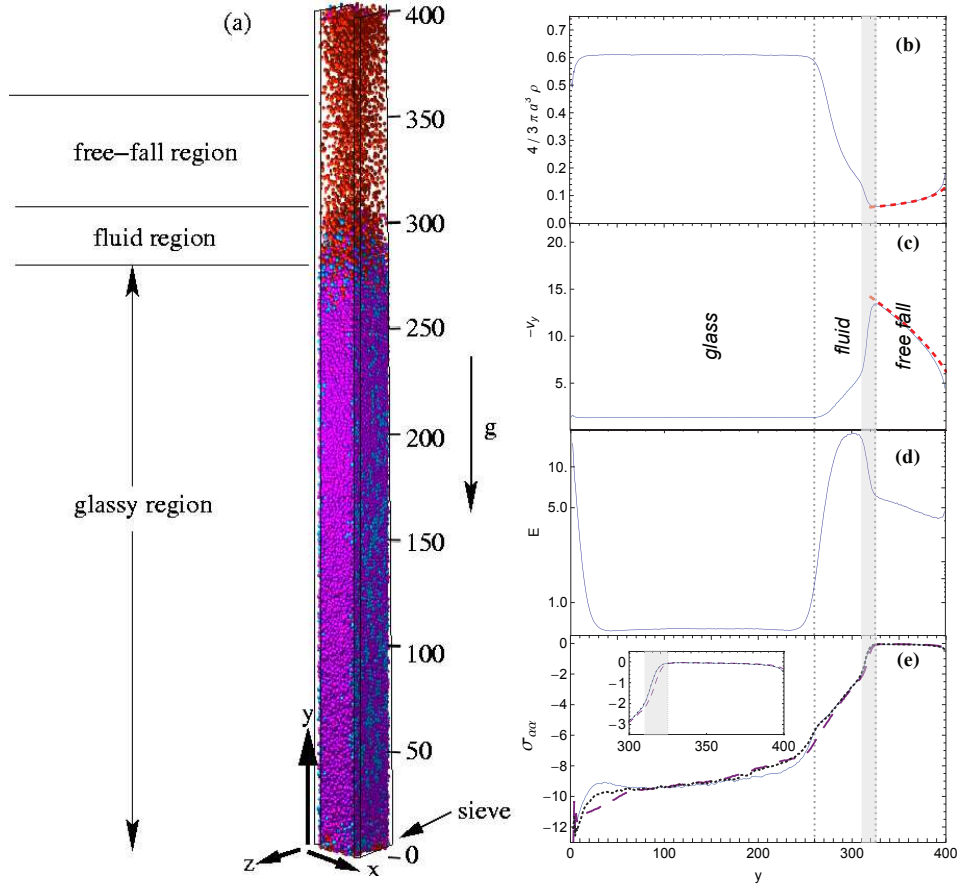
Figure 4.1: (a) Section of a simulation involving 43 200 grains with 15 % poly-dispersity. The system size is $32a \times 32a \times 400a$. There are reflective walls at $x = 0$ and $x = L_x$, periodic boundary conditions in the z-direction, and a finite probability of reflection at the bottom of the chute (at $y = 0$) with an asymptotic coefficient of restitution $\mu_0 = 0.97$. Time-averaged density (volume fraction) in (b) and $y-$ velocity in (c) down the center of a 3D chute. The short dashed lines are analytic calculations of density and v_y in the free-fall region (described in text). (d) The total kinetic energy $E = \frac{1}{2}\rho v^2 + \frac{3}{2}\rho T$ and (e) stress tensor components σ_{xx} (solid line), σ_{yy} (dashed line) and σ_{zz} (dotted line). The measurements for plots (b), (c), (d) and (e) were taken down the center of the chute.

our model in the next paragraphs but for more details one can refer to references [8, 9] (Chapters 2 and 3).

In our simulation, spherical grains are dropped in from the top of a rectangular chute and fall under the influence of gravity. There are flat walls at the left and right (x-direction) of the chute and periodic boundary conditions at the front and back (z-direction). At the bottom of the chute ($y = 0$), grains are reflected with a probability p (typically $p = 90\%$). Particles transmitted through the bottom are replaced at the top of the chute in order to maintain steady-state. Particles reflect off the walls of the chute with a partial loss, typically 10% in their vertical (y) velocity. This is essential as experiments show [10, 11] that much of the column weight is supported by the walls.

Particles in our simulation undergo binary collisions where their momenta are transferred along the line joining their centers. Specifically, the velocities after collision $\dot{\mathbf{r}}_1'$ and $\dot{\mathbf{r}}_2'$ in terms of the velocities before collision, $\dot{\mathbf{r}}_1$ and $\dot{\mathbf{r}}_2$, are

$$
\begin{pmatrix} \dot{\mathbf{r}}_1' \\ \dot{\mathbf{r}}_2' \end{pmatrix} = \begin{pmatrix} \dot{\mathbf{r}}_1 \\ \dot{\mathbf{r}}_2 \end{pmatrix} \tag{4.1}
$$
$$
+ \frac{(1 + \mu)}{(m_1 + m_2)} \begin{pmatrix} -m_2 & m_2 \\ m_1 & -m_1 \end{pmatrix} \begin{pmatrix} \dot{\mathbf{r}}_1 \cdot \mathbf{q} \\ \dot{\mathbf{r}}_2 \cdot \mathbf{q} \end{pmatrix} \mathbf{q},
$$

where $\mathbf{q} = (\mathbf{r}_2 - \mathbf{r}_1)/|\mathbf{r}_2 - \mathbf{r}_1|$, and μ is the coefficient of restitution. Such collision models of granular flow have a long history [12, 13]. μ is a velocity-dependent restitution coefficient described by the phenomenological relation [14, 15],

$$
\mu(v_n) = \begin{cases} 1 - (1 - \mu_0)(v_n/v_0)^{0.7} & , v_n \leq v_0 \\ \mu_0 & , v_n \geq v_0. \end{cases} \tag{4.2}
$$

Here v_n is the component of relative velocity along the line joining the grain centers, μ_0 is the asymptotic coefficient at large velocities, and $v_0 = \sqrt{2ga}$ [16].

Equation (4.2) effectively makes the ball collisions become more elastic as the collisions become weaker as observed experimentally [17, 18]. Scaled units are given in footnote [19].

In previous work [8, 9] (Chapters 2 and 3) we examine both mono- and poly-disperse mixtures of spheres. Here we simulate only 15% poly-disperse particles. In this context, a polydispersity of 15% means that the standard deviation of a particle radius is 0.15 if the mean is 1 using a Gaussian distribution of radii. Poly-disperse particles achieve a truly glassy state, and here we are interested in testing and comparing constitutive relations in the glassy state, in addition to the free-fall and fluid states. Mono-disperse or nearly mono-disperse particles gradually increase in order and crystallize, and it is beyond the scope of this paper to examine the approach to the crystallized state in detail, although we did touch upon such details in previous work [8, 9] (Chapters 2 and 3).

A typical steady-state configuration of our simulation is shown in Fig. 4.1(a). The steady-state density (plotted as a volume fraction), velocity, energy, and diagonal stresses from our simulation for this typical configuration were all measured down the center of the channel and are plotted in Figs. 4.1(b), (c), (d) and (e), respectively. The orientation of the x, y and z axes is shown at the bottom of the visualization in Fig. 4.1(a).

As indicated by the labels and vertical dashed lines in Figs. 4.1(b)-(e), there are three regions, which we label as a glassy region, a fluid region and a free fall region. These labels were justified in our previous work [8, 9] (Chapters 2 and 3). In the free fall region the grains accelerate at $1\,g$ and collisions do not have a significant impact on their kinetics [8, 9] (Chapters 2 and 3). In the liquid region the density is sufficiently high that collisions mix the grains, but the distribution of collision times are exponential, meaning that collisions are largely independent. In the glass region, the collision time distribution is a power-law and thus collisions are

not independent and as a result there are collisions at a wide range of time scales [9] (Chapter 3).

It is important to note that the relative sizes of the glassy, fluid and free-fall regions vary depending on the coefficient of restitution used. As expected, the lowest asymptotic coefficient of restitution of 0.9 resulted in the smallest fluid region, an intermediate asymptotic coefficient of restitution of 0.95 resulted in a larger fluid region, and the largest asymptotic coefficient of restitution of 0.99 resulted in the largest fluid region for the same sized column. The existence of transition regions between the free-fall, fluid and glassy states was demonstrated in previous work [8, 9] (Chapters 2 and 3). The transition region between the free-fall region and the fluid region is indicated by the vertical gray shaded stripe in Figs. 4.1(b-e). Unless otherwise noted, the results presented in this paper use an asymptotic coefficient of restitution of 0.97, which facilitates the study of one of the wider transition regions. A wider fluid region clearly shows a kink in the free-fall to fluid transition region in the data profiles as shown in Figs. 4.1(b)-(e). It is interesting to note that the kink at this transition in the density and velocity profiles lines up with the peak in the kinetic energy and inflection point in the stress profiles as shown in Figs. 4.1 (d) and (e). This peak marks the boundary between the fluid region and the free-fall to fluid transition region.

4.2 Continuum Equations

Our simulation evolves over discrete binary collisions. In our simulation, we average various physical properties based on these discrete events over time and space. We resolve our $32a \times 32a \times 400a$ chute over a fine volume grid composed of $1a \times 1a \times 1a$ cubes. This resolution was chosen to scale with the size of the particles of mean radii $a = 1$. This allows us to map our discrete system onto

a time-averaged continuum set of fields. We will now begin by describing the continuum equations describing the average density, $\langle \rho \rangle$, velocity $\langle \vec{v} \rangle$ and energy $\langle E \rangle$ that we would expect our system to map onto. To simplify the notation, even though the measured properties in our simulation are quantities averaged in time and over the translationally invariant z-direction, we omit the angled brackets $\langle \cdot \rangle$ in the conservation equations that follow.

4.2.1 Conservation equations

In this section, we will describe the continuum equations of conservation of mass, momentum and energy that we will attempt to map our simulation results onto. We will describe how the physical terms in these equations can be measured directly from our simulation.

The continuity equation for mass gives us one equation

$$\frac{\partial \rho}{\partial t} + \nabla \cdot (\rho \mathbf{v}) = 0. \tag{4.3}$$

Momentum conservation requires that

$$\partial_t (\rho v_\alpha) + \partial_\beta (\rho v_\alpha v_\beta) = \partial_\beta \sigma_{\alpha\beta} + \rho g_\alpha, \tag{4.4}$$

where $\sigma_{\alpha\beta}$ is the stress tensor, and all v_α and v_β refer to first moments of the velocity distribution. This gives us the three components of the Navier-Stokes equations. The Einstein summation convention is used for repeated indices α and β. The indices α and β refer to the x, y or z components.

The time averaged stress tensor can be directly measured in our simulation using

the microscopic form of the 3D stress tensor [20]:

$$\sigma_{\alpha\beta} = \sigma_{\alpha\beta}^{\textbf{kinetic}} + \sigma_{\alpha\beta}^{\textbf{collision}} \tag{4.5a}$$

$$= -\langle \rho \left(v_\alpha - \langle v_\alpha \rangle \right) \left(v_\beta - \langle v_\beta \rangle \right) \rangle \tag{4.5b}$$

$$+ \frac{1}{t} \sum_{collisions} -\frac{1}{2}(1 + \mu)(\dot{\mathbf{r}}_{1} - \dot{\mathbf{r}}_{2}) \cdot \hat{\mathbf{q}} \left(\hat{\mathbf{q}} \cdot \hat{\mathbf{e}}_\alpha \right) \left(\hat{\mathbf{q}} \cdot \hat{\mathbf{e}}_\beta \right),$$

where $\hat{\mathbf{e}}_\alpha$ and $\hat{\mathbf{e}}_\beta$ are $\hat{\mathbf{x}}$, $\hat{\mathbf{y}}$ or $\hat{\mathbf{z}}$. The $\frac{1}{2}$ accounts for the double counting of collisions in the sum (we count the transfer from particle 1 to 2 and the transfer from 2 to 1).

Our fifth equation is an equation describing the energy conservation in our system

$$\partial_t \left(E \right) + \partial_\alpha \left(v_\alpha E + F_\alpha \right) = I + \rho g \cdot \mathbf{v}, \tag{4.6}$$

where the Einstein summation convention is used for repeated indices. Briefly,

$$E = \frac{1}{2}\rho v^2 + \frac{3}{2}\rho T \tag{4.7}$$

is the (kinetic) energy (note that $v^2 = \langle v \rangle^2$ in the first term), where

$$T = \frac{1}{3}\delta v^2 = \left(\langle v_x^2 \rangle + \langle v_y - \langle v_y \rangle^2 \rangle + \langle v_z^2 \rangle \right) /3 \tag{4.8}$$

is the granular temperature. The energy, E, from our simulation is plotted in Fig. 4.1(d). $\mathbf{F}$ is the non-convective energy flux and α refers to the x, y or z component.

An important component of the non-convective energy flux $\mathbf{F}$, is the collision energy flux, $\mathbf{F_c}$. Part of the energy flux is related to the coherent transfer of momentum, that is, the work done by the stress tensor and the other part is the heat flux. We can measure the energy transfered between grains in a collision

using Eq. (4.1)[20] to get

$$\delta \mathbf{F_c} = \frac{1 + \mu}{m_1 + m_2} \left[m_1 \left(\dot{\mathbf{r}}_1 \cdot \mathbf{q} \right)^2 - m_2 \left(\dot{\mathbf{r}}_2 \cdot \mathbf{q} \right)^2 \right] \mathbf{q}. \tag{4.9}$$

Averaging over time gives the collision energy flux as

$$\mathbf{F_c} = \frac{1}{t} \sum_{collisions} \delta \mathbf{F_c}. \tag{4.10}$$

Similarly, we can easily use Eq. (4.1) to calculate the dissipation, I from the kinetic energy lost in each collision,

$$\delta I = -\frac{1 - \mu^2}{2(m_1 + m_2)} \left(m_1 \dot{\mathbf{r}}_1 \cdot \mathbf{q} - m_2 \dot{\mathbf{r}}_2 \cdot \mathbf{q} \right)^2. \tag{4.11}$$

If we average δI over the collisions that occur in a small cell $(1 \times 1 \times L_z)$ of our simulation, and if we also average δI per unit time (effectively multiplying by the collision frequency f_c), we arrive at the average dissipation rate I which is the remaining term in Eq. (4.6).

Equations (4.3), (4.4) and (4.6) give us five equations (in the static limit), but there are six unknown stress values, namely the diagonal stresses σ_{xx}, σ_{yy}, σ_{zz}, and, using the fact that the stress tensor is symmetric, we have the shear stresses $\sigma_{xy} = \sigma_{yx}$, $\sigma_{xz} = \sigma_{zx}$ and $\sigma_{yz} = \sigma_{zy}$. We need six constitutive equations to solve for these six unknown stress values. Similarly, all the terms in Eq. (4.6) can be measured directly from a simulation, however they cannot be predicted ahead of time without relating the $\mathbf{F}$ and I to the density, velocities, or energy by means of two additional constitutive relations. The dissipation and heat flux will be examined in more detail in sections 4.2.5 and 4.2.7.

4.2.2   Stress and energy balance

In the previous section we described the conservation equations that are applicable to our system. In the upcoming sections we will examine these conservation equations in detail applying them to the different regions of our simulation. In this section we will examine the balance of stress and energy in the fluid, glass and free-fall regions. In particular, we will examine Eq. (4.4) in the different regions of our simulation. The stress tensor cannot be ignored in these regions, even as a first approximation. If we assume in Eq. (4.4), that the time derivative is zero as we are in steady state, and if we assume that the kinetic terms, $\partial_\beta \left(\rho v_\alpha v_\beta \right)$ are negligible (as is observed by the low acceleration values in the glassy and in part of the fluid region in Fig. 2(c) in reference [8] and in Fig. 1(d) in reference [9]) (Fig. 3.2(c) in Chapter 3 and Fig. 2.1(d) in Chapter 2), we arrive at

$$\partial_x \sigma_{yx} + \partial_y \sigma_{yy} = -\rho g_y, \tag{4.12}$$

where $g_y = -g < 0$ in this orientation.

Figures 4.2(a) and (b) show the balance of the weight, $-\rho g$ and stress gradients $\partial_x \sigma_{yx} + \partial_y \sigma_{yy}$ in the fluid and glassy regions, respectively. There are *very* significant differences between how these terms are balanced in the liquid and glassy regions. We find that the pressure gradient $\partial_y \sigma_{yy}$ is the dominant term supporting the weight in the fluid region. This is consistent with what one would expect in a simple fluid where the pressure would be a function of depth, $P = \rho g y + constant$. In contrast, in the glassy region we find that the gradient in the shear stress, $\partial_x \sigma_{yx}$ is the dominant term supporting the weight. Here, as in our previous paper [9], we can conclude that in the glassy region the system supports a finite shear stress and this region behaves like a solid in this sense.

As a result, a constitutive relation for the pressure is critical to understanding
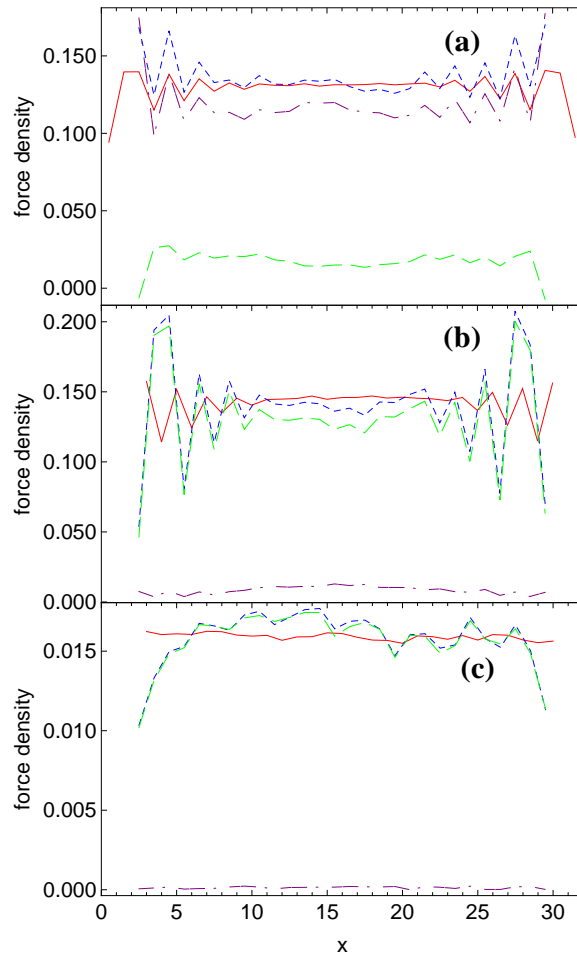
Figure 4.2: Plot of force densities $\partial_y\sigma_{yy}$ (dot-dashed line), $\partial_x\sigma_{yx}$ (long dashed line), $\partial_x\sigma_{yx} + \partial_y\sigma_{yy}$ (short dashed line) and the weight $-\rho g_y$ (solid line) in (a) the fluid region and (b) the glassy region versus the width x for a 400-height column using an asymptotic coefficient of restitution μ_0 of 0.97 and probability of reflection $p = 90\%$. (c) Plot of force densities $\partial_y\sigma_{yy}$ (dot-dashed line), $-\partial_y\rho v_y^2$ (long dashed line), $\partial_x\sigma_{yy} - \partial_y\rho v_y^2$ (short dashed line) and the weight $-\rho g_y$ (solid line) in the free-fall region.

the fluid region while a constitutive relation for the shear stress is necessary for describing the glass.

Now that we have looked at the stress balance in the fluid and glassy regions, we can next examine the balance in the free-fall region. Taking the y component of the Navier-Stokes Eq. (4.4), we have

$$\partial_y \left(\rho v_y^2 \right) = \partial_y \sigma_{yy} + \rho g_y, \tag{4.13}$$

where $g_y = -g < 0$ in this orientation. Figure 4.2(c) shows the balance of the weight, ρg and stress gradients $\partial_y \sigma_{yy} - \partial_y \left(\rho v_y^2 \right)$. In the free-fall region the pressure gradient, $\partial_y \sigma_{yy} \approx 0$, and the kinetic term, $-\partial_y \left(\rho v_y^2 \right)$, contributes solely to balance the weight, ρg.

Finally, we can observe the energy balance Eq. (4.6) in all three regions. We can assume that the time derivatives are negligible since we are in steady state and that the derivatives in the periodic z direction are also negligible. Note that the only significant energy fluxes are in the x and y directions and $\delta v_x^2 \approx \delta v_y^2 \approx \delta v_z^2$ and thus we can say that $T \approx \delta v_y^2$. Using these assumptions together with Eq. (4.6), we finally arrive at the energy equation

$$\nabla \cdot \mathbf{F} = I + \rho g v_y, \tag{4.14}$$

where we have used the following constitutive relation for the energy flux

$$\mathbf{F} = \mathbf{F_c} - \frac{1}{2} \langle \rho \left(v_\alpha - \langle v_\alpha \rangle \right) \left(v_\beta - \langle v_\beta \rangle \right) \rangle v_\beta \tag{4.15}$$

The left and right sides of Eq. (4.14), as directly measured from our simulation, are plotted in Fig. 4.3. The clear agreement in the free fall, fluid and glass regions shows that all the assumptions made to this point are reasonable.
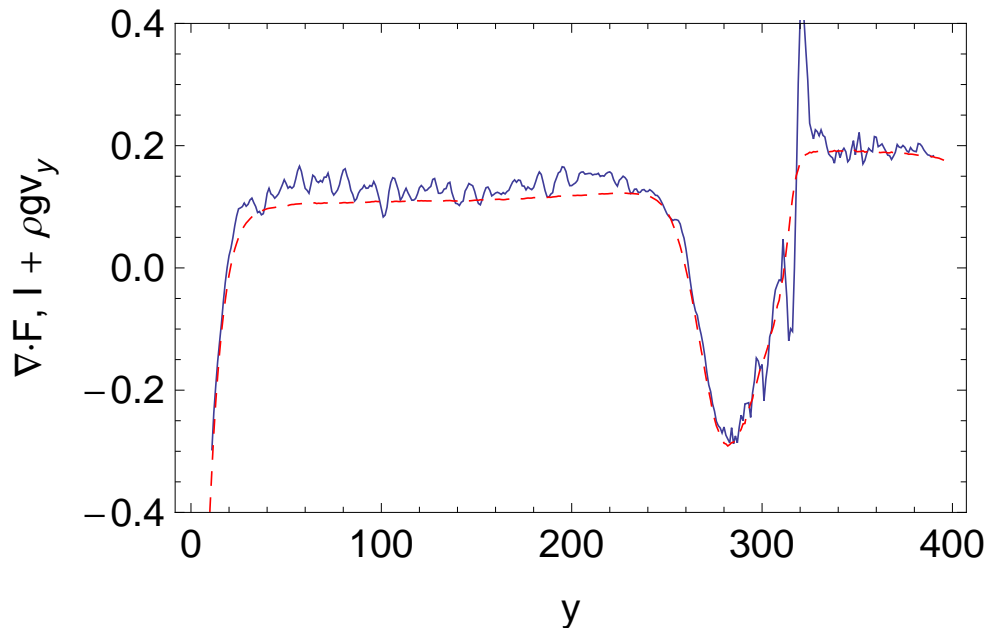
Figure 4.3: (a) Plot of the components of the energy equation from Eq. (4.14) in the free-fall region. The solid line is the left side of the equation, $\nabla \cdot \mathbf{F}$, and the dashed line is the right side of the equation, $I + \rho g v_y$.

4.2.3 Pressure

In our discussion of stress balance in the previous section, we demonstrated the role of the pressure gradient in balancing the weight, particularly in the fluid and somewhat less importantly in the glass. In this section, we will examine several equations of state for pressure for the glassy and fluid regions of our system. In a simple fluid the pressure is normally defined as

$$P = -\frac{1}{3} Tr\left(\sigma\right), \tag{4.16}$$

and the diagonal stresses $\sigma_{\alpha\alpha} = -P$. However, as is already clear from Fig. 4.1(e) the diagonal stresses are not equal everywhere, so we will examine the pressure

tensor diagonal components as

$$P_{\alpha\alpha} = -\sigma_{\alpha\alpha}. \tag{4.17}$$

As jamming is approached, Salsburg and Wood [21] used a free volume approximation to suggest that the pressure in a classical (conservative) hard sphere system approaches

$$P = (\rho T)(1 - (\phi/\phi_c)^{1/D})^{-1}. \tag{4.18}$$

They also gave an asymptotic approximation (as $\phi \to \phi_c$) of Eq. (4.18) as

$$P = D(\rho T)(1 - \phi/\phi_c)^{-1}. \tag{4.19}$$

In Eqs. (4.18) and (4.19) D is the dimension and ϕ is a volume packing fraction

$$\phi = \frac{4}{3}\pi a^3 \frac{\rho}{m}, \tag{4.20}$$

where m is a mean grain mass, and ϕ_c is a random close-packed density. Normally these expressions involve Boltzmann's constant and the absolute temperature, which is not relevent for dissipative granular materials so we follow standard convention and replace $k_B T$ with the granular temperature in Eq. (4.8), something that would be entirely equivalent in a conservative hard sphere system. Also, the true form of Eq. (4.19) has an additional constant of order 1, but literature usually quotes this equation suppressing the constant.

As can be seen in Fig. 4.4 both Eqs. (4.18) and (4.19) do well as the close-packed density is approached in the glassy region, but they give higher pressures than what we observed in our simulation at lower densities in the fluid regions. As expected, the asymptotic approximation Eq. (4.19) is worse in the fluid region than the true free-volume expression Equation (4.18), although both disagree with
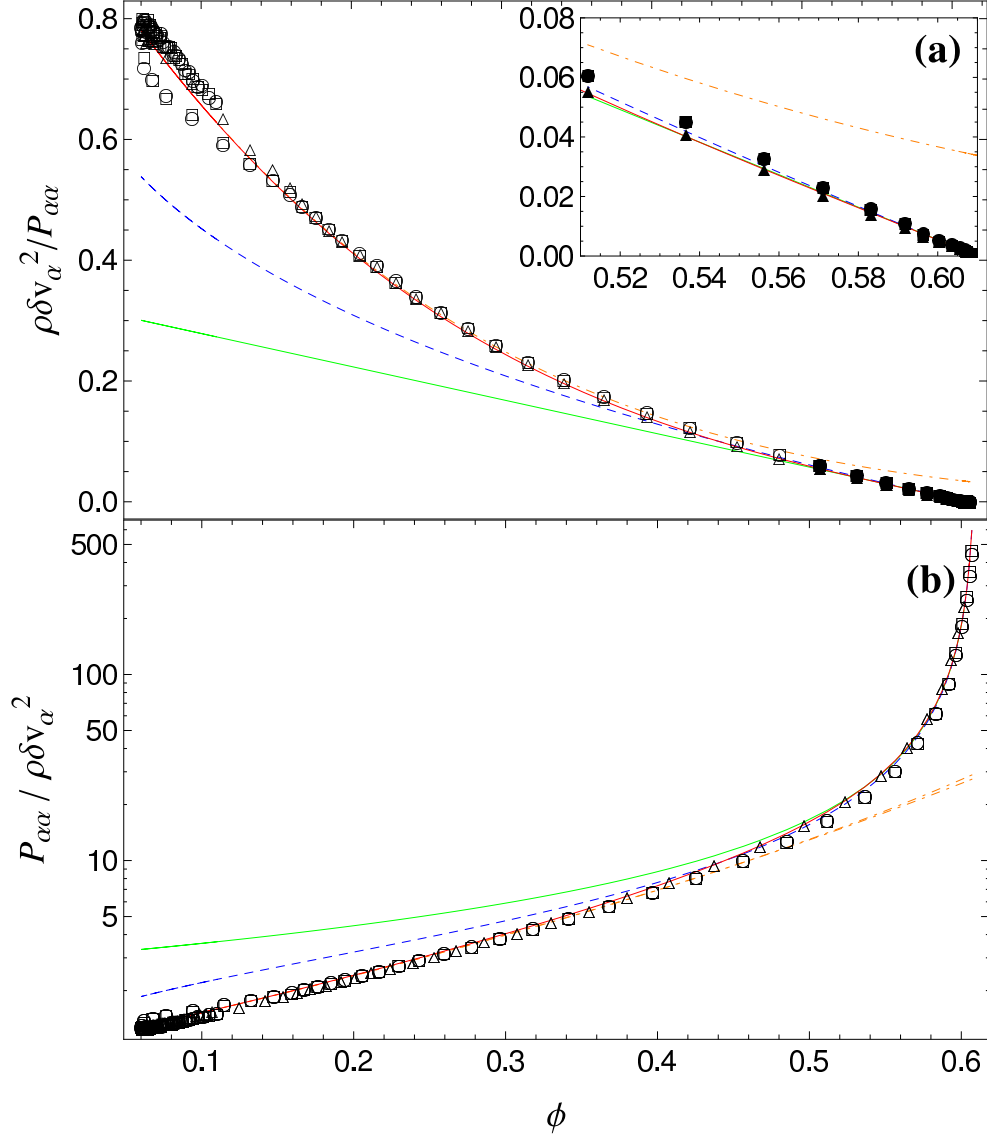
Figure 4.4: (a) Plot of $\rho \delta v_x^2 / P_{xx}$ (squares), $\rho \delta v_y^2 / P_{yy}$ (triangles), and $\rho \delta v_z^2 / P_{zz}$ (circles) versus ϕ. Also plotted are the result from Eq. (4.19) (solid green (bottom) line), Eq. (4.18) (blue dotted (middle) line), and Eq. (4.23) (orange dot-dashed (top) curve). ϕ_c is the observed close-packed density in the glassy region and $\delta v_\alpha^2 = \langle (v_\alpha - \langle v_\alpha \rangle)^2 \rangle$. (b) Reciprocal of data in (a). In both plots closed symbols indicate the glassy region and open symbols the fluid regions. The data is for a $32 \times 32 \times 400$ simulation with an asymptotic coefficient of restitution $\mu_0 = 0.97$ and a probability of reflection at the bottom of the chute $p = 0.9$. The solid red curve through the data is described in the text.

our simulation data in the fluid region. Similar effects are found in simulations of elastic hard sphere packings [22].

At low densities, a more appropriate approach to studying the equation of state of a hard sphere fluid is to use a virial expansion:

$$\frac{P}{\rho T} = 1 + B_2 \phi + B_3 \phi^2 + ..., \tag{4.21}$$

where again ϕ is the volume packing fraction proportional to density and B_i are the virial coefficients. For hard spheres, the Carnahan-Starling [23] equation of state for a hard sphere fluid uses a rescaled virial series solution of the Percus-Yevick equation [24] for hard spheres which is an approximate integral equation for determining the radial distribution function of a fluid. It uses the rescaled virial series

$$\frac{P}{\rho T} = \frac{1 + c_2 \phi + c_3 \phi^2 + ...}{(1 - \phi)^3}, \tag{4.22}$$

where c_i are related to the virial coefficients B_i. The Carnahan-Starling [23] equation of state is written as

$$\frac{P}{\rho T} = \frac{(1 + \phi + \phi^2 - \phi^3)}{(1 - \phi)^3}. \tag{4.23}$$

Both the Carnahan-Starling equation, Eq. (4.23), as well as the virial expansion to 12 coefficients, as derived in [25, 26], are shown in Figure 4.4 (dash-dotted lines, indistinguishable from each other except at high densities in Figure 4.4(b)) and agree well with our data in the lower density fluid region. In the literature, there are several other equations of state that are proposed as solutions to the Percus-Yevick equation which are slightly more accurate than the Carnahan-Starling equation. Examples of these include the Kolafa equation [27] and the Malijevsky and Veverka equation of state [28]. The Malijevsky and Veverka equation, for instance, uses a combination of the analytical solution of the Percus-Yevick equation and a Pade approximation of the rescaled virial series using the

first seven virial coefficients to improve the convergence of the virial expansion. When we plotted the Kolafa and Malijevsky and Veverka equations of state we found that these solutions were very close to the Carnahan-Starling equation of state and gave no significant improvement in agreement with our data.

The close agreement between the virial/Carnahan-Starling result and our data is surprising. These theoretical results are based on the assumption that the grains are in a thermal equilibrium which would be characterized by a Gaussian distribution of velocities. In contrast to a conservative hard sphere fluid, a dissipative granular fluid does not form a Gaussian velocity distribution. Experiments [29, 30] and theory [31, 32, 33] have shown, and we previously demonstrated using our simulation [8] (Chapter 3), that in a granular fluid, the distribution is not Gaussian. At low v_x, the v_x distribution is Gaussian but it has stretched exponential tails. These tails gradually fill the whole distribution such that the entire distribution can be well fit with a 1.5 power law instead of the power-law exponent of 2 that would be expected for a Gaussian velocity distribution [8] (Chapter 3). The lack of normal thermal equilibration is also particularly evident in the free-fall to fluid transition area (the low density region in Fig. 4.4(b)). Here the P_{yy} data match the Carnahan-Starling equation and the virial expansion, but P_{xx} and P_{zz} do not. This indicates that in this transition region, the fluid is not fully equilibrated in the x-x and z-z directions. Thus we shouldn't expect that Eq. (4.23) and the coincident virial expansion can be directly applied to a granular fluid. Surprisingly, however, the Carnahan-Starling and the virial expansion work extremely well in the fluid region, matching our simulation data. A reason may be that even though in the velocity distribution the 1.5 power law exists in the tails, the distribution still remains Gaussian in the center. This implies that the pressure in the fluid and free-fall region is not too sensitive to the tail distribution.

It is also remarkable that there is no real signature of the different phases in the

pressure. The ratio of $P/(\rho T)$ diverges as close packing is approached but is still finite throughout the glassy region. As we shall see below, these phases are only distinct when we consider dynamic properties such as transport coefficients. This fits with the usual description of the glass transition being a dynamical transition. What is perhaps more interesting is that the free-fall to fluid transition must also be a dynamic transition if these phases are truly distinct. We will examine this in more detail in later sections.

An expression that interpolates between the virial and the free-volume expression for the pressure can be found by taking the virial expansion up to and including $B_5 \phi^4$ and adding to it Eq. (4.18) and subtracting the Taylor series expansion of Eq. (4.18) taken about $\phi = 0$ up to and including the ϕ^4 term:

$$
\begin{aligned}
\frac{P}{\rho T} &= (1 + B_2 \phi + B_3 \phi^2 + B_4 \phi^3 + B_5 \phi^4) \\
&+ \left[1 - \left(\frac{\phi}{\phi_c} \right)^{1/3} \right]^{-1} - \sum_{n=0}^{n=12} \left(\frac{\phi}{\phi_c} \right)^{n/3}.
\end{aligned}
\tag{4.24}
$$

This is shown in Fig. 4.4 as the solid red line that goes through the simulation data.

4.2.4   Collision frequency

Many of the constitutive relations that follow, such as for the dissipation and energy flux involve a collision frequency (per unit volume). Thus, it seems appropriate to first establish closed relations for the collision frequency, f_c that are valid in the different regions. A closed relation for the collision frequency includes the pressure, P. In the previous section, we combined a virial expansion with a free-volume theory expression to establish a relation for the pressure, P, that works equally well in the fluid and glass regions. We can also derive the pressure,

P. We know $P_{\alpha\beta} = -\sigma_{\alpha\beta}$, and we have the stresses, $\sigma_{\alpha\alpha}$, plotted in Fig. 4.1(e). We have for the virial pressure

$$V = -\frac{1}{3} Tr \left(\sigma_{\alpha\beta} - \langle \rho \left(v_\alpha - \langle v_\alpha \rangle \right) \left(v_\beta - \langle v_\beta \rangle \right) \rangle \right), \quad (4.25a)$$

$$\approx P - \rho T, \quad (4.25b)$$

where the pressure P is a function of the density ρ and granular temperature T as detailed in the previous section. The kinetic term in Eq. (4.25a), $\langle \rho \left(v_\alpha - \langle v_\alpha \rangle \right) \left(v_\beta - \langle v_\beta \rangle \right) \rangle$, is negligible in the glass but is significant in the fluid and free-fall regions. Using Eq. (4.5) we also have the relation

$$V = \frac{1}{2} f_c \langle (1 + \mu)(\dot{\mathbf{r}}_{\mathbf{1}} - \dot{\mathbf{r}}_{\mathbf{2}}) \cdot \mathbf{q} \rangle, \quad (4.26)$$

where

$$(\dot{\mathbf{r}}_{\mathbf{1}} - \dot{\mathbf{r}}_{\mathbf{2}}) \cdot \mathbf{q} = \mathbf{v_n} \quad (4.27)$$

is simply the normal impact velocity between the colliding particles. Note that we have already studied constitutive relations for the pressure in section 4.2.3.

Using the relations for the pressure determined in section 4.2.3, we can solve for the collision frequency as follows. We can use the fact that

$$\langle (1 + \mu)(\dot{\mathbf{r}}_{\mathbf{1}} - \dot{\mathbf{r}}_{\mathbf{2}}) \cdot \mathbf{q} \rangle = 2 \langle 1 + \mu \rangle \langle v_n \rangle, \quad (4.28)$$

where the factor of 2 is because we have counted the momentum transferred from particle 1 to 2 and from particle 2 to 1 in the average over collisions.
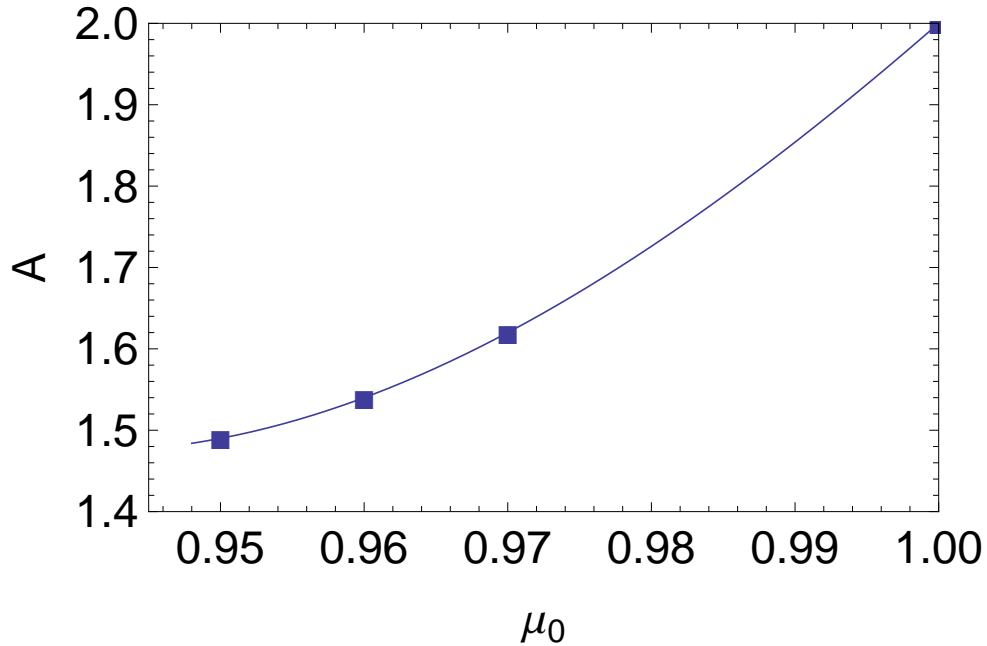
Figure 4.5: Plot of the empirically determined parameter A in Eq. (4.31) for the glassy region of the chute from simulations with different asymptotic coefficients of restitution μ_0. The line is just a guide for the eye.

By combining Eqs. (4.25a), (4.26) and (4.27) we have

$$f_c = \frac{3V}{\frac{1}{2}\langle [1 + \mu(v_n)]\, v_n \rangle} \tag{4.29a}$$

$$\approx \frac{3V}{\langle 1 + \mu(v_n)\rangle \langle v_n \rangle}, \tag{4.29b}$$

where the $\frac{1}{2}$ in Eq. (4.29a) has been cancelled by the 2 from Eq. (4.28).

Now, $\mu = \mu(v_n)$ is the velocity-dependent coefficient of restitution given by Eq. (4.2). Here v_n is the component of relative velocity along the line joining the grain centers.

During a collision the sign of v_n is fixed and v_n is always positive, as can be readily seen from Eq. (4.27). In Ref. [8], we showed that v_n^2 traces the velocity

fluctuations δv_α^2. Thus we expect $\langle v_n \rangle$ to be related to $\langle |\delta v_\alpha| \rangle$,

$$\langle |\delta v_\alpha| \rangle = \sqrt{\frac{2}{\pi}} \langle \delta v_\alpha^2 \rangle^{1/2}, \tag{4.30}$$

if δv_α is distributed in a Gaussian. This is nearly true in the liquid and free-fall regions. However, as will be explained below, δv_α is not strictly distributed in a Gaussian distribution in the glassy region. If the particles are moving statistically independently

$$\langle v_n \rangle = \sqrt{\frac{2}{\pi}} A T^{1/2}, \tag{4.31}$$

where $A = 2$ in the liquid and free-fall regions. In the glassy region $P(\delta v)$ is *not* Gaussian [8] (Chapter 3) and the particles are not moving or colliding independently [8, 9] (Chapters 2 and 3). So $\langle v_n \rangle_{\text{collisions}} \neq \langle \delta v \rangle_{\text{particles}}$. Thus in the glass, $A < 2$ and a value for A has to be determined empirically. For an asymptotic coefficient of restitution of $\mu_0 = 0.97$, we found $A = 1.62$ in the glass. Figure 4.5 shows a plot of A in the glassy region for three different coefficients of restitution. As the simulation becomes more elastic, that is as $\mu_0 \to 1$, $A \to 2$.

We also calculated A in the glassy region for simulations with different sieve probabilities, hence for different flow rates with the same asymptotic coefficient of restitution, and found that A did not vary with the flow rate in the glassy region.

Upon combining, Eqs. (4.2), (4.29), and (4.30), we finally arrive at closed expression for the collision frequency f_c. We can use the fact that in the glass the normal velocity, v_n, is less than the cutoff velocity $v_0 = \sqrt{2ga}$ [16]. Here, g is the acceleration due to gravity and a is the particle radius. Thus our expression for
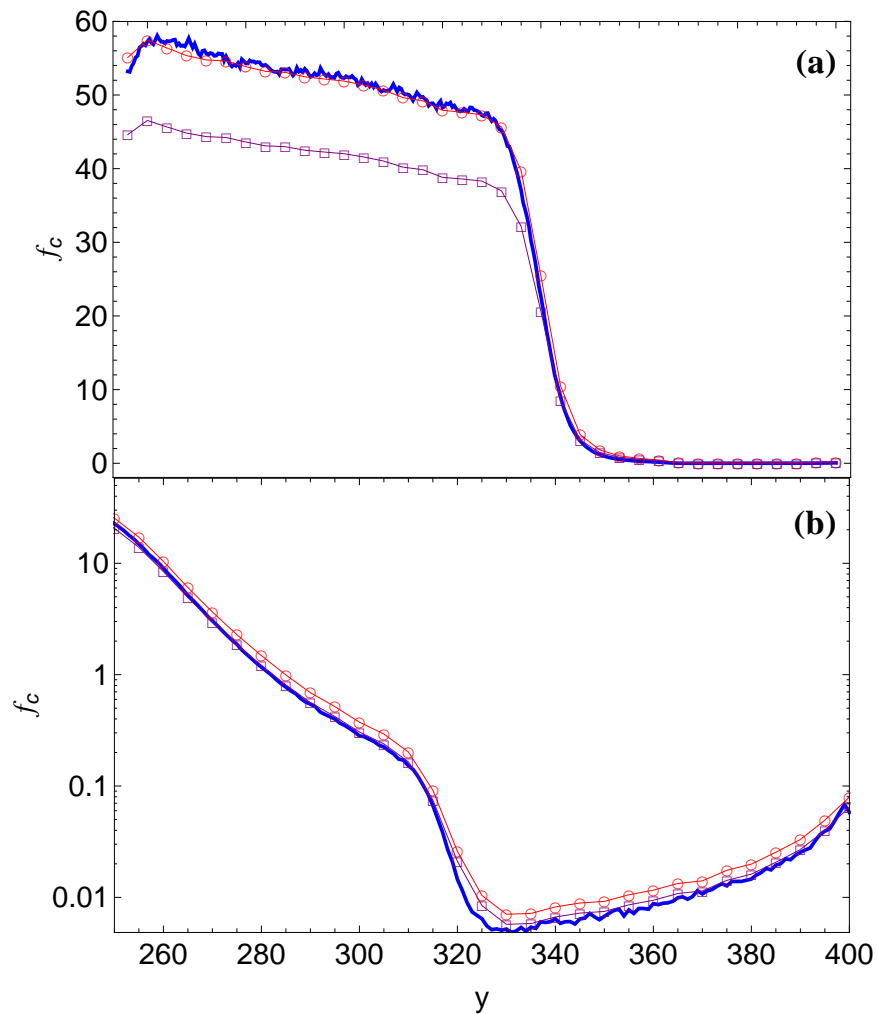
Figure 4.6: Plot of the collision frequency per unit volume as calculated using Eq. (4.32) using $A = 1.62$ (red line with $\circ$'s), as calculated using Eq. (4.32) using $A = 2$ (purple line with $\square$'s), and the simulation values for the collision frequency (blue solid line) versus the height y of the chute in (a) the entire chute and (b) in the fluid region (semi-logarithmic). Measurements are taken in the center of the chute using a simulation with an asymptotic coefficient of restitution $\mu_0 = 0.97$. Data is averaged over depth $(32a)$ in z and over 800 time units.

the collision frequency becomes

$$f_c = \frac{3V}{\left[1 + 1 - (1 - \mu_0)\left(\frac{\sqrt{\frac{2}{\pi}}AT^{1/2}}{v_0}\right)^{0.7}\right]\sqrt{\frac{2}{\pi}}AT^{1/2}}, \qquad (4.32)$$

with A as defined for the different regions in the paragraph above. Fig. 4.6 shows that the collision frequency as calculated using Eq. (4.32), and the collision frequencies obtained from the simulation agree nicely.

4.2.5 Conservation equations in free-fall region

Now that we have established a closed relation for the collision frequency in the fluid, glass and free-fall regions, we can examine closed relations for the properties in the different regions that depend on the collision frequency. In this section, we will examine properties in the free-fall region which we can solve for analytically. In the free-fall region, the stresses are very small, and their gradients even smaller. As can be seen from the flat pressure profile in the free-fall region in the inset in Fig. 4.1(e), there is a small (mostly kinetic) stress contribution. This allows us to greatly simplify the above equations and solve for the density, velocity and energy in the free-fall region. As described in Ref.[8] (Chapter 3), the fluid region begins as a boundary layer in the free-fall region which gradually grows to dominate the flow. What we describe in this section applies only to the plug-like flow in the central (away from the walls) portion of the channel. In this plug-like flow region, velocity gradients in the x-direction are negligible (e.g. see Fig. 3(b) in Ref. [8]) (Fig. 3.3(b) in Chapter 3), as are shear stresses σ_{xy}. Due to the periodic boundary conditions in the z-direction physical properties are translationally invariant, on average, along z. Our system is in a steady state so we can also assume that the partial derivative with respect to time in Eqs. (4.3), (4.4), and (4.6) are negligible.

With these assumptions in the free-fall region, the continuity equation Eq. (4.3) translates to

$$\partial_y \left(\rho v_y \right) = 0. \tag{4.33}$$

and the y component of the Navier-Stokes Eq. (4.4) translates to

$$\partial_y \left(\rho v_y^2 \right) = \partial_y \sigma_{yy} + \rho g. \tag{4.34}$$

There is a very small kinetic contribution to the stress as can be seen in the inset in Fig. 4.1(e):

$$\sigma_{yy} = -\rho \delta v_y^2. \tag{4.35}$$

However this kinetic stress contribution in the free-fall region is nearly constant (except close to the inlet) as can be seen by the horizontal profile in the inset in Fig. 4.1(e), and thus

$$\partial_y \sigma_{yy} = -\partial_y \rho \delta v_y^2 \approx 0. \tag{4.36}$$

We can then solve for the density and velocity in the free-fall region using Eqs. (4.33) and (4.34) and one data point in the bulk interior of the free-fall region at a height y_0, at mid-width (mid $x-$direction) and mid-depth (mid $z-$direction) in the chute. The reason we use an interior point as opposed to a boundary value say, at the top of the chute is because the assumption that σ_{yy} is constant is most accurate once the grains have moved a finite distance into the chute. This assumption is not strictly a required to solve the equations, but it is required if we wish to solve without consideration of the energy equation.

Thus solving Eqs. (4.33) and (4.34), gives us the solution

$$\rho = c/v_y, \tag{4.37}$$

$$v_y \approx -\sqrt{2gy + k_1}, \tag{4.38}$$

where the constants are

$$k_1 = v_{y_0}^2 - 2gy_0, \tag{4.39}$$

$$c = \rho_{y_0}v_{y_0}, \tag{4.40}$$

where ρ_{y_0} and v_{y_0} are measured at any single point in the interior of the free-fall region as described in the previous paragraph. Eqs. (4.37) and (4.38) are plotted as dashed lines in the free-fall region in Fig. 4.1(b) and (c). The agreement between the analytical results and the simulation in the free-fall region is remarkably good. Not surprisingly, there is some deviation at the very top of the chute where the approximation that $\sigma_{yy} \approx constant$ breaks down. As noted above, in the free fall region the stress is almost entirely from the kinetic terms so that $\sigma_{yy} = -\rho\delta v_y^2$ so to improve our analytic solution we must examine the energy equation (to obtain a better solution for δv_y^2).

It is clear however, that to solve these equations analytically (or numerically without input from the simulation) that constitutive relations giving I and F_c are needed. These will be presented in section 4.2.7.

4.2.6   Shear-Stress Constitutive Relations: Models of Viscosity

In section 4.2.2, we demonstrated the importance of the shear stress gradient in supporting the weight. This was significant in the glassy region. In this section, we will examine constitutive relations in the glassy region that involve the shear stress. Closely related to the shear stress is the shear rate (velocity gradient), and the viscosity, so we will examine these properties as well.

In references [8] and [9] (Chapters 2 and 3), it was demonstrated that the velocity profile of particles in the fluid was parabolic (Poiseuille flow), but as one approached the glassy region a plug type profile emerged. The development of

this plug profile in the y-velocity was clearly correlated with the center region so-lidifying into a glass. As the particles travel down the chute, they are slowed by the drag force at the walls supporting the weight of this glassy region via a shear stress. This gives a plug-like profile. We cannot overemphasize the important role that the shear stress has on the y-velocity profiles for particles traveling from the fluid to a glassy region. The stresses were shown to be crucial in providing the weight balance that we discussed in section 4.2.2. In this section, we will discuss constitutive relations for the shear stress in the fluid and glassy regions of our granular system.

Most works based on kinetic theory assume a fluid-like constitutive relation for the shear stress in the system

$$\sigma_{xy} = \eta \partial_x v_y, \tag{4.41}$$

where σ_{xy} is the shear stress, η is the effective viscosity and $\partial_x v_y$ is the shear rate. The difficulty with such descriptions is that the viscosity η is strongly dependent on quantities such as the granular temperature which varies considerably in space in many granular systems.

This complexity can be seen in Fig. 4.7(a) which plots the shear stress, σ_{xy}, vs. the shear rate $\partial_x v_y$ in the granular fluid region for different heights. Here, it was important to use a slow ($p = 90\%$) system with a high enough asymptotic coefficient of restitution $\mu_0 = 0.95$ in order to achieve a true fluid region. The temperature in this region is fairly uniform in width x but changes dramatically in height y (see Figs. 5 and 6 in reference [8]) (Figs. 3.5 and 3.6 Chapter 3). We plotted the shear stress σ_{xy} versus the shear rate $\partial_x v_y$ for different heights, hence at different temperatures for these different heights, as shown in Fig. 4.7(a). Fig. 4.7(a) does display the linear relation of Eq. (4.41). To calculate the viscosity η, we then measured the slopes of σ_{xy} versus $\partial_x v_y$ at these different heights, and

plotted these viscosity values versus the granular temperature T at these heights. We obtained a power-law relationship between the viscosity and the granular temperature along heights in the fluid region as shown in Fig. 4.7(b).

$$\eta \sim T^{-4/3}. \tag{4.42}$$

Equation (4.42) for the fluid region seems surprising. If one recalls, in section 4.2.3, particularly by looking at Fig. 4.4, we were able to successfully match the pressure in the fluid region from our simulation to the pressure equation of state obtained from a virial expansion. Thus it appears reasonable that one should expect our fluid to behave as a hard sphere gas whose viscosity as given from any standard textbook [34] would be:

$$\eta = \frac{5}{64} \frac{1}{a^2} \sqrt{\frac{m k_B T}{\pi}}, \tag{4.43}$$

where a is the particle radius, m its mass, k_B is Boltzmann's constant and T is the absolute temperature. One can see from Eq. (4.43), for a hard sphere gas, the viscosity $\eta \sim T^{1/2}$. Thus one would expect the viscosity to increase with temperature, but from Eq. (4.42) and the corresponding Fig. 4.7(b), the viscosity actually decreases with increasing temperature. This is not how a gas behaves. This behavior is often associated with a liquid whose viscosity grows larger as the temperature decreases as one approaches the solid state. The viscosity in a liquid typically has an exponential relation that is found in standard textbooks [34]

$$\eta = \eta_0 e^{E_{a,\eta}/RT}, \tag{4.44}$$

which as, in our simulation data, does decrease with increasing temperature. In Eq. (4.44), $E_{a,\eta}$ is the molar activation energy. The fact that we observe a power relation given by Eq. (4.42), and not the exponential relation given by Eq. (4.44), indicates that our granular fluid is not a truly equilibrated fluid. The data in

Fig. 4.7(b), however, when plotted on a semi-logarithmic scale (Fig. 4.7(c)), does seem to be approaching a straight line at higher temperatures (near the top of the fluid region), indicating that the viscosity in our granular fluid is trying to approach exponential behavior.

Numerous experiments have measured velocities and forces in sheared granular matter [35, 36, 37, 38] confining granular matter in a Couette cell between a stationary outer cylinder and a rotating inner cylinder. These experiments are typically shearing a very dense granular state like our glass. In Ref. [39], the authors investigate the relationship between the square root of the granular temperature and shear rate that was observed in the glassy region of granular particles in a Couette cell. Our granular particles are in a shear flow traveling down the chute. The shear zones near the walls in the glassy state of our simulation should be comparable to these experiments.

Following the analysis given in reference [39], using $\sigma_{xy} = \eta \dot{\gamma}$ with $\dot{\gamma} = \partial_x v_y$ being the shear rate and η the viscosity, an expression was derived for the viscosity to scale with the collision frequency,

$$\eta = \eta_0 P / \left(\rho_c d^2 T^{1/2} \right), \qquad (4.45)$$

where d is the particle diameter, η_0 is a dimensionless quantity, and $\rho \sim \rho_c$ the close-packed density has been assumed, so that

$$T^{1/2} = \eta_0 P / \left(\rho_c d^2 \sigma_{xy} \right) \dot{\gamma}. \qquad (4.46)$$

However, this analysis can be taken further. If the pressure given in Eq. (4.45) followed the scaling $P \sim \rho T$, this would give the same scaling $\eta \sim T^{1/2}$ as Eq. (4.43) for a hard sphere gas. This extension was not done in Ref. [39]. The analysis that was provided by the authors in Ref. [39], resulting in Eq. (4.46),

gives $\dot{\gamma} = \partial_x v_y \sim T^{1/2}$. Their analysis did not lead to agreement with their experiment. Experimentally, they observed a power-law with

$$T^{1/2} \sim |\partial_x v_y|^{0.4}. \tag{4.47}$$

A log-log plot of the square root of the granular temperature vs shear rate as measured from our simulation on one side of the chute from $x = 4$ to $x = 16$ in the glassy region is shown in Fig. 4.8(a). We plotted this for a series of systems with different probabilities of sieve reflection, p and different asymptotic coefficients of restitution μ_0. On a log-log plot the top curve in Fig. 4.8(a) vaguely resembles a power-law exponent of 0.4 as in experiment [39] for a fast system ($p = 1\%$, $\mu_0 = 0.9$). As shown by the superimposed bottom curves in Fig. 4.8(a), for the slower systems ($p = 90\%$) with $\mu_0 = 0.9$, 0.95, 0.96 and 0.97, the slope is 0.2, although the power-law regime is not clear for the slower systems as for the faster system. Thus the power law exponent of 0.4 that was reported in the experimental paper [39] is not universal.

Eq. (4.47) indirectly assumes that the viscosity in the sheared glass is a function of the granular temperature. Using the relation $\sigma_{xy} = \eta \partial_x v_y$, we can plot the viscosity, η as $\sigma_{xy}/\partial_x v_y$, versus the granular temperature, T, in the glassy region for both a slow ($p = 90\%$) system which yields a power law of 1.1 and a fast ($p = 1\%$) system which yields a power law of 2.3. This is shown as a log-log plot in Fig. 4.8(b). Clearly, the power-law exponent is not universal here.

We can, however, obtain a universal power law in the sheared glass by plotting the shear stress, σ_{xy}, vs. the shear rate, $\partial_x v_y$, on a log-log plot as shown in Fig. 4.9. We found a universal power law of 0.4 for both slow and fast systems on one side of the chute from $x = 1$ to $x = 15$:

$$\sigma_{xy} = B|\partial_x v_y|^{0.4}, \tag{4.48}$$

with B a constant. This is equivalent to obtaining a universal power law by further plotting (not shown) the viscosity, η on one side of the chute from $x = 4$ to $x = 16$ in the glassy region versus the shear rate, $\dot{\gamma} = \partial_x v_y$ and observing a universal power law of approximately -0.6:

$$\eta = B|\partial_x v_y|^{-0.6}. \tag{4.49}$$

The universal power-law between the shear stress and strain rate given by Eq. (4.48) and shown in Fig. 4.9(a) makes one wonder whether we have a true glassy region. Consider in Fig. 4.9(a) a typical region where a particle of radius a undergoes a strain rate $\partial_x v_y$ of 0.01. In this region, $v_y \sim 1$ so using the relation

$$\partial_x v_y = \frac{\Delta v}{a}, \tag{4.50}$$

we can say that it takes 100 time units for one grain to pass another. However, the time that a particle has in the glassy portion of the chute is

$$\frac{L_y}{v_y} \approx \frac{200}{1} = 200 \text{ time units.} \tag{4.51}$$

Thus, in our glassy region, it takes about the same amount of time for one grain to pass another as it takes for all the particles to traverse the entire chute. If we look at the plot of shear stress at the wall (experimentally measurable shear stress) versus the scaled y velocity at the center minus the y velocity at the wall (experimentally observable strain rate) shown in Fig. 4.9(b), we do observe a finite shear stress when the scaled y velocity at the center minus the y velocity at the wall is zero. This indicates that our glassy region has a yield stress at this zero velocity as would be expected for a glassy region.

It is to be noted that Eq. (4.49) is consistent with Eq. (4.48). It is also important to note that the validity of Eq. (4.41) rests on linear response arguments which

are in turn based on minimum entropy production arguments, or alternatively by applying the Boltzmann equation. Since the Boltzmann equation is not valid in a glass and since our glassy system is not even in equilibrium it should not be suprising that Eq. (4.41) is not valid here.

4.2.7 Energy equation

In section 4.2.1, the energy conservation during steady-state was expressed as

$$\partial_t \left(E \right) + \partial_\alpha \left(F_\alpha \right) = I + \rho g \cdot \mathbf{v}. \tag{4.52}$$

In this section, we will examine the kinetic energy terms on the left hand side of Eq. (4.52) which are related to the granular temperature

$$T = \left(\langle v_x^2 \rangle + \langle v_y - \langle v_y \rangle^2 \rangle + \langle v_z^2 \rangle \right) / 3. \tag{4.53}$$

We assume that the time derivative $\partial_t E$ is zero because we are in steady state, so we will concentrate only on the energy flux components, F_α.

As stated in [20], there is a difference between the "energy flux", $\mathbf{F}$, and the "heat flux", $\mathbf{Q}$. The heat flux, $\mathbf{Q}$ is the uncorrelated part of the energy flux, and can be found using

$$\mathbf{Q} = \mathbf{F_c} + \left(\sigma \cdot \mathbf{v} \right), \tag{4.54}$$

where $\mathbf{F_c}$ is the collision energy flux defined by Eq. (4.10) and σ is the stress tensor defined by Eq. (4.5). In Eq. (4.54), $\sigma \cdot \mathbf{v}$ represents the *coherent* transfer of energy (i.e. non-dissipative) during collisions.

Fourier's law suggests that the heat flux across the chute, Q_x, can be expressed

as proportional to the gradient of the granular temperature, T, by the relation

$$Q_x = -\kappa \partial_x T \tag{4.55}$$

where κ is the thermal conductivity. In our *fluid* region, we plotted the heat flux, Q_x versus the gradient of the granular temperature, $\partial_x T$, across the width (x direction) of the chute. This is shown in Fig. 4.10(a) for a slow system using a probability of reflection at the bottom sieve of $p = 90\%$ and an asymptotic coefficient of restitution of $\mu_0 = 0.95$. Systems with higher coefficients of restitution had the largest fluid regions. It was important here to choose a system with a high asymptotic coefficient of restitution in order to maintain a true fluid region. With lower coefficients of restitution we would simply have a combination of fluid to glass and fluid to free-fall transition regions. As one can see for various heights in the fluid region, the data in Fig. 4.10(a) falls on straight lines. The negative slopes of these straight lines give the thermal conductivity

$$\kappa = -\frac{Q_x}{\partial_x T}. \tag{4.56}$$

In Fig. 4.10, the thermal conductivity, κ was calculated as a linear fit and is shown on a semi-logarithmic plot versus the granular temperature at a range of heights in the fluid region for three slow systems ($p = 90\%$). Fig. 4.10 shows results from systems with different asymptotic coefficients of restitution, with data for $\mu_0 = 0.95$ shown as $\square$'s, 0.96 shown as $\circ$'s and 0.97 shown as $\triangledown$'s. Interestingly, all three systems consistently give an exponential fit in the fluid region of

$$\kappa = Ae^{-T/T_0}, \tag{4.57}$$

where $T_0 \sim 11$, and A is a multiplicative constant.

We may contrast Eq. (4.57) to a thermal conduction expression for a hard sphere

gas given in reference [34]

$$\kappa = \frac{25}{128} \frac{c_v}{a^2} \left(\frac{k_B T}{\pi m} \right)^{1/2}, \qquad (4.58)$$

where c_v is a specific heat and a is the particle radius. It does not seem plausible for our granular gas to have a specific heat as we potentially could argue for an infinite specific heat for our dissipative simulation. From the equation for the thermal conductivity of a hard sphere gas given by Eq. (4.58), one obtains the impression that $\kappa \sim T^{1/2}$ and thus that the thermal conductivity should increase with temperature. The thermal conductivity for our granular fluid does not increase with temperature, but exponentially decays with increasing temperature as given by Eq.(4.57). Thus once again our granular fluid cannot be considered as a hard sphere gas. Our fluid behaves as a liquid: as the temperature decreases, the thermal conductivity increases as one might expect in a material which approaches a solid state as it enters the glassy region.

Now, we will examine the thermal conductivity in the glassy region. The heat flux, Q_x is plotted in the glassy region in Fig. 4.11 across the width (x direction) of the chute. As shown in Fig. 4.11, in the glassy region

$$\kappa = 3\phi f_c = \frac{4}{3}\pi a^3 \rho 3 f_c, \qquad (4.59)$$

(the density times the collision frequency). Eq. (4.59) is the same equation found in 2D in reference [20] where we used a volume fraction rather than density. The factor of 3 in Eq. (4.59) arises only because we have defined temperature differently from the way it was defined in reference [20].

Now we will establish constitutive relations for the dissipation, I, in the free-fall, liquid and glass regions. Since the coefficient of restitution, μ, is highly correlated with the impact velocity, v_n, we cannot simply factor the terms in

Eq.(4.11), $-\frac{1}{4}\langle(1 - \mu^2)v_n^2\rangle$ as $-\frac{1}{4}\langle 1 - \mu^2\rangle\langle v_n^2\rangle$ (we could factor out $(1 + \mu)$ in previous expressions (e.g. for the collision frequency) because the *relative* change in $(1 + \mu)$ for different v_n is small whereas the relative change in $(1 - \mu^2)$ for different v_n is large). We outline below two different constitutive relations for I based on different assumptions.

In the first case, we assume that dissipation is dominated by the high impact collisions. We consider a small proportion, say b, of the dissipation involves v_n being greater than the cutoff velocity v_0 in our velocity-dependent coefficient of restitution Eq. (4.2), and a proportion $1 - b$ of the dissipation involves $v_n < v_0$. Then we have

$$
\begin{aligned}
\langle \delta I \rangle &= \langle -\frac{1}{4}(1 - \mu^2)v_n^2 \rangle & (4.60) \\
&= b\langle -\frac{1}{4}(1 - \mu_0^2)v_n^2 \rangle_{v_n > v_0} \\
&+ (1 - b)\langle -\frac{1}{4}(1 - \mu^2)v_n^2 \rangle_{v_n < v_0}.
\end{aligned}
$$

Now, for $v_n < v_0$

$$
\langle -\frac{1}{4}(1 - \mu^2)v_n^2 \rangle_{v_n < v_0} \approx 0, \tag{4.61}
$$

because $\mu \approx 1$ and v_n is also small for these collisions. Similarly,

$$
\begin{aligned}
\langle v_n^2 \rangle_{\textbf{all}} &= b\langle v_n^2 \rangle_{v_n > v_0} + (1 - b)\langle v_n^2 \rangle_{v_n < v_0}, \\
&\approx b\langle v_n^2 \rangle_{v_n > v_0}. \tag{4.62}
\end{aligned}
$$

Putting it all together gives

$$
\langle \delta I \rangle = \frac{1}{4}(1 - \mu_0^2)\langle v_n^2 \rangle. \tag{4.63}
$$

However, most collisions occur with $v_n < v_0$. If the coefficient of restitution formula for $v_n < v_0$ is used directly and substituted into Eq. (4.2) and the average

of the entire expression is evaluated one gets

$$\langle \delta I \rangle = \frac{1}{2} \frac{(1 - \mu_0)}{v_0^{0.7}} \langle v_n^{2.7} \rangle - \frac{(1 - \mu_0)^2}{4 v_0^{1.4}} \langle v_n^{3.4} \rangle. \tag{4.64}$$

One can relate the averages of $\langle v_n^{2.7} \rangle$ and $\langle v_n^{3.4} \rangle$ to $\langle v_n^2 \rangle$ similar to Eq.(4.30).

Figure 4.12 shows, on a semi-logarithmic plot, the dissipation from the simulation plotted along with the constitutive Eqs. (4.63) and (4.64) (multiplied by the collision frequency). The constitutive equation given by Eq. (4.63) matches the dissipation from the simulation nicely in the liquid and glass regions, strongly supporting the argument that dissipation in these regions is completely dominated by the high impact velocity collisions. For the free-fall region an interpolation is required between Eq. (4.63) and Eq. (4.64) to match the dissipation from the simulation. This is similar to when we interpolated between the free-volume and virial expressions for the pressure in section 4.2.3.

4.2.8 Static Limit

We can also examine the existence of a static limit to the glassy state of our system, and relate it to various other constitutive relations proposed for static granular materials. First we will demonstrate that there is a static limit to our equations for stress.

In the first step we write the 3D stress tensor given in Eq. (6) as [20]:

$$\begin{aligned} \sigma_{\alpha\beta} &\approx -\langle \rho (v_\alpha - \langle v_\alpha \rangle)(v_\beta - \langle v_\beta \rangle) \rangle \\ &\quad - \frac{1}{2} f_c \langle (1 + \mu)(\dot{\mathbf{r}}_\mathbf{1} - \dot{\mathbf{r}}_\mathbf{2}) \cdot \hat{\mathbf{q}} \rangle \langle (\hat{\mathbf{q}} \cdot \hat{\mathbf{e}}_\alpha)(\hat{\mathbf{q}} \cdot \hat{\mathbf{e}}_\beta) \rangle. \end{aligned} \tag{4.65}$$

In Eqs. (4.5) and (4.65) the sum is over collisions in a (long) time interval t, f_c is the collision frequency and μ is a velocity-dependent coefficient of restitution. In going from Eq. (4.5) to Eq. (4.65), we have assumed as in [20] that we could separate the factor $(1 + \mu)(\dot{\mathbf{r}}_1 - \dot{\mathbf{r}}_2) \cdot \hat{\mathbf{q}}$ from the factors in the matrix when computing averages. The validity of this assumption is shown in Figs. 4.13(a) and 4.13(b) which plot the shear stress, σ_{xy}, and $R_{xy} = \frac{1}{2} f_c \langle (1 + \mu)(\dot{\mathbf{r}}_1 - \dot{\mathbf{r}}_2) \cdot \hat{\mathbf{q}} \rangle \langle (\hat{\mathbf{q}} \cdot \hat{\mathbf{x}})(\hat{\mathbf{q}} \cdot \hat{\mathbf{y}}) \rangle$ vs. the width x, at heights in the glassy and fluid regions, respectively. As expected, the plotted lines coincide, and the scale of the gradient of the shear stress in the fluid is appreciably less than in the glass. This can also be done for the normal stresses, σ_{xx}, σ_{yy} and σ_{zz}, in Fig. 4.13(c), which plots the respective stress and the collision directions multiplied by $-\frac{1}{2} f_c \langle (1 + \mu)(\dot{\mathbf{r}}_1 - \dot{\mathbf{r}}_2) \cdot \hat{\mathbf{q}} \rangle$ vs. the height y. Once again, as expected, the plotted lines coincide, except of course in the free-fall/fluid transition where the kinetic terms $\langle \rho v_\alpha v_\beta \rangle$ play a significant role.

As shown in Fig. 4.13(c), in a granular fluid the kinetic term, $\langle \rho v_\alpha v_\beta \rangle$ is important but not in a granular glass where it is negligible. As shown in Fig. 4.14(a), for a granular glass, the factor $f_c \langle (1 + \mu)(\dot{\mathbf{r}}_1 - \dot{\mathbf{r}}_2) \cdot \hat{\mathbf{q}} \rangle$ in front of the matrix changes dramatically in the fluid region but in comparison appears to be nearly constant in the glassy region. Fig. 4.14(b) plots the factor $f_c \langle (1 + \mu)(\dot{\mathbf{r}}_1 - \dot{\mathbf{r}}_2) \cdot \hat{\mathbf{q}} \rangle$ for different sieve reflection probabilities and shows that for slower systems, this factor approaches a a constant. Hence the structure of the stress tensor in the glass comes almost entirely from the collision directions (i.e. the $\langle (\hat{\mathbf{q}} \cdot \hat{\mathbf{e}}_\alpha)(\hat{\mathbf{q}} \cdot \hat{\mathbf{e}}_\beta) \rangle$ terms in Eq. (4.65)). This is very reminiscent of models describing static granular materials based on force chains.

The stress tensor equation, Eq. (4.65), that we have developed, can be compared in the glassy region to a previously proposed static pressure tensor model [6, 7]:

$$p_{\alpha\beta} = -\sigma_{\alpha\beta} = \Lambda_1 n_\alpha n_\beta + \Lambda_2 m_\alpha m_\beta + \Lambda_3 l_\alpha l_\beta, \tag{4.66}$$

"with $\hat{n}$, $\hat{m}$, $\hat{l}$ directors along three nonparallel populations of force chains; the Λ's are compressive pressures acting along these. Body forces cause $\Lambda_{1,2,3}$ to vary in space," [7], however $\hat{n}$, $\hat{m}$, $\hat{l}$ are fixed and are not allowed to change in space. They must be determined from global symmetries and boundary conditions. However, they are mutually orthogonal. We can interpret $\Lambda_{1,2,3}$ to be the eigenvalues of our stress tensor as shown in Fig. 4.15, and $\hat{n}$, $\hat{m}$, $\hat{l}$ to be the eigenvectors of our stress tensor as shown in Fig. 4.15. Since the *collision chains* in our system propagate through our particles at 45 degrees to the x/y axes (i.e. as determined from the eigenvectors $\langle(\hat{\mathbf{q}} \cdot \hat{\mathbf{e}}_\alpha)(\hat{\mathbf{q}} \cdot \hat{\mathbf{e}}_\beta)\rangle$), the normalized directors in the glassy region of our system can be expressed as

$$\hat{n} = \left(\frac{1}{\sqrt{2}}, \frac{1}{\sqrt{2}}, 0\right), \tag{4.67a}$$

$$\hat{m} = \left(-\frac{1}{\sqrt{2}}, \frac{1}{\sqrt{2}}, 0\right), \tag{4.67b}$$

$$\hat{l} = (0, 0, 1). \tag{4.67c}$$

Using Eqs. (4.4) and (4.12) in the static limit, we have component-wise

$$\partial_x \sigma_{yx} + \partial_y \sigma_{yy} = -\rho g_y = \rho g, \tag{4.68a}$$

$$\partial_x \sigma_{xx} + \partial_y \sigma_{xy} = 0, \tag{4.68b}$$

$$\partial_z \sigma_{zz} = 0. \tag{4.68c}$$

Using Eqs. (4.68) with the known stress directions described by Eqs. (4.67), we can solve for the eigenvalues in our glassy region giving

$$\sigma_{xy} = \sigma_{yx} = \Lambda_1 \frac{1}{2} - \Lambda_2 \frac{1}{2}, \tag{4.69a}$$

$$\sigma_{yy} = \Lambda_1 \frac{1}{2} + \Lambda_2 \frac{1}{2}, \tag{4.69b}$$

$$\sigma_{xx} = \Lambda_1 \frac{1}{2} + \Lambda_2 \frac{1}{2}, \tag{4.69c}$$

$$\sigma_{zz} = \Lambda_3 = \text{constant}. \tag{4.69d}$$

Finally, combining Eqs. (4.68) and (4.69) we arrive at

$$(\partial_x \Lambda_1 - \partial_x \Lambda_2)\frac{1}{2} + \frac{1}{2}(\partial_y \Lambda_1 + \partial_y \Lambda_2) = 0, \tag{4.70a}$$

$$(\partial_x \Lambda_1 + \partial_x \Lambda_2)\frac{1}{2} + \frac{1}{2}(\partial_y \Lambda_1 - \partial_y \Lambda_2) = 0. \tag{4.70b}$$

There exist four distinct mathematical solutions to Eqs. (4.70) which are

$$\Lambda_1 = \rho g\,(x - 16) + \text{constant}, \tag{4.71a}$$

$$\Lambda_2 = -\rho g\,(x - 16) + \text{constant},$$

$$\Lambda_3 = \sigma_{zz}|_{x=16} = \text{constant}$$

$$\Lambda_1 = \rho g\,(x - 16) + \text{constant}, \tag{4.71b}$$

$$\Lambda_2 = \rho g y + \text{constant},$$

$$\Lambda_3 = \sigma_{zz}|_{x=16} = \text{constant}$$

$$\Lambda_1 = \rho g y + \text{constant}, \tag{4.71c}$$

$$\Lambda_2 = -\rho g\,(x - 16) + \text{constant},$$

$$\Lambda_3 = \sigma_{zz}|_{x=16} = \text{constant}$$

$$\Lambda_1 = \rho g y + \text{constant}, \tag{4.71d}$$

$$\Lambda_2 = \rho g y + \text{constant},$$

$$\Lambda_3 = \sigma_{zz}|_{x=16} = \text{constant}$$

where we have used symmetry properties at mid-width (at $x = 16$) of the chute. Only the first solution, Eq. (4.71a), makes physical sense for our situation. The second and third solutions, Eqs. (4.71b) and (4.71c) can be ruled out because they

are not symmetrical (i.e. $\sigma_{xx} \neq \sigma_{yy} \neq \sigma_{zz}$ anywhere except at some boundary point). The final solution, Eq. (4.71d), is a hydrostatic case which would result in our stress tensor having no shear stresses. Since we know our system is supported by the shear stress at the walls, we may disregard this last solution. The eigenvalue solutions in the glassy region given by Eq. (4.71a), using one interior point as a boundary condition at mid-width of the chute, are plotted as thick transparent lines in the top left plot of Fig. 4.15. These lines closely match our simulation data.

The vector plots in the top row of Fig. 4.15 show that the directions of the principal stresses in the glassy region of our system (the eigenvectors) are at 45 degrees to the x/y axes in the glassy region, as expected. But in the fluid and free-fall region the principal stress is vertical in line with the shear flow as shown in the second plot of the bottom row of Fig. 4.15. It is also evident from the lower portion of Fig. 4.15 that the intermediate free-fall to fluid transition region between the glass and free-fall region is somewhat chaotic (the minor stresses are not along well defined directions).

4.3   Conclusion

In this paper we investigated constitutive relations in the free-fall, fluid and glassy states observed in our simulations of granular matter. We were able to formulate an equation to explore the static stresses in all three of these granular states and showed that values for the stresses are almost entirely dependent on the collision directions. We further showed that the exponent in the power-law between local velocity fluctuations and shear rate that was determined by experiment in the glassy region is not universal. Similarly we found that the shear viscosity dependence on the granular temperature also does not exhibit a universal power-law.

However we did find a universal power-law relationship with exponent 0.4 between the shear stress and the shear rate in the glassy region. We also showed that there is a yield stress associated with our glassy region.

By studying the energy conservation and heat flow in our systems, we obtained accurate representations of the thermal conductivity for a granular glass and granular fluid. We combined the Navier-Stokes equations of momentum conservation, the continuity equation and the conservation of energy equation together with the constitutive relations that have been presented in this paper. All these equations resulted in determining the collision frequency for which we found a closed expression valid in all three regions. By providing closed expressions for the constitutive relations for the stresses, energy flux and dissipation, it is hoped that we have fulfilled our objective to provide useful constitutive relations that might be suitable for fully solving the stress tensor and the energy flux in granular flows.
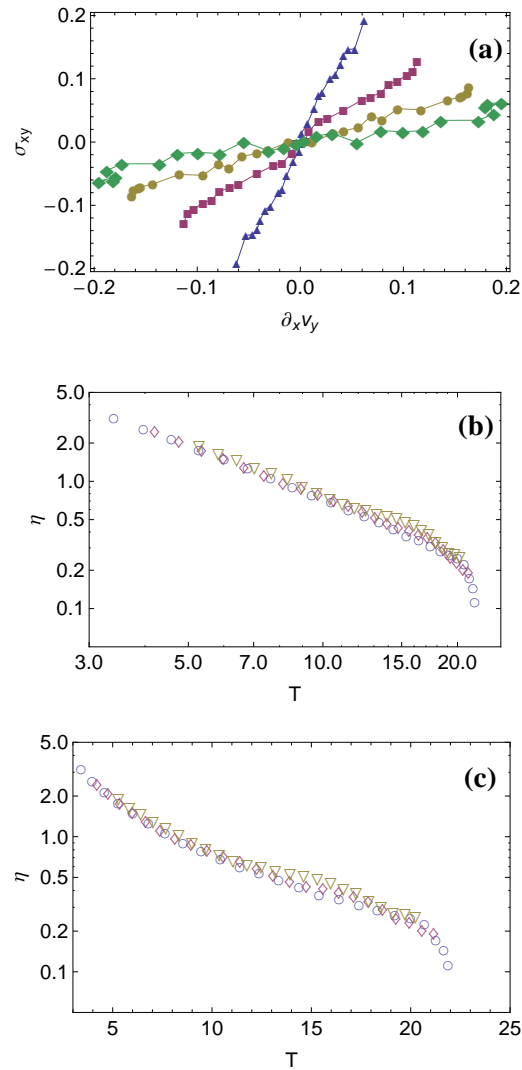
4.4 Acknowledgments

Figure 4.7: (a) Shear stress σ_{xy} versus shear rate $\partial_x v_y$ in the fluid region for a slow flow (probability of reflection at the bottom sieve of p=90%, $\mu_0 = 0.95$). The symbols indicate data at different heights in the fluid region (▲'s at $y = 277$, ■'s at $y = 283$, •'s at $y = 289$ and ♦'s at 295), (b) Log-log plot of viscosity and (c) semilogarithmic plot of viscosity in the fluid region (slope of data in (a)). The symbols indicate different asymptotic coefficients of restitution, μ_0 (with ○'s using $\mu_0 = 0.95$ and $p = 90\%$, ◇'s using $\mu_0 = 0.96$ and $p = 90\%$, and ▽'s using $\mu_0 = 0.97$ and $p = 90\%$). Systems with the higher asymptotic coefficients of restitution of $\mu_0 = 0.95$, 0.96 and 0.97 achieve a true fluid region and have a consistent power-law of $-\frac{4}{3}$.)
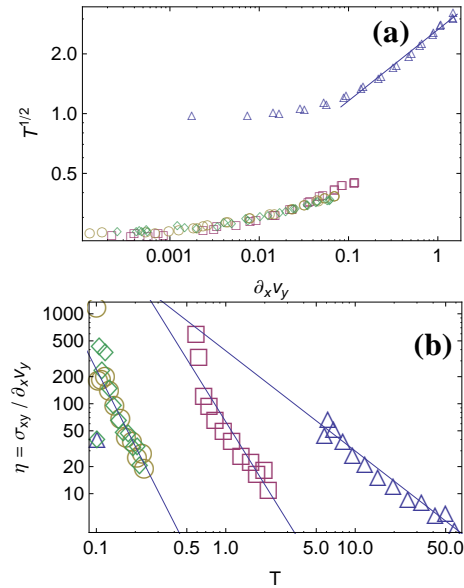
Figure 4.8: (a) Log-Log plot of square root of temperature versus shear rate. A system with a fast flow (probability of reflection at the bottom sieve of $p = 1\%$, $\triangle$ and $\mu_0 = 0.9$) yields the experimental power law exponent of 0.4, while slow systems (probability of reflection at the bottom sieve of $p = 90\%$ with $\mu_0 = 0.9$ $\square$, $\mu_0 = 0.95$ $\circ$, $\mu_0 = 0.96$ $\diamond$, and $\mu_0 = 0.97$ $\triangledown$) have a pseudo-power-law with exponent 0.2. (b) Log-log plot of effective shear viscosity $\eta = \sigma_{xy}/\partial_x v_y$ versus temperature T in the glassy transition region for a fast flow ($\triangle$) and slower flows (symbols same as in (a)). The solid lines have slopes of -1.1 for the fast system, -2.3 for the slow system with $\mu_0 = 0.9$, and -2.8 for the slow systems with $\mu_0 = 0.95$, 0.96 and 0.97.
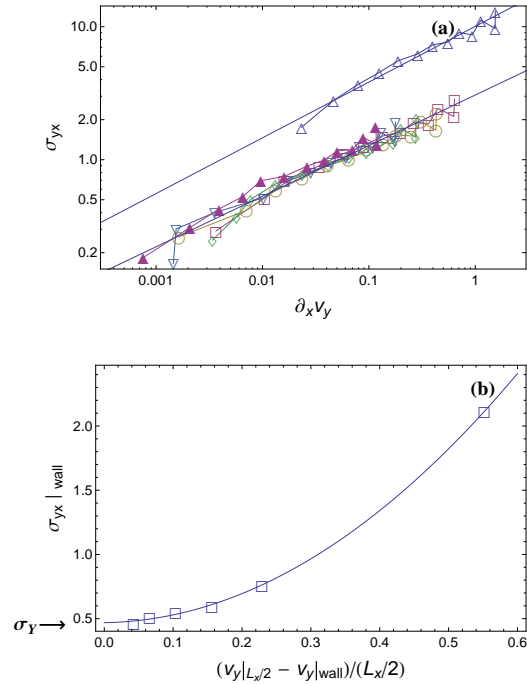
Figure 4.9: (a) Log-log plot of shear stress σ_{yx} versus shear rate $\partial_x v_y$ in the glassy region for various flow rates (probability of reflection at the bottom sieve of p=0.01 as $\triangle$'s, p=0.1 as $\square$'s, p=0.25 as $\circ$'s, p=0.5 as $\triangle$'s, p=0.75 as $\triangledown$'s, and p=0.9 as $\blacktriangle$'s), all with an asymptotic coefficient of restitution of $\mu_0 = 0.9$. The solid straight lines have slopes of 0.41 for the upper line and 0.38 for the lower line. (b) Plot of shear stress σ_{yx} at the wall versus the y velocity at the center at $L_x/2$ minus the y velocity at the wall, scaled by $L_x/2$. The yield stress σ_Y is indicated by the arrow. Data is from a $32 \times 32 \times 250$ column.
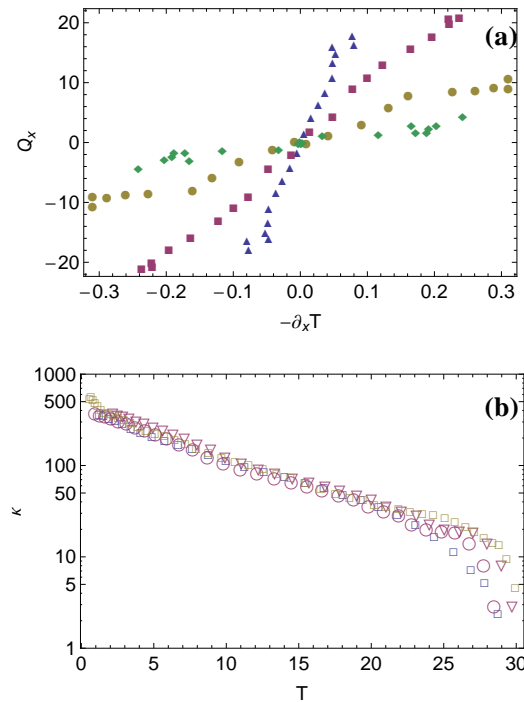
Figure 4.10: (a) Heat flux Q_x versus granular temperature gradient, $-\partial_x T$, in the fluid region (probability of reflection at the bottom sieve of p=90%, $\mu_0 = 0.97$). The symbols indicate data at different heights in the fluid region (▲'s at $y = 274$, ■'s at $y = 284$, •'s at $y = 294$ and ◆'s at $y = 304$), (b) Semi-logarithmic plot of thermal conductivity, $\kappa = -Q_x/\partial_x T$ verus the granular temperature, T, in the fluid region for systems with a probability of reflection at the bottom sieve of p=90%. The symbols indicate different asymptotic coefficients of restitution, μ_0. (with □'s using $\mu_0 = 0.95$, ○'s using $\mu_0 = 0.96$, and ▽'s using $\mu_0 = 0.97$). All three systems give an exponential fit of $\kappa \sim e^{-T/T_0}$ with $T_0 \sim 11$.
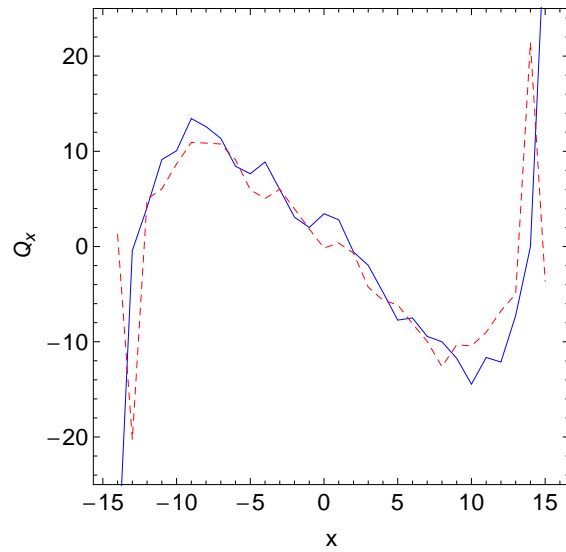
Figure 4.11: Log-log plot of heat flux $Q_x = -\kappa \partial_x 3T$ vs. width x for a 15% polydisperse 3D simulation for a glassy region at $y = 200$ where $\kappa = 4/3\pi a^3 \rho f_c$. The solid line is $Q_x = F_c x + \sigma_{xy} v_y$, and the dashed line is $Q_x = -4/3\pi a^3 \rho f_c \partial_x 3T$.

Figure 4.12: Semi-logarithmic plot of the negative of the dissipation, $-I$, from the simulation as calculated from Eq. (4.11) (blue solid line), as calculated using Eq. (4.63) (red dashed line), and as calculated using Eq. (4.64) (purple dotted line).

117

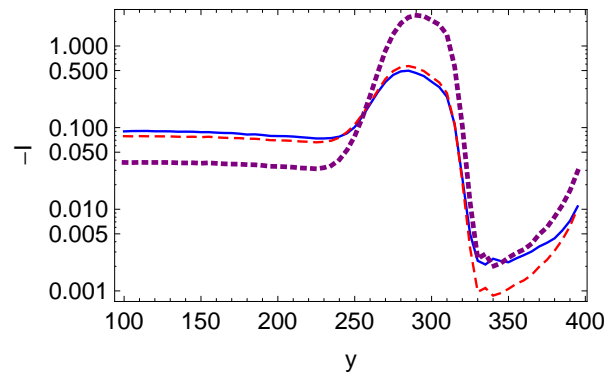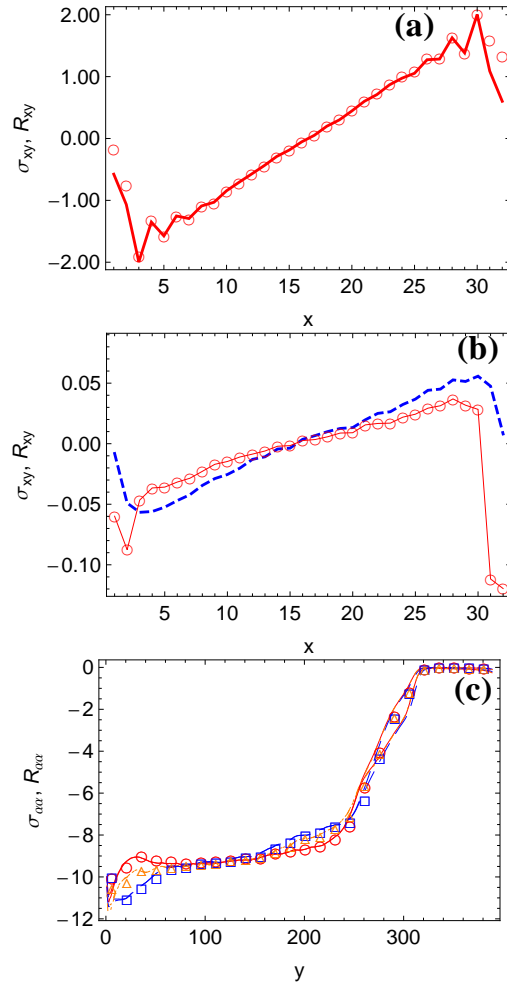Figure 4.13: Shear stress σ_{xy} (solid line) and R_{xy} (circles)(right hand side of Eq. (4.65), the shear stress factorized into the collision directions, $\langle (\hat{\mathbf{q}} \cdot \hat{\mathbf{x}})\,(\hat{\mathbf{q}} \cdot \hat{\mathbf{y}}) \rangle$ and the constant $-\frac{1}{2} f_c \langle (1 + \mu)(\dot{\mathbf{r}}_1 - \dot{\mathbf{r}}_2) \cdot \hat{\mathbf{q}} \rangle)$ versus x in (a) the glassy region at a height, $y = 100$, and (b) the fluid region at a height, $y = 280$, of a 400-height column using an asymptotic coefficient of restitution μ_0 of 0.97. In (b) the dashed line represents data without the kinetic term and the solid line is for data including the kinetic term. (c) Plot of the diagonal stress, $\sigma_{\alpha\alpha}$ with its kinetic term (lower curves) and without its kinetic term (upper curves), and factor $R_{\alpha\alpha}$ versus height y. (σ_{xx} is the solid line, σ_{yy} is the dashed line, and σ_{zz} is the dot-dashed line, R_{xx} is circles, R_{yy} is squares, and R_{zz} is triangles). Data is for a 400-height column using an asymptotic coefficient of restitution μ_0 of 0.97 and a probability of reflection, $p = 0.9$.

Figure 4.14: (a) Plot of $f_c\langle(1+\mu)(\dot{\mathbf{r}}_1 - \dot{\mathbf{r}}_2) \cdot \hat{\mathbf{q}}\rangle$ vs. height y for a 400-height column. The lines from bottom to top represent data with asymptotic coefficients of restitution μ_0 of 0.95, 0.96 and 0.97, all with a sieve reflection probability, $p = 0.9$. Data is averaged over the width (x direction)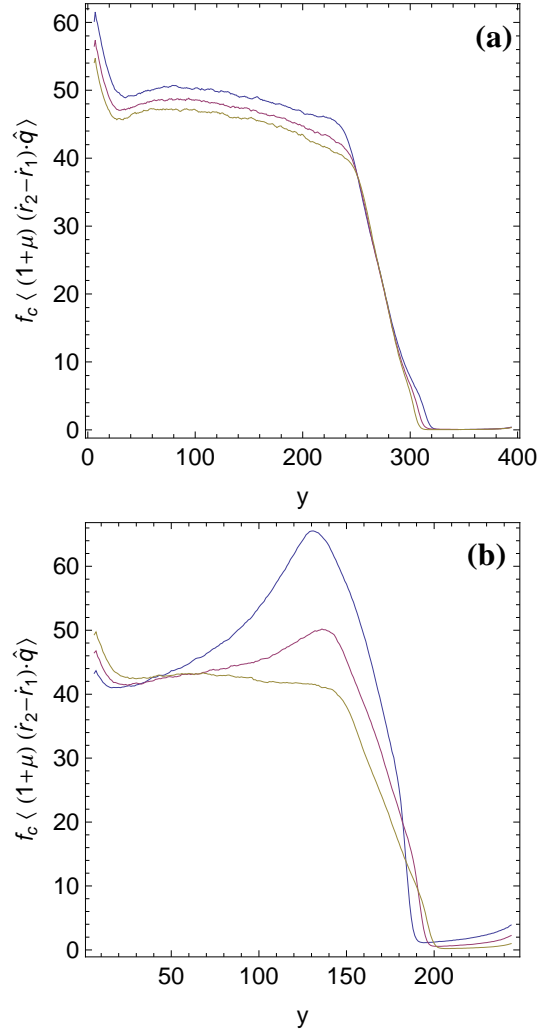. (b) Plot of $f_c\langle(1+\mu)(\dot{\mathbf{r}}_1 - \dot{\mathbf{r}}_2) \cdot \hat{\mathbf{q}}\rangle$ vs. height y for a 250-height column. The lines from top to bottom represent data with sieve reflection probabilities p of 0.25, 0.5 and 0.75, all with an asymptotic coefficient of restitution $\mu_0 = 0.9$.
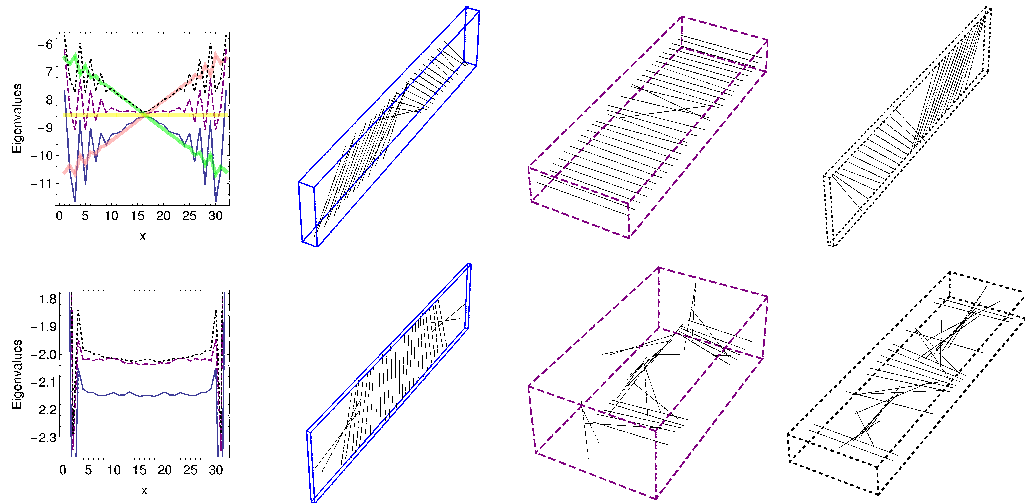
Figure 4.15: Plot of the eigenvalues (compressive stresses) and corresponding directions of the stress tensor along width of column in (Top) the glassy region at $y = 138$, and at (Bottom) top of the fluid region at $y = 305$ for a 400-height column using an asymptotic coefficient of restitution μ_0 of 0.97. In both (Top) and (Bottom), the eigenvalues are associated alongside with the eigenvector directions by the style of the lines. That is, the line style of the eigenvalues (shown as solid, dashed or dotted lines) are matched with the line style of the box (shown as a solid, dashed or dotted lined box) surrounding the particular eigenvector directions. The analytical solution for the eigenvalues given by Eq. (4.71a) are plotted as thick lines with Λ_1 drawn in pink, Λ_2 in green and Λ_3 in yellow.

REFERENCES

[1] M. Otto, J.-P. Bouchaud, P. Claudin and J.E.S. Socolar, Phys. Rev. E **67**, 031302 (2003).

[2] V.M. Kenkre, M.R. Endicott, S.J. Glass and A.J. Hurd, Journal of the American Ceramic Society **79**, 3045 (1996).

[3] V.M. Kenkre, J.E. Scott, E.A. Pease and A.J. Hurd, Phys. Rev. E **57**, 5841 (1998).

[4] J.-P. Bouchaud, M.E. Cates and P. Claudin, J. Physique I France **5**, 639 (1995); J.-P. Bouchaud, P. Claudin, M.E. Cates and J.P. Wittmer, in *Physics of Dry Granular Media*, H.J. Herrman, J.P. Hovi and S. Luding, Eds., NATO ASI 1997 (cond-Mat/9711135).

[5] J.P. Wittmer, P. Claudin, M.E. Cates and J.-P. Bouchaud, Nature **382**, 336 (1996); J.P. Wittmer, P. Claudin and M.E. Cates, J. Physique I France **7**, 39 (1997).

[6] M.E. Cates, J.P. Wittmer, J.-P. Bouchaud and P. Claudin, Chaos **9**, 511 (1999).

[7] M.E. Cates, J.P. Wittmer, J.-P. Bouchaud and P. Claudin, Physica A **263**, 354 (1999).

[8] J.J. Drozd and C. Denniston, Phys. Rev. E **78**, 041304 (2008).

[9] J.J. Drozd and C. Denniston, Europhys. Lett. **76**, 360 (2006).

[10] V.V.R. Natarajan, M.L. Hunt, and E.D. Taylor, J. Fluid Mech. **304**, 1 (1995).

[11] S. Moka and P.R. Nott, Phys. Rev. Lett. **95**, 068003 (2005).

[12] J. T. Jenkins and S. B. Savage, J. Fluid Mech. **130**, 187 (1983).

[13] S. B. Savage and D. J. Jeffrey, J. Fluid Mech. **110**, 255 (1981).

[14] C. Bizon, M. D. Shattuck, J. B. Swift, W. D. McCormick and H. L. Swinney, Phys. Rev. Lett. **80**, 57 (1997).

[15] S. Luding, E. Clement, J. Rajchenbach, and J. Duran, Europhys. Lett **36**, 247 (1996).

[16] Typical fluctuation velocities are $\delta v = 0.05$ implying $\mu \approx 0.99$.

[17] W. Goldsmith *Impact* (Edward Arnold Ltd., London, 1960), p. 262-263, 267.

[18] C. V. Raman, The Photographic Study of Impact At Minimal Velocities, *Physical Review* **12**: pp. 442-447 (1918).

[19] We use units where the acceleration due to gravity $g = 1$, the mean grain radius $a = 1$, and the mean grain mass $m = 1$. To convert to units where, say, g = 9.8 m/s^2, $a = 1.5$mm $= 1.5 \times 10^{-3}$ m, and $m = 0.11$ grams $= 1.1 \times 10^{-3}$ kg (i.e. a steel ball with mass density of 7850 kg/m^3), multiply our distance by a in meters, time by $(a/g)^{1/2} = [(1.5 \times 10^{-3} \text{ m})/(9.8\text{m/s}^2)]^{1/2} = 0.0124$ s and masses by m in kilograms. A typical simulation run is $10^4 - 10^5$ time units, or $2 - 20$ minutes of real time for a system made up of steel balls 3 mm in diameter. For a typical run with polydisperse grains, this corresponds to 6.5×10^9 collisions.

[20] C. Denniston and H. Li, Phys. Rev. E **59**, 3289 (1999).

[21] Z. W. Salsburg and W. W. Wood, J. Chem. Phys. **37**, 798 (1962).

[22] B. J. Alder and T. E. Wainwright, J. Chem. Phys. **33**, 1439 (1960).

[23] N. F. Carnahan and K. E. Starling, J. Chem. Phys. **51**, 635 (1969).

[24] J. K. Percus and G. J. Yevick, Phys. Rev. **110**, 1 (1958).

[25] J.A. Barker and D. Henderson, Rev. Mod. Phys. **48**, 587 (1976).

[26] L.V. Woodcock,
http://arxiv.org/vc/arxiv/papers/0801/0801.4846v2.pdf

[27] J. Kolafa, unpublished results cited in T. Boublik and I. Nezbeda, Coll. Czech. Chem. Commun. **51**, 2301 (1986).

[28] A. Malijevsky and J. Veverka, Phys. Chem. Chem. Phys. **1**, 4267 (1999).

[29] W. Losert, D. G. W. Cooper, J. Delour, A. Kudrolli and J. P. Gollub, Chaos **9**, 682 (1999).

[30] F. Rouyer and N. Menon, Phys. Rev. Lett. **85**, 3676 (2000).

[31] T. P. C. van Noije and M. H. Ernst, Granular Matter **1**, 57 (1998).

[32] T. P. C. van Noije, M. H. Ernst, R. Brito and J. A. G. Orza, Phys. Rev. Lett. **79**, 411 (1997).

[33] R. Cafiero, S. Luding and H. J. Herrmann, Phys. Rev. Lett. **84**, 6014 (2000).

[34] R. G. Mortimer *Physical Chemistry, Third Edition* (Elsevier, London, 2008), p. 464, 465, 470.

[35] R.A. Bagnold, Proc. R. Soc. London A **225**, 49 (1954); **295**, 219 (1966).

[36] S. Schöllmann, Phys. Rev. E **59**, 889 (1999).

[37] C. Veje *et al.,* in *Physics of Dry Granular Media*, edited by H.J. Herrmann, J.P. Hovi, and S. Luding, NATO ASI Ser. E, Vol. 350 (Kluwer, Dordrecht, 1998).

[38] D.M. Mueth *et al.,* cond-mat/0003433.

[39] W. Losert, L. Bocquet, T. C. Lubensky and J. P. Gollub, Phys. Rev. Lett. **85**, 1428 (2000).

CHAPTER 5

Conclusion

The purpose of this thesis was to unlock a bit of the mystery of and to acquire a better understanding of the nature of granular materials. By studying different physical observable properties such as collision times, velocity distributions and constitutive relations, we were able to show that these properties could be neatly categorized by three states or phases of granular material. We justified and called these regions a free-falling gas, a granular fluid and a glassy region.

A previously proposed phase diagram of granular materials included a glassy and liquid region [1]. We feel the predominance of a granular gas region is also evident and that it should be included in the phase diagram as shown in Fig 5.1.

In the case of collision times, it was important to understand the details of how observable properties were measured in experiments. This played a crucial role in explaining any discrepancies with results measured from our simulation. This was also evident in our study of velocity distributions where we were able to reconcile seemingly conflicting experiments by relating different experimental results with our three different phases of granular matter.

We also demonstrated the importance of the free-fall to fluid transition. Although it was a fluid-like region, we showed that it was not fully equilibrated as
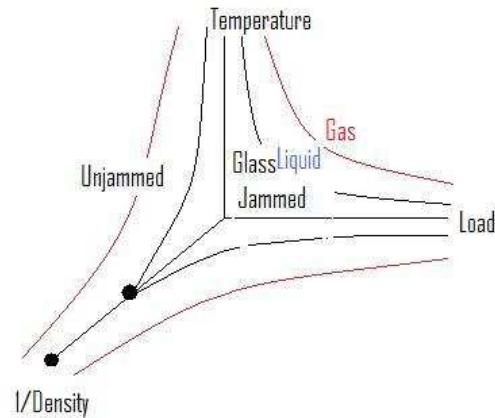
Figure 5.1: Proposed advancement of phase diagram from [1], adding a granular gas region.

a true fluid, and thus it should be considered more as a cross-over rather than a true transition region. We indicated this crossover in our study of the velocity distributions.

Our study of constitutive relations allowed us to probe which experimental and theoretical results were universal by exploring our parameter space. Here, we also compared our findings in the glass and fluid regions to a static stress model used for sand piles and demonstrated that the sand pile is effectively a static limit of our glassy state.

Future work considerations include exploring length scales in the transitional granular fluid region, collision distance distributions and densities of states. We feel that our findings have illustrated the importance of the interplay between theory, experiments and simulations in exploring the true physical nature of granular materials.

REFERENCES

[1] C. S. O'Hern, L. E. Silbert, A. J. Liu and S. R. Nagel, Phys. Rev. E **68**, 011306, (2003).

Curriculum Vita

name: John J. Drozd
place of birth: Brno, Czech Republic
year of birth: 1964
citizenship: Canadian

post-secondary education and degrees:

University of Alberta
Edmonton, Alberta
1982-1985 Mechanical Engineering Co-op

Ryerson University
Toronto, Ontario
1985-1989 Bachelor of Technology, Architectural Science (Project Management)

University of Western Ontario
London, Ontario
1996-2001 Diploma in Honors Standing
Applied Math and Computer Science

University of Western Ontario
London, Ontario
2001-2004 Master of Science
Applied Mathematics

University of Western Ontario
London, Ontario
2004-Present Ph.D. Candidate
Applied Mathematics (Theoretical Physics)

honours and awards:

Ryerson University
Dean's List
Awarded 1986, 1987, 1988

Ryerson University
Highest Grades in Project Management
Awarded 1987

Natural Sciences and Engineering Research Council
Post Graduate Scholarship A
Awarded 2001

SharcNet Fellowship
Awarded 2003

Ontario Graduate Scholarship Award (starting January 2004)
Awarded 2003

Ontario Graduate Scholarship Award (starting January 2005)
Awarded 2004

Shell Sweeney Scholarship Award
Awarded 2007

Faculty of Science Graduate Student Teaching Award
Department of Applied Mathematics
Awarded 2008

related work experience:

Teaching Assistant
The University of Western Ontario
London, Ontario, Canada
2001 - 2008

publications:

S. Saujani, J. Drozd, and R. Mallier, Nonlinear evolution of singular disturbances to a $tanh^3$ mixing layer, *Australian & New Zealand Industrial and Applied Mathematics Journal, Series B, ANZIAM J.* 43 (2002), pp. 409-427.

S. R. Valluri, J. J. Drozd, F. A. Chishtie, R. G. Biggs, M. Davison, Sanjeev V. Dhurandhar, and B. S. Sathyaprakash, A Study of the Gravitational Wave Form From Pulsars, *Classical and Quantum Gravity, Proceedings of the 4th Edoardo Amaldi Conference on Gravitational Waves*, Perth, Western Australia, 8-13 July 2001, Vol. 19 No. 7 (April 2002), pp. 1327-1334.

J. J. Drozd and C. Denniston, Simulations of collision times in gravity driven granular flow, *Europhysics Letters*, 76 (3), (November 2006), pp. 360-366, cond-mat/0609330.

Oleh Baran, John J. Drozd, Robert J. Martinuzzi and Peter H. Poole, Granular circulation in a cylindrical pan: simulations of reversing radial and tangential flows, *Physical Review E*, 76, 021305 (2007), cond-mat/0608072.

John J. Drozd and Colin Denniston, Velocity fluctuations in dense granular flows, *Physical Review E*, 78, 041304 (2008).

John J. Drozd and Colin Denniston, Constitutive relations in dense granular flows, *submitted*.